Univerzita Karlova v Praze

Matematicko-fyzikální fakulta

Habilitační práce

Jety s velkou příčnou hybností na urychlovači Tevatron

Alexander Kupčo

2013

Obsah

1 Úvod

Hlavním tématem předkládané habilitační práce je produkce jetů s velkou příčnou hybností (p_{T}) v proton-antiprotonových srážkách na urychlovači Tevatron ve Fermilab.[1] *Jet*, kolimovaná sprška částic, je otiskem konstituentu protonu, který z něj byl v tvrdé srážce násilně vyražen. Studium produkce jetů nám tak přináší informaci o složení protonu, o jeho konstituentech a interakcemi mezi těmito konstituenty. Jak plyne z Heisenbergovy relace neurčitosti, čím menší je rozměr, který chceme studovat, tím většího přenosu hybnosti je nutné docílit. V laboratořích dosahujeme největších přenosů na hadronových urychlovačích a to právě ve srážkách, kdy vzniknou jety s velkou příčnou hybností. Je to dáno tím, že tyto srážky jsou indukovány silnou interakcí, která je mnohem silnější než elektro-slabá interakce, a tak jsou tyto procesy s produkcí tvrdých jetů nejčastější.

Do spuštění urychlovače LHC v CERN byl největším hadronovým urychlovačem Tevatron. Po modernizaci produkoval srážky protonů s antiprotony při těžišťové energii $\sqrt{s} = 1{,}96\,\mathrm{TeV}$. V datech byly pozorovány jety s příčnou hybností přesahující $600\,\mathrm{GeV}$, což umožnilo studovat strukturu protonu a chování jeho konstituentů na vzdálenostech řádově $1000\times$ menších než je rozměr samotného protonu. Bylo tak možné ověřit předpovědi kvantové chromodynamiky (QCD), teorie popisující silnou interakci, na škále přibližně $10^{-18}\,\mathrm{m}$.

V práci jsou prezentována tři měření týkající se fyziky jetů s velkou příčnou hybností provedená experimentem DØ na urychlovači Tevatron (apendix A-C). Měření azimutálních dekorelací v párové produkci jetů [DØ05] (apendix A) bylo prvním publikovaným měřením z modernizovaného urychlovače Tevatron týkající se jetů s velkým p_{T}. Rozdělení je citlivé na vícenásobné partonové emise a bylo použito jako první test predikce kvantové chromodynamiky v druhém řádu poruchové teorie (NLO - next-to-leading order) pro procesy se třemi partony v koncovém stavu. NLO QCD předpovědi vykázaly dobrý souhlas s měřením v široké kinematické oblasti. Měření bylo také použito pro ladění parametrů a testování modelů partonových spršek v Monte Carlo generátorech, například [CS11], [Fie11], [BBG$^+$11], [Ska10], [BHL$^+$10], [AGH$^+$08].

Měření inkluzivní produkce jetů bylo publikováno ve dvou článcích: [DØ08]

[1] Podélným směrem se rozumí směr srážejících se svazků, příčný směr je pak směr kolmý na osu svazků. V rovině kolmé na svazek je měřen azimutální úhel φ. Osa svazků je dále ztotožněna s osou z kartézských souřadnic a definuje směr, od kterého se měří polární úhel ϑ. V této souřadné soustavě je pak definována pseudorapidita η jako $\eta = -\ln\tanh(\vartheta/2)$ a rapidita y jako $y = \frac{1}{2}\ln\frac{E+p_z}{E-p_z}$, kde E a p_z jsou energie a podélná hybnost objektu. V textu jsou používány přirozené jednotky $\hbar = c = 1$.

(apendix B) a [DØ12] (apendix C). I v tomto případě byl pozorován dobrý souhlas mezi NLO QCD teoretickou předpovědí a daty a to až do největších hodnot příčné hybnosti p_{T}. Byla tak potvrzena platnost kvantové chromodynamiky i v oblasti $p_{\mathrm{T}} \sim 600\,\mathrm{GeV}$ a nebyly nalezeny žádné náznaky nových neznámých jevů, jako například možné nebodovosti a struktury kvarku. Výsledky přinesly novou informaci o složení protonu, především o gluonech, které nesou velkou část hybnosti protonu. Data byla použita skupinami zabývajícími se globálním určováním partonových distribučních funkcí, například v globálních analýzách dat MSTW2008 [MSTW09] a CT10 [LGH$^+$10].

Dnešní experimenty ve fyzice částic jsou díky své enormní experimentální náročnosti prováděny velkými skupinami spolupracujících fyziků a není možné provést samostatně měření a analýzu dat. Nicméně i zde lze identifikovat hlavní autory publikovaných prací. To jsou ti autoři, kteří primárně předložili kolaboraci DØ práci k posouzení.

U všech tří publikací experimentu DØ jsem byl hlavním spoluautorem a vyznamně jsem přispěl k jejich vzniku. V případě dvoujetových azimutálních dekorelací [DØ05] jsem toto měření samostatně prováděl včetně následné analýzy dat. V případě měření inkluzivní produkce jetů [DØ08] a [DØ12] jsem jedním ze tří hlavních autorů. Na měření jsem spolupracoval s doktorandem Mikko Voutilainenem, který prováděl vlastní analýzu dat. Analýza byla založena na kódu, který jsem vyvinul při předchozích měřeních této veličiny. Výsledky těchto prvních měření byly například prezentovány na konferencích EPS2003 [Kup04], Moriond 2005 [Kup05] a ICHEP2006 [Kup07]. K finálnímu měření jsem přímo přispěl hlavně prací na energetické kalibraci jetů, což je největší zdroj výsledné systematické chyby měření. Zabýval jsem se měřením vlastní energetické odezvy kalorimetru na jet, jednak samotným měřením tak i příslušnou systematikou.

Další část předložené habilitační práce se týká modelování hadronizace v Monte Carlo generátorech simulujících srážky částic. K hadronizaci dochází v pozdějších stádiích srážky. Neovlivňuje tedy velmi samotné kinematické vlastnosti jetu, nicméně má vliv na rozložení toku energie v jetu a jeho okolí. Na HERA MC workshopu v DESY v Hamburgu jsem předložil návrh [Kup98] na modifikaci modelu hadrnonizace použitého v Monte Carlo generátoru Herwig [BGG$^+$08]. Pozměněný model napravil chování původního modelu v případě zahrnutí těžších resonancí (tj. hadronů s velmi krátkou dobou života). Model byl dále rozvinut Winterem, Kraussem a Soffem [WKS04] a posléze byl implementován v novějších verzích generátoru Herwig [BGG$^+$08].

Členění předkládané habilitační práce je následující. V kapitole 2 je nejprve stručně shrnut pojem jetu a jsou zavedeny další základní pojmy nutné pro pochopení výsledků měření produkce jetů s velkou příčnou hybností. Ty jsou prezentovány v dalších dvou kapitolách 3 (měření azimutálních dekore-

lací v párové produkci jetů) a 4 (měření inkluzivní produkce jetů). Kapitola 5 je pak věnovaná hadronizačnímu modelu generátoru HERWIG a navržené modifikací tohoto modelu. Nakonec jsou v apendixech A-D přiloženy výše zmíněné publikace týkající se diskutovaných témat.

2 Struktura protonu a jety

Protony, neutrony a ostatní silně interagující částice, souhrnně označovány jako hadrony, nejsou elementární částice na stejné úrovni jako je například elektron. Jak bylo zjištěno v experimentech s pružným rozptylem elektronů na protonech [MH56], mají svůj rozměr, typicky kolem 1 fm, a svoji strukturu.

Následné experimenty s energetičtějšími svazky elektronů na lineárním urychlovači v Stanford Linear Accelerator Center (SLAC) [BCD$^+$69,BFK$^+$69] ukázaly, že pokud dojde k velkému přenosu impulzu (tzv. hluboce nepružný rozptyl), začne se elektron rozptylovat na individuálních konstituentech protonu. Konstituenti se navíc v hluboce nepružných interakcích chovají jako bodové, kvazi-volné částice a příliš mnoho necítí okolní sousedy. Naměřená data vedla Feynmana ještě v témže roce 1969 k formulování *partonového modelu* [Fey73]. V tomto modelu se proton ve vysokoenergetických srážkách jeví jako shluk téměř volných bodových konstituentů - partonů. Každý z nich nese určitou část hybnosti protonu. Proton je pak popsán souborem *partonových distribučních funkcí* $d_i(x)$, které charakterizují pravděpodobnost, že v protonu nalezneme parton i-tého druhu nesoucí poměrnou část celkové hybnosti protonu x.

Data ze SLAC jasně ukazovala, že nabité partony se chovají jako bodové fermiony se spinem 1/2, a že v protonu je také podstatná neutrální komponenta, která nese asi polovinu celkové hybnosti protonu. Nabízela se myšlenka ztotožnit nabité partony s kvarky, které byly zavedeny Zweigem [Zwe64] a Gell-Mannem [GM64] v *kvarkovém modelu*. Tento model vysvětloval vlastnosti a vzájemné vztahy mezi hadrony na základě předpokladu, že se hadrony skládají ze tří druhů kvarků, tzv. vůní ($u,\ d,\ s$), které tvoří fundamentální triplet grupy SU(3). Baryony, například proton či neutron, obsahují 3 kvarky, mesony jsou pak složeny s kvarku a antikvarku. Jednotlivým baryonům jsou přiřazena místa v ireduciblních reprezentacích vzniklých z rozkladu tenzorového součinu $3 \otimes 3 \otimes 3 = 10 \oplus 8 \oplus 8 \oplus 1$. Analogicky, mesonům odpovídají místa v rozkladu $3 \otimes \bar{3} = 8 \oplus 1$, kde $\bar{3}$ je fundamentální antitriplet grupy SU(3) složený z antikvarků.

Problém byl jak vysvětlit, že jsou kvarky v hadronech tak silně vázané, že se coby samostatné částice nepozorují, a na druhou stranu, že se v hluboce nepružném rozptylu chovají zase jako téměř volné. Hledala se teorie,

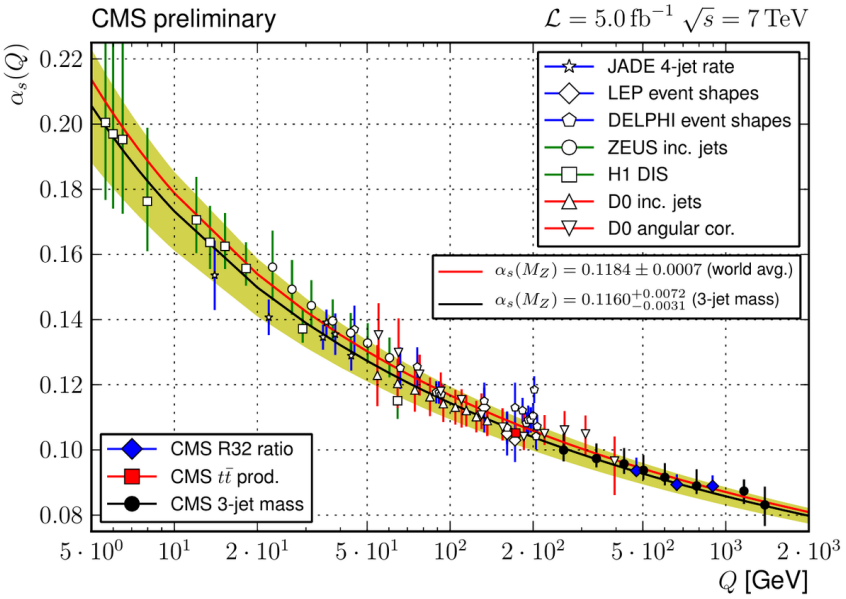

Obrázek 1: Běžení vazbového parametru silné interakce α_S experimentálně naměřené při různých energetických škálách a porovnání s běžením tohoto parametru v QCD, [CMS12].

ve které by byla síla mezi kvarky na velkých vzdálenostech kolem 1 fm velmi velká a naopak na malých vzdálenostech, tedy při velkých přenosech impulzu, klesala k nule. Žádná ze známých kvantově polních teorií, takovéto chování nevykazovala. Například v kvantové elektrodynamice se síla mezi elektrickými náboji chová přesně opačně.

V roce 1973 Gross s Wilczekem [GW73] a nezávisle na nich Politzer [Pol73] zjistili, že tuto asymptotickou volnost v sobě mohou obsahovat teorie Yang-Millsova typu založené na neabelovské grupě kalibrační symetrie. Na této bázi zformulovali teorii silných interakcí, *kvantovou chromodynamiku*, jako kvantově polní teorii s lokální kalibrační symetrií vůči grupě SU(3)[2]. Kvarky nesou náboj silné interakce, tzv. *barvu*. Pro danou vůni kvarku tak existují tři různé barevné stavy odpovídající fundamentální reprezentaci SU(3). Analogicky antikvarky nesou antibarvu odpovídající fundamentálnímu antitripletu SU(3). Příslušné kalibrační vektorové pole, které zprostředkovává silnou interakci mezi kvarky, pak odpovídá elektricky neutrálním a nehmotným gluonům. To jsou ony neutrální partony, které byly pozorovány nepřímo v hluboce nepružném rozptylu elektronu v SLAC.

[2]Jde o jinou SU(3) symetrii než v kvarkovém modelu, která se týkala symetrie mezi různými druhy kvarků.

Na rozdíl od abelovských teorií, jako je QED, kde fotony nemají náboj, gluony barevný náboj nesou, existují v 8 barevných stavech, které odpovídají adjoint representaci SU(3). Gluony tak mohou mezi sebou přímo interagovat a právě díky této vlastnosti vazba mezi dvěma barevnými objekty klesá se zmenšující se vzdáleností, obrázek 1.

Kvantová chromodynamika velmi úspěšně vysvětlila všechny známé fenomeny týkající se silných interakcí. Kvantitativně, a díky neporuchovým výpočtům na mříži i kvalitativně, vysvětlila uvěznění barvy v hadronech. Z Lagrangiánu QCD lze dnes neporuchovými metodami dokonce spočítat i poměry hmotností hadronů [FH12]. Znalost dynamiky silných interakcí umožnila také vysvětlit mírnou závislost strukturních funkcí protonu na kvadrátu přeneseného čtyřimpulzu Q^2 pozorovanou v hlubokém nepružném rozptylu elektronů na protonech.[3] Partonové distribuční funkce, které byly v původním partonovém modelu pouze funkcemi poměrné hybnosti x, závisejí nakonec i na Q^2, čili $d_i(x, Q^2)$. Kvantová chromodynamika tuto závislost plně vysvětluje. Jak bude dále prezentováno v této práci, předpovědi kvantové chromodynamiky jsou v dobrém souladu i při procesech s těmi nejvyššími přenosy impulzu: na Tevatronu byl pozorován souhlas pro jety s $p_{\mathrm{T}} \sim 600\,\mathrm{GeV}$, nejnovější data z LHC pak až do hodnot $p_{\mathrm{T}} \sim 2\,\mathrm{TeV}$ [ATLAS12, CMS11, CMS13].

2.1 Jety

Při srážkách s velkým přenosem hybnosti jsou z protonu prudce vyráženy jednotlivé partony. Kvarky nebo gluony však díky specifičnosti silné interakce přímo nepozorujeme. Podstatnou roli zde hrají dva procesy: tzv. partonové spršky a následná hadronizace.

Vyražený parton, jakožto náboj u kterého došlo k drastické změně pohybového stavu, má silnou tendenci vyzařovat další partony - nejčastěji se tak děje buď ve směru letu původního partonu a nebo se jedná o nízkoenergetický gluon. Je to dáno charakterem teorie, ve které se kromě ultrafialových divergencí vyskytují i tzv. hmotnostní divergence objevující se při kolineárním nebo měkkém vyzáření partonu. Tento mnohonásobný emisní proces se nazývá *partonovou sprškou* a lze jej popsat v rámci poruchové teorie silných interakcí. V nejnižším řádu, tzv. leading-log (LL), se jedná o řetězec náhodných událostí, kdy je pravděpodobnost vyzáření dalšího partonu popsána určitou, spočítatelnou pravděpodobností funkcí. Vzniklé partony pak mohou až do určité meze dané jejich virtualitou vyzařovat další partony. Místo vy-

[3] Kvadrát přeneseného čtyřimpulzu Q^2 je zaveden jako $Q^2 = -(k - k')^2$, kde k a k' jsou čtyřimpulsy dopadajícího a rozptýleného elektronu.

raženého partonu tak rychle vzniká sprška partonů, letících ve směru letu původního partonu. Díky možnosti popisu partonových sprškek v LL aproximaci pomocí Markovova řetězce náhodných událostí, lze modely partonových sprškek implementovat do Monte Carlo generátorů srážek částic jako je PYTHIA nebo HERWIG.

K dalšímu procesu dochází v okamžiku, kdy se vyražený parton, a s ním i oblak partonů vyzářených v následné sprškce, dostane od zbytku protonu na vzdálenost kolem $\Lambda_{QCD} \sim 1\,\mathrm{fm}$. V hodnotě Λ_{QCD} má silná vazbová konstanta pól, analog Landauova pólu v elektrodynamice, a silná síla na těchto vzdálenostech prudce roste. Kvalitativní neporuchové výpočty na mříži ukazují, že se mezi vzdalujícími barevnými náboji pole koncetruje do struny spojující oba náboje. Vyražené partony, stejně jako zbytek protonu, nesou barevný náboj a jakmile se od sebe dostanou na vzdálenost kolem 1 fm, jejich potenciální energie stoupne tak, že je zde dostatek energie k vygenerování nových partonů z vakua, například kvark-antikvarkového páru. Obrazně se struna přetrhne a na jeden její konec se naváže barva a na druhý volný konec anti-barva, tak aby stínily původní barevné náboje vzdalujících se partonů. Proces pokračuje tak dlouho dokud se partony nepřeskupí do bezbarvých celků - hadronů.

Hadronizaci neumíme z prvotních principů kvantové chromodynamiky přesně popsat a nezbývá nám než se uchýlit k fenomenologickým modelům. Ze své podstaty je hadronizace neporuchový jev, kterému však kvalitativně rozumíme. Dokonce lze tyto kvalitativní úvahy i částečně ověřit neporuchovými výpočty na mříži. Pro popis vzniku jetu je důležité, že k procesu hadronizace dochází na mnohem delší časové škále než samotná tvrdá interakce a příliš tak neovlivňuje kinematiku partonové sprškky. I po hadrnonizaci poletí ve směru původního tvrdého partonu kolimovaná sprška částic a sečteme-li jejich energii a hybnost, budou silně korelovány s původní energií a hybností vyraženého partonu. Díky barevné vazbě mezi vyraženým partonem a zbytkem protonu však během hadronizace vzniknou částice i v oblastech mezi jetem a zbytkem protonu. Hadronizace tedy ovlivňuje tok energie v okolí jetu.

Poprvé byly jety pozorovány v e^+e^- interakcích na urychlovači PETRA v laboratoři DESY v Hamburku. V tomto případě partony nevylétávají z protonu, ale jsou vytvořeny při anihilaci pozitron-elektronového páru. V nejnižším řádu poruchové teorie tento proces není vyvolán silnými interakcemi, ale elektroslabými, a dojde k tvorbě páru kvark anti-kvark: $e^+e^- \to q\bar{q}$. V koncovém stavu pak pozorujeme dva kolimované, od sebe odlétávající svazky částic, viz. obrázek 2, vlevo. Pokud kvark nebo antikvark vyzáří energetický gluon pod velkým úhlem, pozorujeme přítomnost třetího jetu viz. obrázek 2, vpravo a obrázek 3. Jde o první pozorovanou přímou manifestaci existence

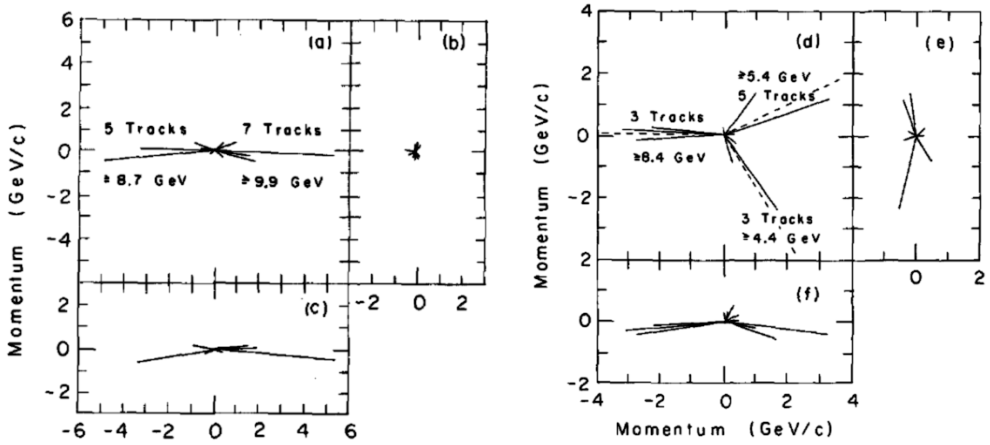

Obrázek 2: Dvou jetový případ (vlevo) a jedny z prvních tří jetových případů (vpravo) pozorované experimentem TASSO, PETRA, DESY [TASSO79].

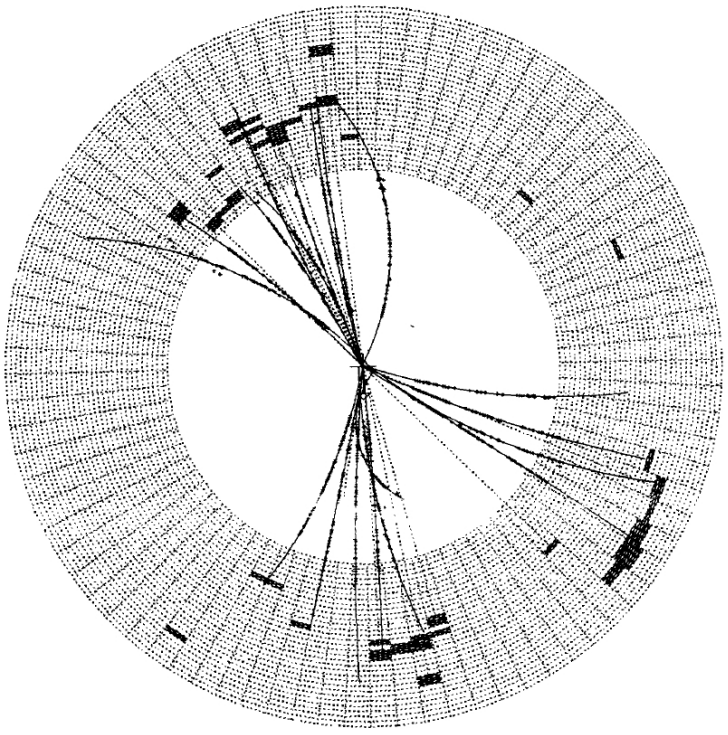

Obrázek 3: Tří jetový případ pozorovaný experimentem JADE na urychlovači PETRA, [JADE80].

gluonu (g), neboť proces tvorby tří jetů může na stromové úrovni probíhat jen jako $e^+e^- \to q\bar{q}g$. Jeden z trojice jetů tak musí pocházet z gluonu.

Anihilace e^+e^- jsou ideální laboratoří pro test kvantové chromodynamiky. Z úhlového rozdělení dvojic jetů lze ukázat, že kvarky mají spin 1/2. Tříjetové případy zase manifestují existenci gluonu a lze na nich testovat spin gluonu a jeho interakci s kvarky. Analýza čtyřjetových případů zase jasně prokázala neabelovský charakter silných interakcí. Byly tak otestovány všechny základní aspekty kvantové chromodynamiky.

I když jet není fundamentálním objektem teorie, jako třeba bodový elektron nebo kvark, hrají jety v částicové fyzice obdobnou roli. Jak bylo v této kapitole ukázáno, díky specifickým vlastnostem kvantové chromodynamiky, především díky uvěznění barevného náboje silné interakce, nemůžeme přímo měřit a detekovat vyražené partony. Vidíme jen hadronové spršky, jety, letící v původním směru rozptýlených partonů. Jety tak představují velmi důležitý nástroj, jak se dostat k informaci o energii a směru rozptylu kvarků a gluonů.

2.2 Jetové algoritmy

Aby bylo možno s pojmem jet pracovat jak po experimentální stránce tak i teoretické, je potřeba přesně definovat, jak v koncovém stavu jety vytvořit a které částice mu přiřadit. To je úkolem *jetových algoritmů*. Detailní popis problematiky jetových algoritmů na hadronových urychlovačích lze nalézt v práci [BDE+00].

První skupinu jetových algoritmů tvoří algoritmy založené na jednoduché geometrické myšlence. Do této skupiny tzv. *kuželových algoritmů* (cone algorithms) patří i algoritmus použitý pro prezentovaná měření. Jet je zde tvořen částicemi (nebo v případě experimentu jednotlivými buňkami či věžemi buněk kalorimetru), které letí do kužele o fixním poloměru R. Tento poloměr je základním parametrem algoritmu a kontroluje velikost jetu. Na hadronových urychlovačích se místo úhlové vzdálenosti používá míra $R = \sqrt{\Delta\varphi^2 + \Delta\eta^2}$. To proto, že takto definovaná vzdálenost nezávisí na boostu ve směru podél svazku.[4]

Experimenty používají z důvodu signifikantní úspory výpočetního času iterativní verzi kuželového algoritmu. Buňky kalorimetru jsou zkombinovány do projektivních věží v pseudorapiditě η a azimutálním úhlu φ. Věže s dostatečně velkým signálem nad nějakou předem zvolenou hodnotou energie E_0 slouží jako startovací pozice, kolem které se nakreslí kužel o poloměru R.

[4]Rozdíl v rapiditě je invariantní vůči boostu podél osy z a můžeme-li zanedbat hmotnosti pak pseudorapidita η splývá s rapiditou. V hadronových srážkách se těžiště tvrdé srážky individuálních partonů, která vede k tvorbě jetů, obecně pohybuje převážně ve směru osy svazků.

Částice v tomto kuželu pomocí rekombinačního schématu definují hybnost a energii jetu. Kolem nové polohy jetu se pak opět zkonstruuje kužel a proces pokračuje tak dlouho, dokud se nenalezne stabilní pozice. V konečném stádiu algoritmu je potřeba rozhodnout se, co udělat s jety, které se překrývají. Kdy je zkombinovat do jednoho a nebo naopak, kdy je brát jako dva různé jety.

Po teoretické stránce je konstrukce kuželových algoritmů problematická. Již samotná existence startovací buňky činí algoritmus náchylný na infračervené a kolineární divergence, které jsou v QCD přítomny díky nulové hmotnosti gluonu. Navíc je potřeba věnovat pozornost dalším detailům, jako je právě procedura kombinování a rozdělování překrývajících se jetů. Prezentovaná měření používají tzv. Midpoint-Cone Algorithm [BDE$^+$00], který byl navržen tak, aby většinu teoretických problémů eliminoval.

Teoreticky čistší je třída tzv. *klastrovacích algoritmů*, kdy dochází postupně k rekombinaci částic do větších celků. Algoritmus nejprve definuje vzdálenost mezi dvěma částicemi, další postup je pak obecný. Najde se nejbližší dvojice částic a pokud je vzdálenost menší než parametr algoritmu D, který kontroluje velikost jetu, tak jsou částice zrekombinovány do jedné. Opět se najde nejbližší pár a algoritmus se opakuje tak dlouho, dokud je nejmenší vzdálenost menší než parametr D. Co zůstane, je prohlášeno za jety. [5]

V případě hadronových urychlovačů byly tradičně dříve používány hlavně kuželové algoritmy a to především proto, že díky fixnímu rozměru nemají tendenci nabalovat do jetu okolní částice nesouvisející s vyraženým partonem. Těch je na hadronových urychlovačích velmi mnoho, díky vysoké luminositě svazků dochází totiž k několika srážkám najednou. Situace se změnila s nově navrženým anti-k_T klastrovacím algoritmem [CSS08], jehož míra vzdálenosti byla vhodně zvolena tak, aby k tomuto nabalování měkkých částic nedocházelo ve velké míře. Anti-k_T algoritmus se stal hlavním algoritmem, který se používá na experimentech na LHC.

[5] V případě hadronových interakcí je nutno algoritmus mírně modifikovat doplněním o vzdálenost částice ke svazku (prakticky zbytku rozbitého protonu). Detaily algoritmu jsou popsány v [BDE$^+$00].

3 Azimutální dekorelace v párové produkci jetů

Předkládaná práce [DØ05] (apendix A) se zabývá měřením azimutálních dekorelací v párové produkci jetů. V nejnižším řádu poruchové teorie jsou vyprodukované partony vybalancovány v transversální hybnosti a jsou plně korelovány v azimutu - svírají přímý úhel π, obrázek 4 vlevo. Pokud je dodatečná radiace měkká nebo kolineární s vyraženým partonem, což je nejčastější případ, dojde jen k malé změně úhlu (obrázek 4, druhý zleva). Pro popis měření na úhlech kolem $\Delta\phi_{\text{dijet}} \sim \pi$ je potřeba započítat tyto mnohonásobné emise, což je v Monte Carlo generátorech provedeno mechanismem partonové spršky.

Pokud dojde k vyzáření energetického partonu pod velkým úhlem, poruší se úhlová korelace mezi dvěma vedoucími jety, myšleno jety s největším p_{T}. V případě tří partonů v koncovém stavu musí být $\Delta\phi_{\text{dijet}} > 2\pi/3$ - obrázek 4, třetí zleva. V případě menších úhlů, $\Delta\phi_{\text{dijet}} < 2\pi/3$, je zapotřebí alespoň čtyř energetických partonů v koncovém stavu.

Rozdělení azimutálního úhlu $\Delta\phi_{\text{dijet}}$ mezi dvěma vedoucími jety tak nese informaci o širokých aspektech multipartonové emise. Jde jednak o emise spjatých s infračervenými a kolineárními divergencemi teorie ($\Delta\phi_{\text{dijet}} \sim \pi$), tak i tvrdé energetické emise pod velkými úhly. Proto se naměřená data často využívají pro testování a ladění parametrů modelů partonových sprškek, tak jak jsou implementovány v různých Monte Carlo generátorech, jako například Pythia, Pomwig [SKP+11], Sherpa [G+09] a dalších: [CS11], [Fie11], [BBG+11], [Ska10], [ATLAS11], [BHL+10] a [AGH+08].

Už naše původní práce poukázala na velké nesrovnalosti mezi předpověmi Pythia6.225 a daty, obrázek 5, vlevo. Bylo nutné změnou parametru, který kontroluje maximální virtualitu partonů ve sprše, zvýšit množství ra-

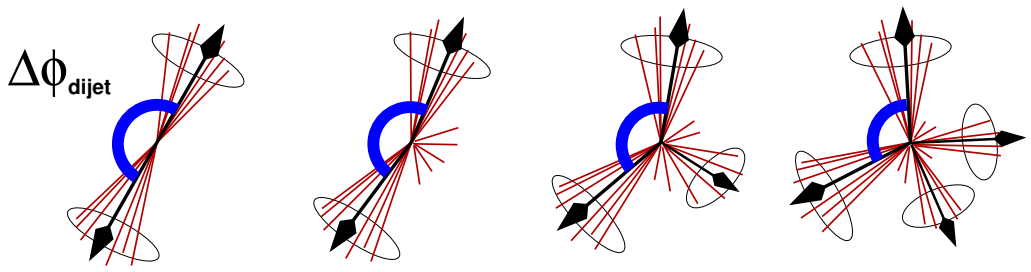

Obrázek 4: Změna azimutálního úhlu mezi dvěma vedoucími jety v závislosti na množství dodatečné radiace, [Kup05].

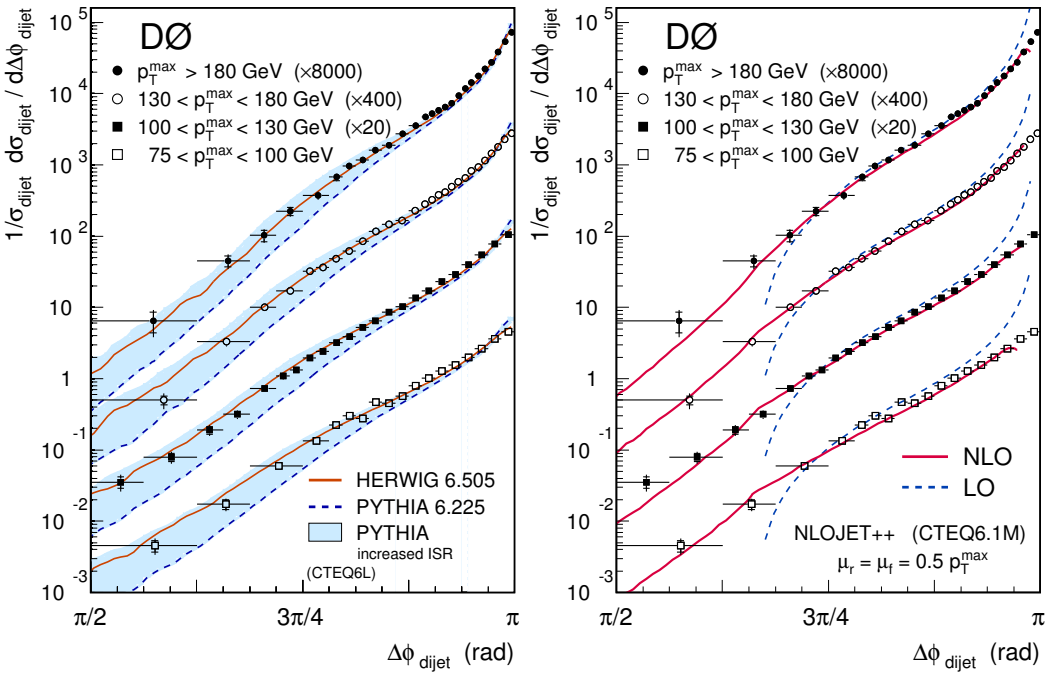

Obrázek 5: Porovnání změřeného rozdělení azimutálního úhlu mezi dvěmi vedoucími jety s předpovědmi Monte Carlo generátorů HERWIGa PYTHIA, [DØ05]. (vlevo) a předpovědí NLO QCD (vpravo)

diace v počátečním stavu (tzv. initial state radiation - ISR), aby se dosáhlo souhlasu s pozorovanými daty.

Dalším aspektem práce bylo porovnání dat s druhým řádem poruchového rozvoje QCD (NLO QCD). Bylo to vůbec první měření z hadronového urychlovače, na kterém bylo provedeno srovnání s NLO QCD předpovědí pro tří jetové veličiny. Tyto teoretické výpočty nebyly v době prvních dat z Tevatron (tzv. Run I) k dispozici. Technicky byly implementovány do programu NLOJET++ [Nag03]. NLO QCD předpovědi vykazují dobrý souhlas s experimentálními daty v téměř celé oblasti hodnot $\Delta\phi_{\text{dijet}}$, samozřejmě mimo oblast $\Delta\phi_{\text{dijet}} \sim \pi$, jejíž popis vyžaduje resumaci mnohonásobných emisí, obrázek 5, vpravo.

Díky dostupným NLO QCD výpočtům pro procesy s třemi partony v koncovém stavu lze na hadronových urychlovačích měřit hodnotu α_S z tří jetových veličin. Tématem se zabýval pod mým vedením v rámci své diplomové práce Oldřich Kepka [Kep05]. Dnes je extrakce vazbového parametru silné interakce α_S z tří-jetvých veličin na hadronových urychlovačích standardním přístupem, viz. obrázek 1.

4 Inkluzivní produkce jetů

Měření inkluzivní produkce jetů v závislosti na jejich příčné hybnosti p_{T} je jednou ze základních veličin zkoumaných na hadronových urychlovačích. Lze na ni přímo testovat předpovědi kvantové chromodynamiky a to až do vůbec největších dostupných hodnot p_{T}. Můžeme tak přímo ověřit naše představy o hmotě na nejmenších dostupných škálách.

První měření inkluzivního spektra jetů provedené experimentem CDF na Tevatronu při těžišťové energii $\sqrt{s} = 1{,}8\,\mathrm{TeV}$ [CDF96] ukazovalo na zvýšenou produkci jetů při vysokých hodnotách p_{T}, viz. obrázek 6. Data byla interpretována jako možný náznak nové fyziky, konkrétně jako projev efektivní 4-kvarkové interakce (tzv. *quark compositeness*). Interpretace nebyla jednoznačná, protože k vysvětlení pozorované skutečnosti stačilo zvýšit ve strukturních funkcích protonu obsah gluonů nesoucí velkou část hybnosti protonu x. Gluonová distribuční funkce při velkých x nebyla totiž z ostatních měření dostatečně přesně určená.

Detailní prozkoumání produkce jetů při vysokých hodnotách p_{T} bylo hlavní motivací předkládaných prací [DØ08] (apendix B) a [DØ12] (apendix C). Vyšší luminosita a mírně vyšší těžišťová energie srážky dovolila nabrat víc jak 20× případů s velmi vysokým p_{T}.

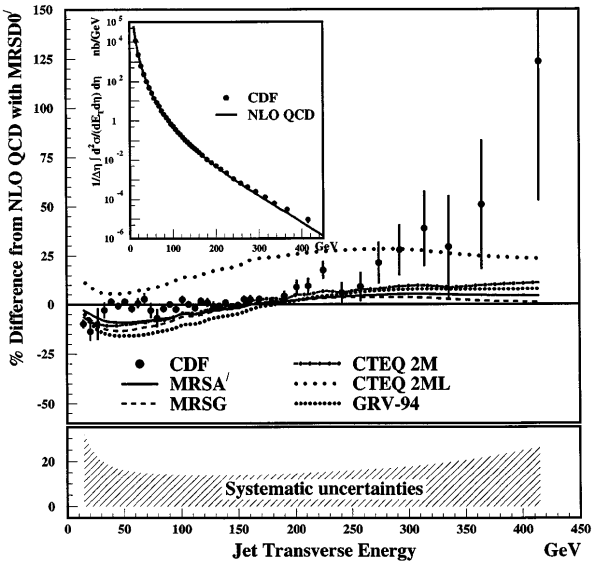

Obrázek 6: Poměr inkluzivní produkce jetů k teoretické NLO QCD předpovědi jak byla změřena experiment CDF v Run I v proton-antiprotonových interakcích při $\sqrt{s} = 1.8\,\mathrm{TeV}$ [CDF96].

4.1 Energetická kalibrace jetů

Po experimentální stránce je dominantní systematickou chybou neurčitost v energetické kalibraci jetů, viz. Apendix C, obrázek 45. Účinný průřez produkce jetů totiž s rostoucím p_{T} prudce klesá a tak malá změna v určení energie jetů znamená velkou změnu ve výsledném měření produkce. Kvalita energetické kalibrace tak přímo určuje výslednou kvalitu měření produkce jetů.

Z těchto důvodů jsem se energetickou kalibrací jetů v rámci *DØ Jet Energy Scale* skupiny několik let intenzivně zabýval. Jednak jsem měřil přímo odezvu kalorimetru na jet v případech, kdy spolu s jetem vznikl foton, viz. Apendix C, kapitola V, oddíl B. Foton tvoří, obdobně jako elektron, v kalorimetru elektromagnetickou spršku. Ty lze velmi přesně zkalibrovat pomocí rozpadu $Z \to e^+e^-$. Odezva kalorimetru na jet se pak v $\gamma +$ jet případech určí tak, aby jet vybalancoval příčnou hybnost fotonu.

In situ kalibrace DØ kalorimetru byla nutná, protože kalorimetr nebyl nikdy přímo proměřen na testovacích svazcích. To byl problém i pro Monte Carlo simulace detektoru DØ, které zdaleka nepopisovaly skutečnou odezvu detektoru na jet. Standardní Monte Carlo tak nebylo možné použít na některé důležité korekce, respektive by vedlo k příliš velké systematické chybě, například pro korekci vůči jinému poměru kvarkových a gluonových jetů v kalibračním vzorku $\gamma +$ jet případů a měřeném inkluzivním vzorku. Stejně tak bylo nutné spolehnout se bez dobré simulace detektoru na extrapolaci kalibrace jetů z $\gamma +$jet případů, které dosahovaly $p_{\mathrm{T}} \sim 200\,\mathrm{GeV}$ do hodnot až nad 600 GeV, kterých dosahovaly jety v inkluzivním souboru dat.

Vyvinuli jsme metodu jak vyladit Monte Carlo simulace odezvy DØ kalorimetru tak, aby lépe popisovala skutečnost. Díky ní jsme mohli zpřesnit extrapolaci kalibrace pro nejenergetičtější jety a výrazně tak zpřesnit měření produkce jetů na největších hodnotách p_{T}. Stejně tak jsme mohli lépe provézt korekci na rozdílný obsah kvarkových a gluonových jetů v měřeném inkluzivním souboru dat a vybraných kalibračních $\gamma +$jet případech, viz. Apendix C, obrázky 12 a 13. Stejná metoda pak byla použita pro zpřesnění energetické kalibrace jetů iniciovaných b kvarkem, což nakonec vedlo k přesnějšímu měření hmotnosti top kvarku [DØ11].

Zabýval jsem se také určením a propagací korelací chyb kalibrace mezi jety s různým p_{T} a y. Ty pak sloužily jako podklad pro výpočet korelací mezi chybami produkce jetů v různých oblastech p_{T} a y, Apendix B, obrázek 3. Tato informace je nezbytná pro skupiny zabývající se extrakcí partonových strukturních funkcí. Stejně tak je informace důležitá i pro jiná měření, přímo ovlivňuje limity získané z dat pro různé modely nové fyziky jdoucí za rámec standardního modelu.

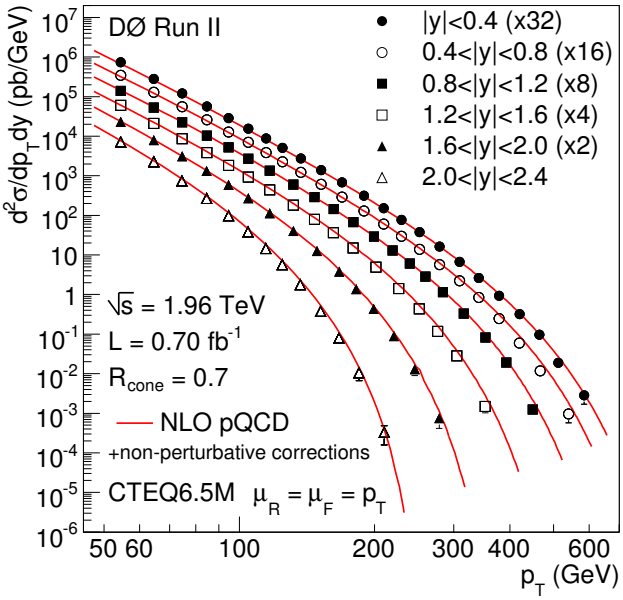

Obrázek 7: Inlusivní produkce jetů změřená experimentem DØ v $p\bar{p}$ srážkách při $\sqrt{s} = 1{,}96$ TeV, [DØ08] (apendix B).

V letech 2006-2008 jsem také vedl DØ Jet Energy Scale skupinu. V tomto období se nám podařilo finalizovat energetickou kalibraci jetů s velmi malou chybou, která pro centrální jety byla pod 1.5% pro téměř všechny hodnoty p_{T}, viz. Apendix C, obrázek 21. To nám pak umožnilo provést jedno z nejpřesnějších měření inkluzivní produkce jetů. Výsledná systematická chyba byla asi poloviční oproti předchozím publikovaným měřením CDF a DØ [CDF96, DØ99, DØ01, CDF06, CDF07].

4.2 Výsledky měření

Inkluzivní produkce jetů byla měřena v 6 binech rapidity y. To by umožnilo rozlišit případné signály nové fyziky od efektů spojených s neznalostí strukturních funkcí. Předpokládá se, že nové částice či interakce by se projevily nejvíce právě v centrální části, kdy dochází k největším přenosům hybnosti. Naopak produkce jetů při velkých hodnotách rapidity by neměla být novou fyzikou tolik ovlivněna.

NLO QCD předpovědi vykazují z daty výborný souhlas v celém rozsahu transversálních hybností a rapidity, obrázky 7 a 8. V rozmezí $p_{\mathrm{T}} = 50\,\mathrm{GeV}$ až $600\,\mathrm{GeV}$ padá účinný průřez o víc jak 8 řádů a přesto zůstává souhlas mezi teorií a měřením v rámci 10-20% experimentálních a teoretických chyb. Výborného souhlasu je dosaženo hlavně při použití MRST2004 partonových

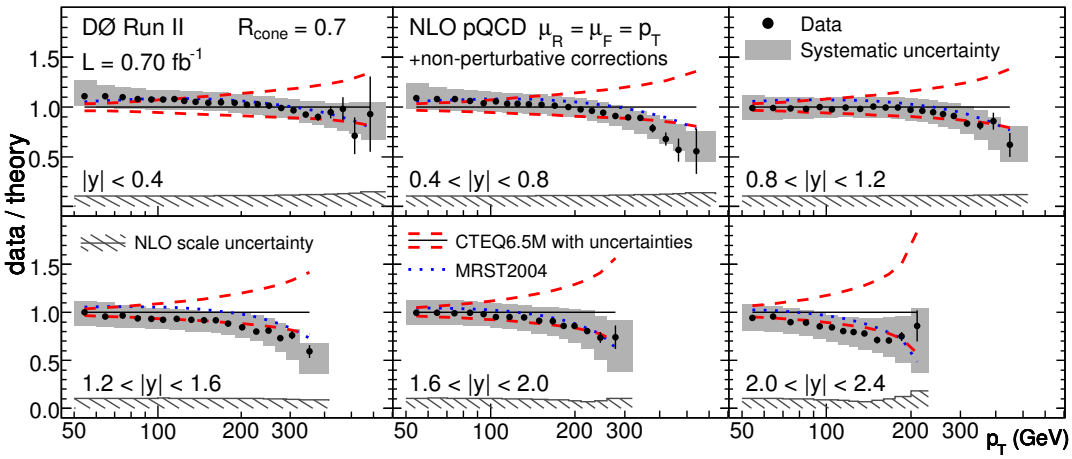

Obrázek 8: Porovnání inkluzivní produkce jetů změřené experimentem DØ s předpovědí NLO QCD, [DØ08] (apendix B).

distribučních funkci [MRST04]. Nepotvrdila se tak interpretace prvního měření experimentu CDF [CDF96] jako signál nové fyziky. Kvarky a gluony se zdají bodové a chovají se podle QCD až do nejvyšších hodnot $p_{\mathrm{T}} \sim 600\,\mathrm{GeV}$, což řádově odpovídá asi tisícině rozměru protonu.

Měření z Tevatronu jsou důležité i pro interpretaci novějších dat z urychlovače LHC, jehož objevitelský potenciál je díky vyšší těžišťové energii srážky větší. Případný nesouhlas dat s teorií by šel jednoznačněji interpretovat jako signál nové fyziky. Nejnovější měření experimentů ATLAS a CMS na urychlovači LHC potvrdily platnost QCD až do energetické škály 2 TeV [ATLAS12, CMS11, CMS13].

Experimentální přesnost měření byla v oblasti vyskokých p_{T} menší než nepřesnosti spojené s neznalostí partonových distribučních funkcí, viz. přerušované čáry na obrázku 8. Získaná data tak nesou novou informaci o složení protonu, především o gluonech nesoucí velkou část hybnosti protonu. Naše měření používají skupiny zabývající se globálním určováním partonových distribučních funkcí, kde je nutné zkombinovat velké množství dat z ruzných experimentů, aby bylo možno jednotlivé komponenty protonu spolehlivě extrahovat [MSTW09, LGH$^+$10].

Impaktu tohoto měření na znalost gluonové distribuční funkce je věnována jedna kapitola v práci skupiny MSTW [MSTW09]. Autoři konstatují mnohem lepší konzistenci nového měření inkluzivního spektra jetů s ostatními experimenty než tomu bylo u předchozích měření z Tevatronu. Není podle nich nutné zavádět speciální proceduru, jak tomu bylo v předchozích globálních fitech, která navýšila obsah gluonu při vysokých hodnotách x a umožnila tak

lepší popis starších dat z Tevatronu při $\sqrt{s} = 1{,}8\,\mathrm{TeV}$. Dochází však k závěru, že zahrnutí nových dat vede jen k mírnému zmenšení neurčitosti gluonové distribuční funkce, než jak by napovídaly malé experimentální chyby. Důvodem je vysoké množství signifikantních zdrojů různých systematických chyb s vysokou korelací. Ukázala se tak důležitost naší podrobné analýzy systematických chyb.

5 Modifikace klastrového hadronizačního modelu

Herwig a Pythia jsou jedny z nejpoužívanějších obecných Monte Carlo generátorů srážek částic. Liší se v mnoha aspektech, což je cenné pro odhad chyb spjatých s modelováním jevů, které nedokážeme přímo spočítat z původního Lagrangiánu QCD. Jedním z takových jevů je proces hadronizace, ke kterému dochází ve finální fázi srážky. Mechanismus tohoto procesu byl v hrubých rysech načrtnut v podkapitole 2.1.

Hadronizační model programů Pythia a Herwig se od sebe liší. Model Pythia je založen na fragmentaci struny natahující se mezi dvěma částicemi nesoucí barvu. Je motivován neporuchovými výpočty na mříži, které ukazují, že se skutečně mezi vzdalujícími barevnými náboji pole koncentruje do relativně tenké struny spojující tyto náboje.

Hadronizace v Herwig je založena na jednodušším tzv. *klastrovém modelu*. Objekty nesoucí barvu jsou spojeny v párech do bezbarvých klastrů, jeden objekt nese barvu, druhý příslušnou anti-barvu. Klastry se pak generováním dalších párů barva-antibarva rozpadají na další bezbarvé klastry, dokud jejich invariantní hmotnost neklesne pod určitou mez. Poté se tyto finální klastry nechají rozpadnou na dvojici hadronů, tím, že se z vakua vygeneruje pár kvark-antikvark nebo pár dikvark-antidikvark, což je nutné pro produkci baryonů v koncovém stavu.

Při studiu původního klastrového modelu Herwig5.9 jsem si všimnul podivného chování, pokud se do modelu zahrnou těžší resonance. Navrhnul jsem modifikaci modelu hadrnonizace, která by napravila toto chování a umožnila by simulovat i produkci těžších resonancí, například hadronu $\Lambda(1520)$, [Kup98] (Apendix D). Model byl dále rozvinut Winterem, Kraussem a Soffem [WKS04] a posléze byl implementován v novějších verzích generátoru Herwig [BGG+08].

6 Shrnutí

Prezentovaná habilitační práce shrnuje můj hlavní příspěvek k fyzikálnímu programu experimentu DØ v oblasti fyziky jetů. Týkala se jednak aspektu mnohonásobných partonových emisí (měření azimutálních korelací v párové produkci jetů), testování kvantové chromodynamiky na nejmenších rozměrových škálách (měření inklusivní produkce jetů), tak i experimentální problematiky spjaté s energetickou kalibrací jetů. Kromě toho byla prezentována má samostatná práce týkající se návrhu modifikovaného klastrového hadronizačního modelu pro Monte Carlo generátor HERWIG.

V habilitační práci jsem se snažil konkretizovat můj podíl na dosažených výsledcích v rámci experimentu DØ. Dále jsem se snažil zařadit tyto výsledky do širšího rámce částicové fyziky a načrtnout jejich impakt a význam, který v tomto oboru zanechaly.

Experimentální výsledky potvrdily platnost kvantové chromodynamiky i na těch největších dostupných energetických škálách. Data také upřesnila naše představy o struktuře protonu, především o gluonech, které nesou velkou část hybnosti protonu. Měření úhlových dekorelací v párové produkci jetů pak slouží jako jedno ze základních rozdělení pro ladění parametrů modelů partonových sprškek.

Reference

[AGH+08] J. Archibald, T. Gleisberg, S. Hoeche, F. Krauss, M. Schonherr et al., *Recent developments in SHERPA*, Nucl.Phys.Proc.Suppl. **183**, 60–66 (2008).

[ATLAS11] G. Aad et al. (ATLAS Collaboration), *ATLAS tunes of PYTHIA 6 and Pythia 8 for MC11*, (2011), ATL-PHYS-PUB-2011-009, ATL-COM-PHYS-2011-744.

[ATLAS12] G. Aad et al. (ATLAS Collaboration), *Measurement of inclusive jet and dijet production in pp collisions at $\sqrt{s} = 7$ TeV using the ATLAS detector*, Phys.Rev. **D86**, 014022 (2012), 1112.6297.

[BBG+11] A. Buckley, J. Butterworth, S. Gieseke, D. Grellscheid, S. Hoche et al., *General-purpose event generators for LHC physics*, Phys.Rept. **504**, 145–233 (2011), 1101.2599.

[BCD+69] E. D. Bloom, D. Coward, H. DeStaebler, J. Drees, G. Miller et al., *High-Energy Inelastic e p Scattering at 6-Degrees and 10-Degrees*, Phys.Rev.Lett. **23**, 930–934 (1969).

[BDE+00] G. Blazey, J. Dittmann, S. Ellis, D. Elvira, K. Frame, S. Grinstein, R. Hirosky, R. Piegaia, H. Schellman, R. Snihur, V. Sorin and D. Zeppenfeld, *Run II Jet Physics: Proceedings of the Run II QCD and Weak Boson Physics Workshop*, (2000), hep-ex/0005012v2.

[BFK+69] M. Breidenbach, J. I. Friedman, H. W. Kendall, E. D. Bloom, D. Coward et al., *Observed Behavior of Highly Inelastic electron-Proton Scattering*, Phys.Rev.Lett. **23**, 935–939 (1969).

[BGG+08] M. Bahr, S. Gieseke, M. Gigg, D. Grellscheid, K. Hamilton et al., *Herwig++ Physics and Manual*, Eur.Phys.J. **C58**, 639–707 (2008), 0803.0883.

[BHL+10] A. Buckley, H. Hoeth, H. Lacker, H. Schulz and J. E. von Seggern, *Systematic event generator tuning for the LHC*, Eur.Phys.J. **C65**, 331–357 (2010), 0907.2973.

[CDF96] F. Abe et al. (CDF Collaboration), *Inclusive Jet Cross Section in $\overline{p}p$ Collisions at $s = 1.8$TeV*, Phys. Rev. Lett. **77**, 438–443 (Jul 1996).

[CDF06] A. Abulencia et al. (CDF Collaboration), *Measurement of the inclusive jet cross section in $p\bar{p}$ interactions at $\sqrt{s} = 1.96$ TeV using a cone-based jet algorithm*, Phys. Rev. D **74**, 071103 (Oct 2006).

[CDF07] A. Abulencia et al. (CDF Collaboration), *Measurement of the inclusive jet cross section using the k_{T} algorithm in $p\bar{p}$ collisions at $\sqrt{s} = 1.96$ TeV with the CDF II detector*, Phys. Rev. D **75**, 092006 (May 2007).

[CMS11] S. Chatrchyan et al. (CMS Collaboration), *Measurement of the Inclusive Jet Cross Section in pp Collisions at $\sqrt{s} = 7$ TeV*, Phys.Rev.Lett. **107**, 132001 (2011), 1106.0208.

[CMS12] S. Chatrchyan et al. (CMS Collaboration), *Measurement of the 3-jet mass cross section at 7 TeV and determination of the strong coupling constant from 3-jet masses in the TeV range*, CMS Public Note: CMS-PAS-SMP-12-027 (2012).

[CMS13] S. Chatrchyan et al. (CMS Collaboration), *Measurements of differential jet cross sections in proton-proton collisions at $\sqrt{s}$=7 TeV with the CMS detector*, Phys. Rev. D **87**, 112002 (Jun 2013).

[CS11] R. Corke and T. Sjostrand, *Interleaved Parton Showers and Tuning Prospects*, JHEP **1103**, 032 (2011), 1011.1759.

[CSS08] M. Cacciari, G. P. Salam and G. Soyez, *The Anti-k(t) jet clustering algorithm*, JHEP **0804**, 063 (2008), 0802.1189.

[DØ99] B. Abbott et al. (DØ Collaboration), *Inclusive Jet Cross Section in $\overline{p}p$ Collisions at $\sqrt{s} = 1.8$TeV*, Phys. Rev. Lett. **82**, 2451–2456 (Mar 1999).

[DØ01] B. Abbott et al. (DØ Collaboration), *Inclusive Jet Production in $p\overline{p}$ Collisions*, Phys. Rev. Lett. **86**, 1707–1712 (Feb 2001).

[DØ05] V. Abazov et al. (DØ Collaboration), *Measurement of dijet azimuthal decorrelations at central rapidities in $p\bar{p}$ collisions at $\sqrt{s} = 1.96$ TeV*, Phys.Rev.Lett. **94**, 221801 (2005), hep-ex/0409040.

[DØ08] V. Abazov et al. (DØ Collaboration), *Measurement of the inclusive jet cross-section in $p\bar{p}$ collisions at $s^{91/2)}$ =1.96-TeV*, Phys.Rev.Lett. **101**, 062001 (2008), 0802.2400.

[DØ11] V. M. Abazov et al. (DØ Collaboration), *Precise measurement of the top-quark mass from lepton+jets events at DØ*, Phys.Rev. **D84**, 032004 (2011), 1105.6287.

[DØ12] V. M. Abazov et al. (DØ Collaboration), *Measurement of the inclusive jet cross section in $p\bar{p}$ collisions at $\sqrt{s} = 1.96$ TeV*, Phys.Rev. **D85**, 052006 (2012), 1110.3771.

[Fey73] R. Feynman, *Photon-hadron interactions*, (1973).

[FH12] Z. Fodor and C. Hoelbling, *Light Hadron Masses from Lattice QCD*, Rev.Mod.Phys. **84**, 449 (2012), 1203.4789.

[Fie11] R. Field, *Min-Bias and the Underlying Event at the LHC*, Acta Phys.Polon. **B42**, 2631–2656 (2011), 1110.5530.

[G+09] T. Gleisberg et al., *Event generation with SHERPA 1.1*, JHEP **02**, 007 (2009), 0811.4622.

[GM64] M. Gell-Mann, *A Schematic Model of Baryons and Mesons*, Phys.Lett. **8**, 214–215 (1964).

[GW73] D. Gross and F. Wilczek, *Ultraviolet Behavior of Nonabelian Gauge Theories*, Phys.Rev.Lett. **30**, 1343–1346 (1973).

[JADE80] W. Bartel et al. (JADE Collaboration), *Observation of planar three-jet events in e^+e^- annihilation and evidence for gluon bremsstrahlung*, Physics Letters B **91**, 142–147 (March 1980).

[Kep05] O. Kepka, *The QCD analysis of multijet events in proton-antiproton collisions at the Tevatron*, (2005), diploma thesis, Charles University in Prague.

[Kup98] A. Kupco, *Cluster hadronization in HERWIG 5.9*, (1998), hep-ph/9906412.

[Kup04] A. Kupco, *Recent QCD results from DØ*, Eur. Phys. J. **C33**, s419–s421 (2004).

[Kup05] A. Kupco, *Latest jets results from the Tevatron at $\sqrt{s} = 1.96$-TeV*, (2005), hep-ex/0506038.

[Kup07] A. Kupco, Inclusive Jet Production from the Tevatron, in *High Energy Physics ICHEP '06*, edited by Y. Sissakian, G. Kozlov and E. Kolganova, pages 465–468, November 2007.

[LGH+10] H.-L. Lai, M. Guzzi, J. Huston, Z. Li, P. M. Nadolsky et al., *New parton distributions for collider physics*, Phys.Rev. **D82**, 074024 (2010), 1007.2241.

[MH56] R. Mcallister and R. Hofstadter, *ELASTIC SCATTERING OF 188-MEV ELECTRONS FROM THE PROTON AND THE ALPHA PARTICLE*, Phys.Rev. **102**, 851–856 (1956).

[MRST04] A. D. Martin, R. G. Roberts, W. J. Stirling and R. S. Thorne, *Physical gluons and high-E_T jets*, Physics Letters B **604**, 61–68 (December 2004), arXiv:hep-ph/0410230.

[MSTW09] A. Martin, W. Stirling, R. Thorne and G. Watt, *Parton distributions for the LHC*, Eur.Phys.J. **C63**, 189–285 (2009), 0901.0002.

[Nag03] Z. Nagy, *Next-to-leading order calculation of three jet observables in hadron hadron collision*, Phys.Rev. **D68**, 094002 (2003), hep-ph/0307268.

[Pol73] H. D. Politzer, *Reliable Perturbative Results for Strong Interactions?*, Phys.Rev.Lett. **30**, 1346–1349 (1973).

[Ska10] P. Z. Skands, *Tuning Monte Carlo Generators: The Perugia Tunes*, Phys.Rev. **D82**, 074018 (2010), 1005.3457.

[SKP+11] A. S., H. K., N. P., O. C. and R. E., *Jet pair production in POWHEG*, JHEP **1104**, 081 (2011).

[TASSO79] R. Brandelik et al. (TASSO Collaboration), *Evidence for Planar Events in e+ e- Annihilation at High-Energies*, Phys.Lett. **B86**, 243 (1979).

[WKS04] J.-C. Winter, F. Krauss and G. Soff, *A Modified cluster hadronization model*, Eur.Phys.J. **C36**, 381–395 (2004), hep-ph/0311085.

[Zwe64] G. Zweig, *An SU(3) model for strong interaction symmetry and its breaking*, (1964), CERN-TH-401.

Measurement of Dijet Azimuthal Decorrelations at Central Rapidities in $p\bar{p}$ Collisions at $\sqrt{s} = 1.96$ TeV

V. M. Abazov,[33] B. Abbott,[70] M. Abolins,[61] B. S. Acharya,[27] D. L. Adams,[68] M. Adams,[48] T. Adams,[46] M. Agelou,[17] J.-L. Agram,[18] S. N. Ahmed,[32] S. H. Ahn,[29] G. D. Alexeev,[33] G. Alkhazov,[37] A. Alton,[60] G. Alverson,[59] G. A. Alves,[2] M. Anastasoaie,[32] S. Anderson,[42] B. Andrieu,[16] Y. Arnoud,[13] A. Askew,[73] B. Åsman,[38] O. Atramentov,[53] C. Autermann,[20] C. Avila,[7] L. Babukhadia,[67] T. C. Bacon,[40] F. Badaud,[12] A. Baden,[57] S. Baffioni,[14] B. Baldin,[47] P. W. Balm,[31] S. Banerjee,[27] E. Barberis,[59] P. Bargassa,[73] P. Baringer,[54] C. Barnes,[40] J. Barreto,[2] J. F. Bartlett,[47] U. Bassler,[16] D. Bauer,[51] A. Bean,[54] S. Beauceron,[16] F. Beaudette,[15] M. Begel,[66] A. Bellavance,[63] S. B. Beri,[26] G. Bernardi,[16] R. Bernhard,[47,*] I. Bertram,[39] M. Besançon,[17] A. Besson,[18] R. Beuselinck,[40] V. A. Bezzubov,[36] P. C. Bhat,[47] V. Bhatnagar,[26] M. Bhattacharjee,[67] M. Binder,[24] A. Bischoff,[45] K. M. Black,[58] I. Blackler,[40] G. Blazey,[49] F. Blekman,[31] S. Blessing,[46] D. Bloch,[18] U. Blumenschein,[22] A. Boehnlein,[47] O. Boeriu,[52] T. A. Bolton,[55] P. Bonamy,[17] F. Borcherding,[47] G. Borissov,[39] K. Bos,[31] T. Bose,[65] C. Boswell,[45] A. Brandt,[72] G. Briskin,[71] R. Brock,[61] G. Brooijmans,[65] A. Bross,[47] N. J. Buchanan,[46] D. Buchholz,[50] M. Buehler,[48] V. Buescher,[22] S. Burdin,[47] T. H. Burnett,[75] E. Busato,[16] J. M. Butler,[58] J. Bystricky,[17] F. Canelli,[66] W. Carvalho,[3] B. C. K. Casey,[71] D. Casey,[61] N. M. Cason,[52] H. Castilla-Valdez,[30] S. Chakrabarti,[27] D. Chakraborty,[49] K. M. Chan,[66] A. Chandra,[27] D. Chapin,[71] F. Charles,[18] E. Cheu,[42] L. Chevalier,[17] D. K. Cho,[66] S. Choi,[45] S. Chopra,[68] T. Christiansen,[24] L. Christofek,[54] D. Claes,[63] A. R. Clark,[43] B. Clément,[18] C. Clément,[38] Y. Coadou,[5] D. J. Colling,[40] L. Coney,[52] B. Connolly,[46] M. Cooke,[73] W. E. Cooper,[47] D. Coppage,[54] M. Corcoran,[73] J. Coss,[19] A. Cothenet,[14] M.-C. Cousinou,[14] S. Crépé-Renaudin,[13] M. Cristetiu,[45] M. A. C. Cummings,[49] D. Cutts,[71] H. da Motta,[2] B. Davies,[39] G. Davies,[40] G. A. Davis,[50] K. De,[72] P. de Jong,[31] S. J. de Jong,[32] E. De La Cruz-Burelo,[30] C. De Oliveira Martins,[3] S. Dean,[41] K. Del Signore,[60] F. Déliot,[17] P. A. Delsart,[19] M. Demarteau,[47] R. Demina,[66] P. Demine,[17] D. Denisov,[47] S. P. Denisov,[36] S. Desai,[67] H. T. Diehl,[47] M. Diesburg,[47] M. Doidge,[39] H. Dong,[67] S. Doulas,[59] L. Duflot,[15] S. R. Dugad,[27] A. Duperrin,[14] J. Dyer,[61] A. Dyshkant,[49] M. Eads,[49] D. Edmunds,[61] T. Edwards,[41] J. Ellison,[45] J. Elmsheuser,[24] J. T. Eltzroth,[72] V. D. Elvira,[47] S. Eno,[57] P. Ermolov,[35] O. V. Eroshin,[36] J. Estrada,[47] D. Evans,[40] H. Evans,[65] A. Evdokimov,[34] V. N. Evdokimov,[36] J. Fast,[47] S. N. Fatakia,[58] D. Fein,[42] L. Feligioni,[58] T. Ferbel,[66] F. Fiedler,[24] F. Filthaut,[32] W. Fisher,[64] H. E. Fisk,[47] F. Fleuret,[16] M. Fortner,[49] H. Fox,[22] W. Freeman,[47] S. Fu,[47] S. Fuess,[47] C. F. Galea,[32] E. Gallas,[47] E. Galyaev,[52] M. Gao,[65] C. Garcia,[66] A. Garcia-Bellido,[75] J. Gardner,[54] V. Gavrilov,[34] P. Gay,[12] D. Gelé,[18] R. Gelhaus,[45] K. Genser,[47] C. E. Gerber,[48] Y. Gershtein,[71] G. Geurkov,[71] G. Ginther,[66] K. Goldmann,[25] T. Golling,[21] B. Gómez,[7] K. Gounder,[47] A. Goussiou,[52] G. Graham,[57] P. D. Grannis,[67] S. Greder,[18] J. A. Green,[53] H. Greenlee,[47] Z. D. Greenwood,[56] E. M. Gregores,[4] S. Grinstein,[1] Ph. Gris,[12] J.-F. Grivaz,[15] L. Groer,[65] S. Grünendahl,[47] M. W. Grünewald,[28] W. Gu,[6] S. N. Gurzhiev,[36] G. Gutierrez,[47] P. Gutierrez,[70] A. Haas,[65] N. J. Hadley,[57] H. Haggerty,[47] S. Hagopian,[46] I. Hall,[70] R. E. Hall,[44] C. Han,[60] L. Han,[41] K. Hanagaki,[47] P. Hanlet,[72] K. Harder,[55] R. Harrington,[59] J. M. Hauptman,[53] R. Hauser,[61] C. Hays,[65] J. Hays,[50] T. Hebbeker,[20] C. Hebert,[54] D. Hedin,[49] J. M. Heinmiller,[48] A. P. Heinson,[45] U. Heintz,[58] C. Hensel,[54] G. Hesketh,[59] M. D. Hildreth,[52] R. Hirosky,[74] J. D. Hobbs,[67] B. Hoeneisen,[11] M. Hohlfeld,[23] S. J. Hong,[29] R. Hooper,[71] S. Hou,[60] P. Houben,[31] Y. Hu,[67] J. Huang,[51] Y. Huang,[60] I. Iashvili,[45] R. Illingworth,[47] A. S. Ito,[47] S. Jabeen,[54] M. Jaffré,[15] S. Jain,[70] V. Jain,[68] K. Jakobs,[22] A. Jenkins,[40] R. Jesik,[40] Y. Jiang,[60] K. Johns,[42] M. Johnson,[47] P. Johnson,[42] A. Jonckheere,[47] P. Jonsson,[40] H. Jöstlein,[47] A. Juste,[47] M. M. Kado,[43] D. Käfer,[20] W. Kahl,[55] S. Kahn,[68] E. Kajfasz,[14] A. M. Kalinin,[33] J. Kalk,[61] D. Karmanov,[35] J. Kasper,[58] D. Kau,[46] Z. Ke,[6] R. Kehoe,[61] S. Kermiche,[14] S. Kesisoglou,[71] A. Khanov,[66] A. Kharchilava,[52] Y. M. Kharzheev,[33] K. H. Kim,[29] B. Klima,[47] M. Klute,[21] J. M. Kohli,[26] M. Kopal,[70] V. M. Korablev,[36] J. Kotcher,[68] B. Kothari,[65] A. V. Kotwal,[65] A. Koubarovsky,[35] O. Kouznetsov,[13] A. V. Kozelov,[36] J. Kozminski,[61] J. Krane,[53] M. R. Krishnaswamy,[27] S. Krzywdzinski,[47] M. Kubantsev,[55] S. Kuleshov,[34] Y. Kulik,[47] S. Kunori,[57] A. Kupco,[17] T. Kurča,[19] V. E. Kuznetsov,[45] S. Lager,[38] N. Lahrichi,[17] G. Landsberg,[71] J. Lazoflores,[46] A.-C. Le Bihan,[18] P. Lebrun,[19] S. W. Lee,[29] W. M. Lee,[46] A. Leflat,[35] C. Leggett,[43] F. Lehner,[47,*] C. Leonidopoulos,[65] P. Lewis,[40] J. Li,[72] Q. Z. Li,[47] X. Li,[6] J. G. R. Lima,[49] D. Lincoln,[47] S. L. Linn,[46] J. Linnemann,[61] V. V. Lipaev,[36] R. Lipton,[47] L. Lobo,[40] A. Lobodenko,[37] M. Lokajicek,[10] A. Lounis,[18] J. Lu,[6] H. J. Lubatti,[75] A. Lucotte,[13] L. Lueking,[47] C. Luo,[51] M. Lynker,[52] A. L. Lyon,[47] A. K. A. Maciel,[49] R. J. Madaras,[43] P. Mättig,[25] A. Magerkurth,[60] A.-M. Magnan,[13] M. Maity,[58] N. Makovec,[15] P. K. Mal,[27] S. Malik,[56] V. L. Malyshev,[33] V. Manankov,[35] H. S. Mao,[6] Y. Maravin,[47] T. Marshall,[51] M. Martens,[47] M. I. Martin,[49] S. E. K. Mattingly,[71] A. A. Mayorov,[36] R. McCarthy,[67] R. McCroskey,[42] T. McMahon,[69] D. Meder,[23] H. L. Melanson,[47] A. Melnitchouk,[62] X. Meng,[6] M. Merkin,[35] K. W. Merritt,[47] A. Meyer,[20] C. Miao,[71]

H. Miettinen,[73] D. Mihalcea,[49] J. Mitrevski,[65] N. Mokhov,[47] J. Molina,[3] N. K. Mondal,[27] H. E. Montgomery,[47] R. W. Moore,[5] M. Mostafa,[1] G. S. Muanza,[19] M. Mulders,[47] Y. D. Mutaf,[67] E. Nagy,[14] F. Nang,[42] M. Narain,[58] V. S. Narasimham,[27] N. A. Naumann,[32] H. A. Neal,[60] J. P. Negret,[7] S. Nelson,[46] P. Neustroev,[37] C. Noeding,[22] A. Nomerotski,[47] S. F. Novaes,[4] T. Nunnemann,[24] E. Nurse,[41] V. O'Dell,[47] D. C. O'Neil,[5] V. Oguri,[3] N. Oliveira,[3] B. Olivier,[16] N. Oshima,[47] G. J. Otero y Garzón,[48] P. Padley,[73] K. Papageorgiou,[48] N. Parashar,[56] J. Park,[29] S. K. Park,[29] J. Parsons,[65] R. Partridge,[71] N. Parua,[67] A. Patwa,[68] P. M. Perea,[45] E. Perez,[17] O. Peters,[31] P. Pétroff,[15] M. Petteni,[40] L. Phaf,[31] R. Piegaia,[1] P. L. M. Podesta-Lerma,[30] V. M. Podstavkov,[47] Y. Pogorelov,[52] B. G. Pope,[61] E. Popkov,[58] W. L. Prado da Silva,[3] H. B. Prosper,[46] S. Protopopescu,[68] M. B. Przybycien,[50,†] J. Qian,[60] A. Quadt,[21] B. Quinn,[62] K. J. Rani,[27] P. A. Rapidis,[47] P. N. Ratoff,[39] N. W. Reay,[55] J.-F. Renardy,[17] S. Reucroft,[59] J. Rha,[45] M. Ridel,[15] M. Rijssenbeek,[67] I. Ripp-Baudot,[18] F. Rizatdinova,[55] C. Royon,[17] P. Rubinov,[47] R. Ruchti,[52] B. M. Sabirov,[33] G. Sajot,[13] A. Sánchez-Hernández,[30] M. P. Sanders,[41] A. Santoro,[3] G. Savage,[47] L. Sawyer,[56] T. Scanlon,[40] R. D. Schamberger,[67] H. Schellman,[50] P. Schieferdecker,[24] C. Schmitt,[25] A. A. Schukin,[36] A. Schwartzman,[64] R. Schwienhorst,[61] S. Sengupta,[46] H. Severini,[70] E. Shabalina,[48] V. Shary,[17] W. D. Shephard,[52] D. Shpakov,[59] R. A. Sidwell,[55] V. Simak,[9] V. Sirotenko,[47] D. Skow,[47] P. Skubic,[70] P. Slattery,[66] R. P. Smith,[47] K. Smolek,[9] G. R. Snow,[63] J. Snow,[69] S. Snyder,[68] S. Söldner-Rembold,[41] X. Song,[49] Y. Song,[72] L. Sonnenschein,[58] A. Sopczak,[39] V. Sorín,[1] M. Sosebee,[72] K. Soustruznik,[8] M. Souza,[2] B. Spurlock,[72] N. R. Stanton,[55] J. Stark,[13] J. Steele,[56] G. Steinbrück,[65] K. Stevenson,[51] V. Stolin,[34] A. Stone,[48] D. A. Stoyanova,[36] J. Strandberg,[38] M. A. Strang,[72] M. Strauss,[70] R. Ströhmer,[24] M. Strovink,[43] L. Stutte,[47] S. Sumowidagdo,[46] A. Sznajder,[3] M. Talby,[14] P. Tamburello,[42] W. Taylor,[67] P. Telford,[41] J. Temple,[42] S. Tentindo-Repond,[46] E. Thomas,[14] B. Thooris,[17] M. Tomoto,[47] T. Toole,[57] J. Torborg,[52] S. Towers,[67] T. Trefzger,[23] S. Trincaz-Duvoid,[16] T. G. Trippe,[43] B. Tuchming,[17] C. Tully,[64] A. S. Turcot,[68] P. M. Tuts,[65] L. Uvarov,[37] S. Uvarov,[37] S. Uzunyan,[49] B. Vachon,[47] R. Van Kooten,[51] W. M. van Leeuwen,[31] N. Varelas,[48] E. W. Varnes,[42] I. A. Vasilyev,[36] M. Vaupel,[25] P. Verdier,[15] L. S. Vertogradov,[33] M. Verzocchi,[57] F. Villeneuve-Seguier,[40] J.-R. Vlimant,[16] E. Von Toerne,[55] M. Vreeswijk,[31] T. Vu Anh,[15] H. D. Wahl,[46] R. Walker,[40] N. Wallace,[42] Z.-M. Wang,[67] J. Warchol,[52] M. Warsinsky,[21] G. Watts,[75] M. Wayne,[52] M. Weber,[47] H. Weerts,[61] M. Wegner,[20] N. Wermes,[21] A. White,[72] V. White,[47] D. Whiteson,[43] D. Wicke,[47] D. A. Wijngaarden,[32] G. W. Wilson,[54] S. J. Wimpenny,[45] J. Wittlin,[58] T. Wlodek,[72] M. Wobisch,[47] J. Womersley,[47] D. R. Wood,[59] Z. Wu,[6] T. R. Wyatt,[41] Q. Xu,[60] N. Xuan,[52] R. Yamada,[47] M. Yan,[57] T. Yasuda,[47] Y. A. Yatsunenko,[33] Y. Yen,[25] K. Yip,[68] S. W. Youn,[50] J. Yu,[72] A. Yurkewicz,[61] A. Zabi,[15] A. Zatserklyaniy,[49] M. Zdrazil,[67] C. Zeitnitz,[23] B. Zhang,[6] D. Zhang,[47] X. Zhang,[70] T. Zhao,[75] Z. Zhao,[60] H. Zheng,[52] B. Zhou,[60] Z. Zhou,[53] J. Zhu,[57] M. Zielinski,[66] D. Zieminska,[51] A. Zieminski,[51] R. Zitoun,[67] V. Zutshi,[49] E. G. Zverev,[35] and A. Zylberstejn[17]

(D0 Collaboration)

[1]*Universidad de Buenos Aires, Buenos Aires, Argentina*
[2]*LAFEX, Centro Brasileiro de Pesquisas Físicas, Rio de Janeiro, Brazil*
[3]*Universidade do Estado do Rio de Janeiro, Rio de Janeiro, Brazil*
[4]*Instituto de Física Teórica, Universidade Estadual Paulista, São Paulo, Brazil*
[5]*University of Alberta and Simon Fraser University, Canada*
[6]*Institute of High Energy Physics, Beijing, People's Republic of China*
[7]*Universidad de los Andes, Bogotá, Colombia*
[8]*Charles University, Center for Particle Physics, Prague, Czech Republic*
[9]*Czech Technical University, Prague, Czech Republic*
[10]*Institute of Physics, Academy of Sciences, Center for Particle Physics, Prague, Czech Republic*
[11]*Universidad San Francisco de Quito, Quito, Ecuador*
[12]*Laboratoire de Physique Corpusculaire, IN2P3-CNRS, Université Blaise Pascal, Clermont-Ferrand, France*
[13]*Laboratoire de Physique Subatomique et de Cosmologie, IN2P3-CNRS, Universite de Grenoble 1, Grenoble, France*
[14]*CPPM, IN2P3-CNRS, Université de la Méditerranée, Marseille, France*
[15]*Laboratoire de l'Accélérateur Linéaire, IN2P3-CNRS, Orsay, France*
[16]*LPNHE, Universités Paris VI and VII, IN2P3-CNRS, Paris, France*
[17]*DAPNIA/Service de Physique des Particules, CEA, Saclay, France*
[18]*IReS, IN2P3-CNRS, University Louis Pasteur Strasbourg, and University de Haute Alsace, France*
[19]*Institut de Physique Nucléaire de Lyon, IN2P3-CNRS, Université Claude Bernard, Villeurbanne, France*
[20]*RWTH Aachen, III. Physikalisches Institut A, Aachen, Germany*
[21]*Universität Bonn, Physikalisches Institut, Bonn, Germany*
[22]*Universität Freiburg, Physikalisches Institut, Freiburg, Germany*
[23]*Universität Mainz, Institut für Physik, Mainz, Germany*

[24]Ludwig-Maximilians-Universität München, München, Germany
[25]Fachbereich Physik, University of Wuppertal, Wuppertal, Germany
[26]Punjab University, Chandigarh, India
[27]Tata Institute of Fundamental Research, Mumbai, India
[28]University College Dublin, Dublin, Ireland
[29]Korea Detector Laboratory, Korea University, Seoul, Korea
[30]CINVESTAV, Mexico City, Mexico
[31]FOM-Institute NIKHEF and University of Amsterdam/NIKHEF, Amsterdam, The Netherlands
[32]University of Nijmegen/NIKHEF, Nijmegen, The Netherlands
[33]Joint Institute for Nuclear Research, Dubna, Russia
[34]Institute for Theoretical and Experimental Physics, Moscow, Russia
[35]Moscow State University, Moscow, Russia
[36]Institute for High Energy Physics, Protvino, Russia
[37]Petersburg Nuclear Physics Institute, St. Petersburg, Russia
[38]Lund University, Royal Institute of Technology, Stockholm University, and Uppsala University, Sweden
[39]Lancaster University, Lancaster, United Kingdom
[40]Imperial College, London, United Kingdom
[41]University of Manchester, Manchester, United Kingdom
[42]University of Arizona, Tucson, Arizona 85721, USA
[43]Lawrence Berkeley National Laboratory and University of California, Berkeley, California 94720, USA
[44]California State University, Fresno, California 93740, USA
[45]University of California, Riverside, California 92521, USA
[46]Florida State University, Tallahassee, Florida 32306, USA
[47]Fermi National Accelerator Laboratory, Batavia, Illinois 60510, USA
[48]University of Illinois at Chicago, Chicago, Illinois 60607, USA
[49]Northern Illinois University, DeKalb, Illinois 60115, USA
[50]Northwestern University, Evanston, Illinois 60208, USA
[51]Indiana University, Bloomington, Indiana 47405, USA
[52]University of Notre Dame, Notre Dame, Indiana 46556, USA
[53]Iowa State University, Ames, Iowa 50011, USA
[54]University of Kansas, Lawrence, Kansas 66045, USA
[55]Kansas State University, Manhattan, Kansas 66506, USA
[56]Louisiana Tech University, Ruston, Louisiana 71272, USA
[57]University of Maryland, College Park, Maryland 20742, USA
[58]Boston University, Boston, Massachusetts 02215, USA
[59]Northeastern University, Boston, Massachusetts 02115, USA
[60]University of Michigan, Ann Arbor, Michigan 48109, USA
[61]Michigan State University, East Lansing, Michigan 48824, USA
[62]University of Mississippi, University, Mississippi 38677, USA
[63]University of Nebraska, Lincoln, Nebraska 68588, USA
[64]Princeton University, Princeton, New Jersey 08544, USA
[65]Columbia University, New York, New York 10027, USA
[66]University of Rochester, Rochester, New York 14627, USA
[67]State University of New York, Stony Brook, New York 11794, USA
[68]Brookhaven National Laboratory, Upton, New York 11973, USA
[69]Langston University, Langston, Oklahoma 73050, USA
[70]University of Oklahoma, Norman, Oklahoma 73019, USA
[71]Brown University, Providence, Rhode Island 02912, USA
[72]University of Texas, Arlington, Texas 76019, USA
[73]Rice University, Houston, Texas 77005, USA
[74]University of Virginia, Charlottesville, Virginia 22901, USA
[75]University of Washington, Seattle, Washington 98195, USA

(Received 16 September 2004; published 7 June 2005)

Correlations in the azimuthal angle between the two largest transverse momentum jets have been measured using the D0 detector in $p\bar{p}$ collisions at a center-of-mass energy $\sqrt{s} = 1.96$ TeV. The analysis is based on an inclusive dijet event sample in the central rapidity region corresponding to an integrated luminosity of 150 pb^{-1}. Azimuthal correlations are stronger at larger transverse momenta. These are well described in perturbative QCD at next-to-leading order in the strong coupling constant, except at large azimuthal differences where contributions with low transverse momentum are significant.

DOI: 10.1103/PhysRevLett.94.221801 PACS numbers: 13.87.Ce, 12.38.Qk

Radiation of multiple quarks and gluons is one of the more complex aspects of perturbative quantum chromodynamics (PQCD), and it is being actively studied for the physics programs at the Fermilab Tevatron Collider and the CERN LHC [1]. The proper description of radiative processes is crucial for a wide range of precision measurements as well as for searches for new physical phenomena where the influence of QCD radiation is unavoidable. In this Letter we study radiative processes by examining their impact on angular distributions. We investigate the azimuthal angle between the two jets with highest transverse momenta with respect to the beam axis (p_T), $\Delta\phi_{\text{dijet}}$. Dijet production in hadron-hadron collisions, in the absence of radiative effects, results in two jets with equal transverse momenta and correlated azimuthal angles $\Delta\phi_{\text{dijet}} = \pi$. Additional radiation with low p_T causes small azimuthal decorrelations, whereas $\Delta\phi_{\text{dijet}}$ significantly lower than π is evidence of additional hard radiation with high p_T. Exclusive three-jet production populates $2\pi/3 < \Delta\phi_{\text{dijet}} < \pi$, while smaller values of $\Delta\phi_{\text{dijet}}$ require additional radiation such as a fourth jet in an event. Distributions in $\Delta\phi_{\text{dijet}}$ provide an ideal testing ground for higher-order PQCD predictions without requiring the reconstruction of additional jets and offer a way to examine the transition between soft and hard QCD processes based on a single observable.

A new measurement of azimuthal decorrelations between jets produced at high p_T in $p\bar{p}$ collisions is presented in this Letter. This is the first measurement of the differential $\Delta\phi_{\text{dijet}}$ distribution in dijet production at a hadron collider. Jets are defined using a cone algorithm [2] with radius $\mathcal{R}_{\text{cone}} = 0.7$. The same jet algorithm is used for partons in the PQCD calculations, final-state particles in the Monte Carlo event generators, and reconstructed energy depositions in the experiment. The observable, $(1/\sigma_{\text{dijet}})(d\sigma_{\text{dijet}}/d\Delta\phi_{\text{dijet}})$, is defined as the differential dijet cross section in $\Delta\phi_{\text{dijet}}$ normalized by the dijet cross section integrated over $\Delta\phi_{\text{dijet}}$ in the same phase space. (Theoretical and experimental uncertainties are reduced in this construction.) Calculations of three-jet observables at next-to-leading order (NLO) in the strong coupling constant α_s have recently become available [3,4].

Data were obtained with the D0 detector [5] in Run II of the Fermilab Tevatron Collider using $p\bar{p}$ collisions at $\sqrt{s} = 1.96$ TeV. The primary tool for jet detection was a compensating, finely segmented, liquid-argon and uranium calorimeter that provided nearly full solid-angle coverage. Calorimeter cells were grouped into projective towers focused on the nominal interaction point for trigger and reconstruction purposes. Events were acquired using multiple-stage inclusive-jet triggers. Four analysis regions were defined based on the jet with largest p_T in an event ($p_T^{\max}$) with the requirement that the trigger efficiency be at least 99%. The accumulated integrated luminosities for events with $p_T^{\max} > 75$, 100, 130, and 180 GeV were 1.1, 21, 90, and 150 pb^{-1}($\pm 6.5\%$), respectively. The second leading p_T jet in each event was required to have $p_T > 40$ GeV and both jets were required to have central rapidities with $|y_{\text{jet}}| < 0.5$ where $y_{\text{jet}} = \frac{1}{2}\ln[(E + p_z)/(E - p_z)]$ and E and p_z are the energy and the longitudinal momentum of the jet.

The position of the $p\bar{p}$ interaction was reconstructed using a tracking system consisting of silicon microstrip detectors and scintillating fibers located within a 2 T solenoidal magnet. The vertex coordinate along the beam axis was required to be within 50 cm of the detector center, which preserved the projective nature of the calorimeter towers. The systematic uncertainty associated with the vertex selection efficiency is less than 3% for $\Delta\phi_{\text{dijet}} > 2\pi/3$ and $\approx 8\%$ for $\Delta\phi_{\text{dijet}} \approx \pi/2$. The missing transverse energy was calculated from the vector sum of the individual transverse energies in calorimeter cells. Background from cosmic rays and incorrectly vertexed events was eliminated by requiring this missing transverse energy to be below $0.7p_T^{\max}$. Background introduced by electrons, photons, and detector noise that mimicked jets was eliminated based on characteristics of shower development expected for genuine jets. The overall efficiency for $\Delta\phi_{\text{dijet}} < 5\pi/6$ is 82%–84%, depending on the $p_T^{\max}$ region. For $\Delta\phi_{\text{dijet}} \to \pi$ it drops to 76%–81%.

The p_T of each jet was corrected for calorimeter showering effects, overlaps due to multiple interactions and event pileup, calorimeter noise effects, and the energy response of the calorimeter. The calorimeter response was measured from the p_T imbalance in photon + jet events. The relative uncertainty on the jet energy calibration is $\approx 7\%$ for jets with $20 < p_T < 250$ GeV. The sensitivity of the measurement to this calibration was reduced by normalizing the $\Delta\phi_{\text{dijet}}$ distribution to the integrated dijet cross section. Nevertheless, this provides the largest contribution to the systematic uncertainty ($< 7\%$ for $\Delta\phi_{\text{dijet}} > 5\pi/6$ but up to 23% for $\Delta\phi_{\text{dijet}} < 2\pi/3$).

The correction for migrations between bins due to finite energy and position resolution was determined from events generated with the HERWIG [6] and PYTHIA [7] programs. The generated jets were smeared according to detector resolutions [8]. The angular jet resolution was determined from a full simulation of the D0 detector response. It was found to be better than 20 mrad for jets with energies above 80 GeV. The jet p_T resolution was measured from the p_T imbalance in dijet events. It decreases from 18% at $p_T = 40$ GeV to 9% for $p_T = 200$ GeV. Finite jet p_T resolution can lead to ambiguities in the selection of the two leading p_T jets. This effect is large at small $\Delta\phi_{\text{dijet}}$ where contri-

butions from higher jet multiplicities dominate. The generated events were reweighted to describe the observed $\Delta\phi_{\text{dijet}}$ distribution. This provided a good description of the observed p_T spectra of the four leading p_T jets. The correction for migrations is typically less than 8% for $\Delta\phi_{\text{dijet}} > 2\pi/3$ and $\approx 40\%$ for $\Delta\phi_{\text{dijet}} \approx \pi/2$ with a model dependence of less than 2%. Only for $p_T^{\max} < 130$ GeV and at $\Delta\phi_{\text{dijet}} \approx \pi/2$ is the model dependence as large as $\approx 14\%$. The model dependence was taken into account in the evaluation of the overall systematic uncertainty.

The corrected data are presented in Fig. 1 as a function of $\Delta\phi_{\text{dijet}}$ in four ranges of $p_T^{\max}$. The inner error bars represent the statistical uncertainties, and the outer error bars correspond to the quadratic sum of the statistical and systematic uncertainties. The systematic uncertainties include contributions from the sources described above: event selection efficiency, jet energy calibration, and the model dependence in the correction for migrations. The spectra are strongly peaked at $\Delta\phi_{\text{dijet}} \approx \pi$; the peaks are narrower at larger values of $p_T^{\max}$. Overlaid on the data points in Fig. 1 are the results of PQCD calculations obtained using the parton-level event generator NLOJET++ [4] and CTEQ6.1M [9] parton distribution functions (PDFs) with $\alpha_s(M_Z) = 0.118$. The leading order (LO) PQCD prediction for the observable was calculated from the ratio of the predictions for $2 \to 3$ processes ($d\sigma_{\text{dijet}}/d\Delta\phi_{\text{dijet}}$) and $2 \to 2$ processes (σ_{dijet}), both at LO. The NLO prediction of the observable was analogously obtained from the NLO results of the individual pieces,

$$\frac{1}{\sigma_{\text{dijet}}} \left| \frac{d\sigma_{\text{dijet}}}{d\Delta\phi_{\text{dijet}}} \right|_{\text{(N)LO}}.$$

The renormalization and factorization scales are chosen to be $\mu_r = \mu_f = 0.5 p_T^{\max}$. The ratio is insensitive to hadronization corrections and the underlying event [10].

As shown in Fig. 2, data and NLO agree within 5%–20%. The theoretical uncertainty due to the PDFs [9] is estimated to be below 20%. Also shown is the effect of renormalization and factorization scale variation ($0.25 p_T^{\max} < \mu_{r,f} < p_T^{\max}$). The large scale dependence for $\Delta\phi_{\text{dijet}} < 2\pi/3$ occurs because the NLO calculation receives contributions only from tree-level four-parton final states in this regime. Results from PQCD at large

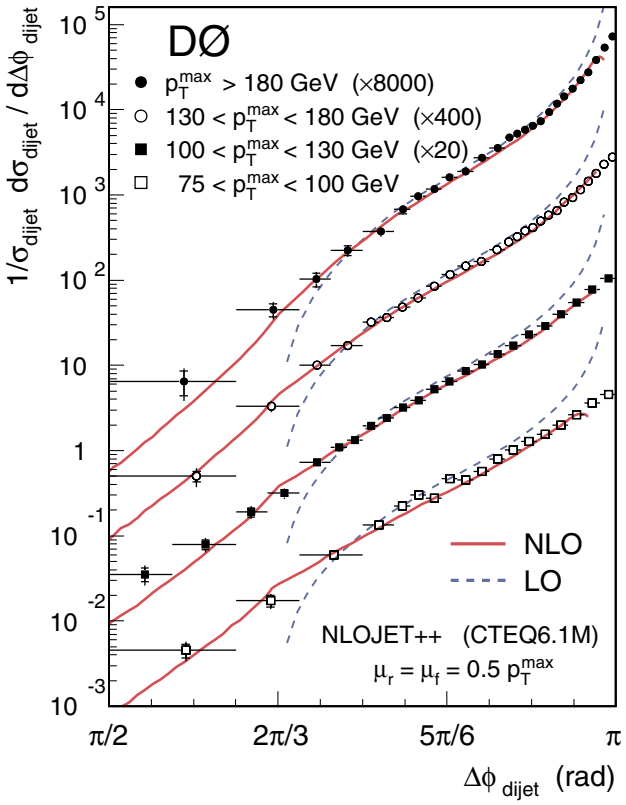

FIG. 1 (color online). The $\Delta\phi_{\text{dijet}}$ distributions in four regions of $p_T^{\max}$. Data and predictions with $p_T^{\max} > 100$ GeV are scaled by successive factors of 20 for purposes of presentation. The solid (dashed) lines show the NLO (LO) PQCD predictions.

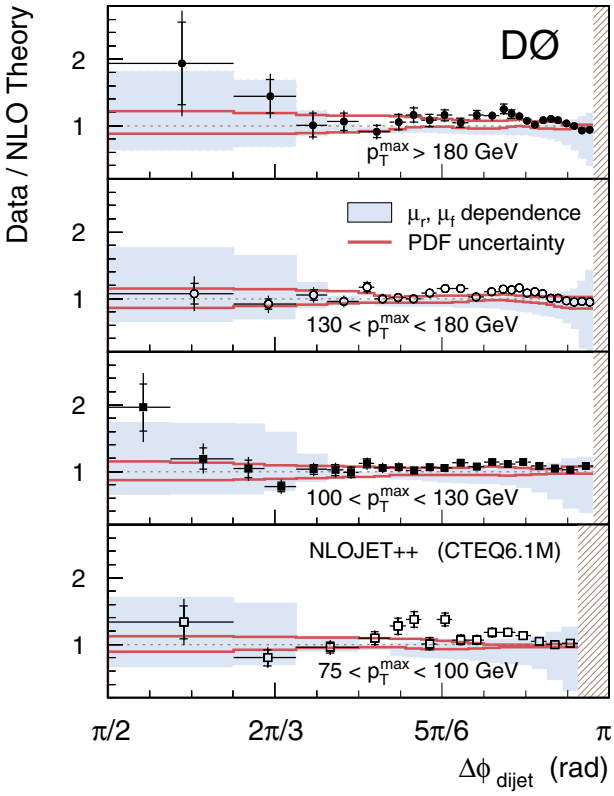

FIG. 2 (color online). Ratios of data to the NLO PQCD calculation for different regions of $p_T^{\max}$. Theoretical uncertainties due to variation of μ_r and μ_f are shown as the shaded regions; the uncertainty due to the PDFs is indicated by the solid lines. The points at large $\Delta\phi_{\text{dijet}}$ are excluded because the calculation is not stable near the divergence at π.

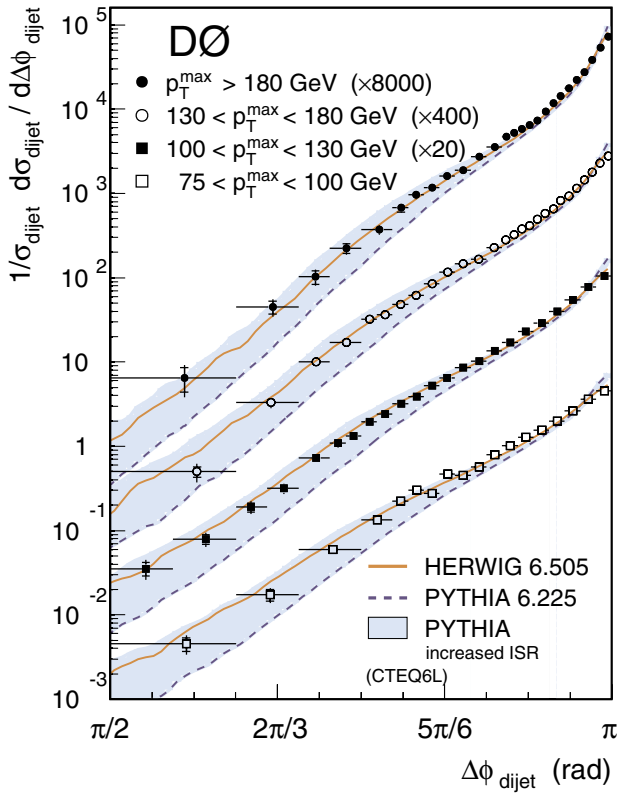

FIG. 3 (color online). The $\Delta\phi_{\text{dijet}}$ distributions in different p_T^{max} ranges. Results from HERWIG and PYTHIA are overlaid on the data. Data and predictions with $p_T^{\text{max}} > 100$ GeV are scaled by successive factors of 20 for purposes of presentation.

$\Delta\phi_{\text{dijet}}$ in Figs. 1 and 2 were excluded because fixed-order perturbation theory fails to describe the data in the region $\Delta\phi_{\text{dijet}} \approx \pi$ where soft processes dominate. Overall, NLO PQCD provides a good description of the data although differences in shape can be discerned for $\Delta\phi_{\text{dijet}} \gtrsim 5\pi/6$. In this region, the observable probes the transition between two- and three-jet configurations. The cone algorithm is sensitive to the fine details of the event topology in this transition region. These details may not be adequately described by low-order PQCD, and higher-order calculations may be required.

Monte Carlo event generators, such as HERWIG and PYTHIA, use $2 \rightarrow 2$ LO PQCD matrix elements with phenomenological parton-shower models to simulate higher-order QCD effects. Results from HERWIG (version 6.505) and PYTHIA (version 6.225), both using default parameters and the CTEQ6L [9] PDFs, are compared to the data in Fig. 3. HERWIG describes the data well over the entire $\Delta\phi_{\text{dijet}}$ range including $\Delta\phi_{\text{dijet}} \approx \pi$. PYTHIA with default parameters describes the data poorly—the distribution is too narrowly peaked at $\Delta\phi_{\text{dijet}} \approx \pi$ and lies significantly below the data over most of the $\Delta\phi_{\text{dijet}}$ range. The maximum p_T^2 in the initial-state parton shower is directly related to the maximum virtuality that can be adjusted in PYTHIA. The shaded bands in Fig. 3 indicate the range of variation when the maximum allowed virtuality is smoothly increased from the current default by a factor of 4 [11]. These variations result in significant changes in the low $\Delta\phi_{\text{dijet}}$ region clearly demonstrating the sensitivity of this measurement. Consequently, global efforts to tune Monte Carlo event generators should benefit from including our data.

To summarize, we have measured the dijet azimuthal decorrelation in different ranges of leading jet p_T and observe an increased decorrelation towards smaller p_T. NLO PQCD describes the data except for very large $\Delta\phi_{\text{dijet}}$ where the calculation is not predictive.

We thank W. Giele, Z. Nagy, M. H. Seymour, and T. Sjöstrand for many helpful discussions. We thank the staffs at Fermilab and collaborating institutions, and acknowledge support from the Department of Energy and National Science Foundation (USA), Commissariat à l'Energie Atomique and CNRS/Institut National de Physique Nucléaire et de Physique des Particules (France), Ministry of Education and Science, Agency for Atomic Energy and RF President Grants Program (Russia), CAPES, CNPq, FAPERJ, FAPESP, and FUNDUNESP (Brazil), Departments of Atomic Energy and Science and Technology (India), Colciencias (Colombia), CONACyT (Mexico), KRF (Korea), CONICET and UBACyT (Argentina), The Foundation for Fundamental Research on Matter (The Netherlands), PPARC (United Kingdom), Ministry of Education (Czech Republic), Natural Sciences and Engineering Research Council and WestGrid Project (Canada), BMBF and DFG (Germany), A. P. Sloan Foundation, Civilian Research and Development Foundation, Research Corporation, Texas Advanced Research Program, and the Alexander von Humboldt Foundation.

*Visitor from University of Zurich, Zurich, Switzerland.
†Visitor from Institute of Nuclear Physics, Krakow, Poland.

[1] M. Dobbs *et al.*, hep-ph/0403100.
[2] We are using the iterative, seed-based cone algorithm including midpoints, as described on p. 47, Sect. 3.5 in G. C. Blazey *et al.*, in *Proceedings of the Workshop: QCD and Weak Boson Physics in Run II*, edited by U. Baur, R. K. Ellis, and D. Zeppenfeld (Fermilab, Batavia, IL, 2000).
[3] W. B. Kilgore and W. T. Giele, in *Proceedings of the 35th Rencontres De Moriond, Les Arcs, France, 2000*, edited by J. Tran Thanh Van (EDP Sciences, Les Ulis, France, 2001).
[4] Z. Nagy, Phys. Rev. Lett. **88**, 122003 (2002); Z. Nagy, Phys. Rev. D **68**, 094002 (2003).
[5] D0 Collaboration, V. Abazov *et al.*, Nucl. Instrum. Methods Phys. Res., Sect. A (to be published); T. LeCompte and H. T. Diehl, Annu. Rev. Nucl. Part. Sci.

50, 71 (2000); D0 Collaboration, S. Abachi *et al.*, Nucl. Instrum. Methods Phys. Res., Sect. A **338**, 185 (1994).

[6] G. Marchesini *et al.*, Comput. Phys. Commun. **67**, 465 (1992); G. Corcella *et al.*, J. High Energy Phys. 01 (2001) 010.

[7] T. Sjöstrand *et al.*, Comput. Phys. Commun. **135**, 238 (2001).

[8] A. Kupčo, Ph.D. thesis, Charles University, Prague, Czech Republic, 2003 (unpublished).

[9] J. Pumplin *et al.*, J. High Energy Phys. 07 (2002) 12; D. Stump *et al.*, J. High Energy Phys. 10 (2003) 046.

[10] M. Wobisch, hep-ex/0411025 (to be published).

[11] The PYTHIA parameter PARP(67) was increased from the current default of 1.0 to 4.0 which was the default before version 6.138. A variation in this range is generally considered to be reasonable [12]. The maximum virtuality in the initial-state parton shower is defined by the product of PARP(67) and the square of the hard-scattering scale.

[12] T. Sjöstrand, L. Lönnblad, and S. Mrenna, PYTHIA 6.2 Physics and Manual, LU-TP 01-21 (2001), hep-ph/0108264.

Measurement of the Inclusive Jet Cross Section in $p\bar{p}$ Collisions at $\sqrt{s} = 1.96$ TeV

V. M. Abazov,[36] B. Abbott,[75] M. Abolins,[65] B. S. Acharya,[29] M. Adams,[51] T. Adams,[49] E. Aguilo,[6] S. H. Ahn,[31] M. Ahsan,[59] G. D. Alexeev,[36] G. Alkhazov,[40] A. Alton,[64,*] G. Alverson,[63] G. A. Alves,[2] M. Anastasoaie,[35] L. S. Ancu,[35] T. Andeen,[53] S. Anderson,[45] B. Andrieu,[17] M. S. Anzelc,[53] Y. Arnoud,[14] M. Arov,[60] M. Arthaud,[18] A. Askew,[49] B. Åsman,[41] A. C. S. Assis Jesus,[3] O. Atramentov,[49] C. Autermann,[21] C. Avila,[8] C. Ay,[24] F. Badaud,[13] A. Baden,[61] L. Bagby,[50] B. Baldin,[50] D. V. Bandurin,[59] P. Banerjee,[29] S. Banerjee,[29] E. Barberis,[63] A.-F. Barfuss,[15] P. Bargassa,[80] P. Baringer,[58] J. Barreto,[2] J. F. Bartlett,[50] U. Bassler,[18] D. Bauer,[43] S. Beale,[6] A. Bean,[58] M. Begalli,[3] M. Begel,[73] C. Belanger-Champagne,[41] L. Bellantoni,[50] A. Bellavance,[50] J. A. Benitez,[65] S. B. Beri,[27] G. Bernardi,[17] R. Bernhard,[23] I. Bertram,[42] M. Besançon,[18] R. Beuselinck,[43] V. A. Bezzubov,[39] P. C. Bhat,[50] V. Bhatnagar,[27] C. Biscarat,[20] G. Blazey,[52] F. Blekman,[43] S. Blessing,[49] D. Bloch,[19] K. Bloom,[67] A. Boehnlein,[50] D. Boline,[62] T. A. Bolton,[59] G. Borissov,[42] T. Bose,[77] A. Brandt,[78] R. Brock,[65] G. Brooijmans,[70] A. Bross,[50] D. Brown,[81] N. J. Buchanan,[49] D. Buchholz,[53] M. Buehler,[81] V. Buescher,[22] V. Bunichev,[38] S. Burdin,[42,†] S. Burke,[45] T. H. Burnett,[82] C. P. Buszello,[43] J. M. Butler,[62] P. Calfayan,[25] S. Calvet,[16] J. Cammin,[71] W. Carvalho,[3] B. C. K. Casey,[50] H. Castilla-Valdez,[33] S. Chakrabarti,[18] D. Chakraborty,[52] K. Chan,[6] K. M. Chan,[55] A. Chandra,[48] F. Charles,[19,**] E. Cheu,[45] F. Chevallier,[14] D. K. Cho,[62] S. Choi,[32] B. Choudhary,[28] L. Christofek,[77] T. Christoudias,[43] S. Cihangir,[50] D. Claes,[67] Y. Coadou,[6] M. Cooke,[80] W. E. Cooper,[50] M. Corcoran,[80] F. Couderc,[18] M.-C. Cousinou,[15] S. Crépé-Renaudin,[14] D. Cutts,[77] M. Ćwiok,[30] H. da Motta,[2] A. Das,[45] G. Davies,[43] K. De,[78] S. J. de Jong,[35] E. De La Cruz-Burelo,[64] C. De Oliveira Martins,[3] J. D. Degenhardt,[64] F. Déliot,[18] M. Demarteau,[50] R. Demina,[71] D. Denisov,[50] S. P. Denisov,[39] S. Desai,[50] H. T. Diehl,[50] M. Diesburg,[50] A. Dominguez,[67] H. Dong,[72] L. V. Dudko,[38] L. Duflot,[16] S. R. Dugad,[29] D. Duggan,[49] A. Duperrin,[15] J. Dyer,[65] A. Dyshkant,[52] M. Eads,[67] D. Edmunds,[65] J. Ellison,[48] V. D. Elvira,[50] Y. Enari,[77] S. Eno,[61] P. Ermolov,[38] H. Evans,[54] A. Evdokimov,[73] V. N. Evdokimov,[39] A. V. Ferapontov,[59] T. Ferbel,[71] F. Fiedler,[24] F. Filthaut,[35] W. Fisher,[50] H. E. Fisk,[50] M. Ford,[44] M. Fortner,[52] H. Fox,[42] S. Fu,[50] S. Fuess,[50] T. Gadfort,[70] C. F. Galea,[35] E. Gallas,[50] C. Garcia,[71] A. Garcia-Bellido,[82] V. Gavrilov,[37] P. Gay,[13] W. Geist,[19] D. Gelé,[19] C. E. Gerber,[51] Y. Gershtein,[49] D. Gillberg,[6] G. Ginther,[71] N. Gollub,[41] B. Gómez,[8] A. Goussiou,[82] P. D. Grannis,[72] H. Greenlee,[50] Z. D. Greenwood,[60] E. M. Gregores,[4] G. Grenier,[20] Ph. Gris,[13] J.-F. Grivaz,[16] A. Grohsjean,[25] S. Grünendahl,[50] M. W. Grünewald,[30] F. Guo,[72] J. Guo,[72] G. Gutierrez,[50] P. Gutierrez,[75] A. Haas,[70] N. J. Hadley,[61] P. Haefner,[25] S. Hagopian,[49] J. Haley,[68] I. Hall,[65] R. E. Hall,[47] L. Han,[7] K. Harder,[44] A. Harel,[71] R. Harrington,[63] J. M. Hauptman,[57] R. Hauser,[65] J. Hays,[43] T. Hebbeker,[21] D. Hedin,[52] J. G. Hegeman,[34] J. M. Heinmiller,[51] A. P. Heinson,[48] U. Heintz,[62] C. Hensel,[58] K. Herner,[72] G. Hesketh,[63] M. D. Hildreth,[55] R. Hirosky,[81] J. D. Hobbs,[72] B. Hoeneisen,[12] H. Hoeth,[26] M. Hohlfeld,[22] S. J. Hong,[31] S. Hossain,[75] P. Houben,[34] Y. Hu,[72] Z. Hubacek,[10] V. Hynek,[9] I. Iashvili,[69] R. Illingworth,[50] A. S. Ito,[50] S. Jabeen,[62] M. Jaffré,[16] S. Jain,[75] K. Jakobs,[23] C. Jarvis,[61] R. Jesik,[43] K. Johns,[45] C. Johnson,[70] M. Johnson,[50] A. Jonckheere,[50] P. Jonsson,[43] A. Juste,[50] E. Kajfasz,[15] A. M. Kalinin,[36] J. M. Kalk,[60] S. Kappler,[21] D. Karmanov,[38] P. A. Kasper,[50] I. Katsanos,[70] D. Kau,[49] R. Kaur,[27] V. Kaushik,[78] R. Kehoe,[79] S. Kermiche,[15] N. Khalatyan,[50] A. Khanov,[76] A. Kharchilava,[69] Y. M. Kharzheev,[36] D. Khatidze,[70] T. J. Kim,[31] M. H. Kirby,[53] M. Kirsch,[21] B. Klima,[50] J. M. Kohli,[27] J.-P. Konrath,[23] V. M. Korablev,[39] A. V. Kozelov,[39] J. Kraus,[65] D. Krop,[54] T. Kuhl,[24] A. Kumar,[69] A. Kupco,[11] T. Kurča,[20] J. Kvita,[9] F. Lacroix,[13] D. Lam,[55] S. Lammers,[70] G. Landsberg,[77] P. Lebrun,[20] W. M. Lee,[50] A. Leflat,[38] J. Lellouch,[17] J. Leveque,[45] J. Li,[78] L. Li,[48] Q. Z. Li,[50] S. M. Lietti,[5] J. G. R. Lima,[52] D. Lincoln,[50] J. Linnemann,[65] V. V. Lipaev,[39] R. Lipton,[50] Y. Liu,[7] Z. Liu,[6] A. Lobodenko,[40] M. Lokajicek,[11] P. Love,[42] H. J. Lubatti,[82] R. Luna,[3] A. L. Lyon,[50] A. K. A. Maciel,[2] D. Mackin,[80] R. J. Madaras,[46] P. Mättig,[26] C. Magass,[21] A. Magerkurth,[64] P. K. Mal,[55] H. B. Malbouisson,[3] S. Malik,[67] V. L. Malyshev,[36] H. S. Mao,[50] Y. Maravin,[59] B. Martin,[14] R. McCarthy,[72] A. Melnitchouk,[66] L. Mendoza,[8] P. G. Mercadante,[5] M. Merkin,[38] K. W. Merritt,[50] A. Meyer,[21] J. Meyer,[22,§] T. Millet,[20] J. Mitrevski,[70] J. Molina,[3] R. K. Mommsen,[44] N. K. Mondal,[29] R. W. Moore,[6] T. Moulik,[58] G. S. Muanza,[20] M. Mulders,[50] M. Mulhearn,[70] O. Mundal,[22] L. Mundim,[3] E. Nagy,[15] M. Naimuddin,[50] M. Narain,[77] N. A. Naumann,[35] H. A. Neal,[64] J. P. Negret,[8] P. Neustroev,[40] H. Nilsen,[23] H. Nogima,[3] S. F. Novaes,[5] T. Nunnemann,[25] V. O'Dell,[50] D. C. O'Neil,[6] G. Obrant,[40] C. Ochando,[16] D. Onoprienko,[59] N. Oshima,[50] N. Osman,[43] J. Osta,[55] R. Otec,[10] G. J. Otero y Garzón,[50] M. Owen,[44] P. Padley,[80] M. Pangilinan,[77] N. Parashar,[56] S.-J. Park,[71] S. K. Park,[31] J. Parsons,[70] R. Partridge,[77] N. Parua,[54] A. Patwa,[73] G. Pawloski,[80] B. Penning,[23] M. Perfilov,[38] K. Peters,[44] Y. Peters,[26] P. Pétroff,[16] M. Petteni,[43] R. Piegaia,[1] J. Piper,[65] M.-A. Pleier,[22] P. L. M. Podesta-Lerma,[33,‡] V. M. Podstavkov,[50] Y. Pogorelov,[55] M.-E. Pol,[2] P. Polozov,[37] B. G. Pope,[65] A. V. Popov,[39] C. Potter,[6] W. L. Prado da Silva,[3] H. B. Prosper,[49] S. Protopopescu,[73] J. Qian,[64] A. Quadt,[22,§] B. Quinn,[66] A. Rakitine,[42]

M. S. Rangel,[2] K. Ranjan,[28] P. N. Ratoff,[42] P. Renkel,[79] S. Reucroft,[63] P. Rich,[44] J. Rieger,[54] M. Rijssenbeek,[72] I. Ripp-Baudot,[19] F. Rizatdinova,[76] S. Robinson,[43] R. F. Rodrigues,[3] M. Rominsky,[75] C. Royon,[18] P. Rubinov,[50] R. Ruchti,[55] G. Safronov,[37] G. Sajot,[14] A. Sánchez-Hernández,[33] M. P. Sanders,[17] A. Santoro,[3] G. Savage,[50] L. Sawyer,[60] T. Scanlon,[43] D. Schaile,[25] R. D. Schamberger,[72] Y. Scheglov,[40] H. Schellman,[53] T. Schliephake,[26] C. Schwanenberger,[44] A. Schwartzman,[68] R. Schwienhorst,[65] J. Sekaric,[49] H. Severini,[75] E. Shabalina,[51] M. Shamim,[59] V. Shary,[18] A. A. Shchukin,[39] R. K. Shivpuri,[28] V. Siccardi,[19] V. Simak,[10] V. Sirotenko,[50] P. Skubic,[75] P. Slattery,[71] D. Smirnov,[55] G. R. Snow,[67] J. Snow,[74] S. Snyder,[73] S. Söldner-Rembold,[44] L. Sonnenschein,[17] A. Sopczak,[42] M. Sosebee,[78] K. Soustruznik,[9] B. Spurlock,[78] J. Stark,[14] J. Steele,[60] V. Stolin,[37] D. A. Stoyanova,[39] J. Strandberg,[64] S. Strandberg,[41] M. A. Strang,[69] E. Strauss,[72] M. Strauss,[75] R. Ströhmer,[25] D. Strom,[53] L. Stutte,[50] S. Sumowidagdo,[49] P. Svoisky,[55] A. Sznajder,[3] P. Tamburello,[45] A. Tanasijczuk,[1] W. Taylor,[6] J. Temple,[45] B. Tiller,[25] F. Tissandier,[13] M. Titov,[18] V. V. Tokmenin,[36] T. Toole,[61] I. Torchiani,[23] T. Trefzger,[24] D. Tsybychev,[72] B. Tuchming,[18] C. Tully,[68] P. M. Tuts,[70] R. Unalan,[65] L. Uvarov,[40] S. Uvarov,[40] S. Uzunyan,[52] B. Vachon,[6] P. J. van den Berg,[34] R. Van Kooten,[54] W. M. van Leeuwen,[34] N. Varelas,[51] E. W. Varnes,[45] I. A. Vasilyev,[39] M. Vaupel,[26] P. Verdier,[20] L. S. Vertogradov,[36] M. Verzocchi,[50] F. Villeneuve-Seguier,[43] P. Vint,[43] P. Vokac,[10] E. Von Toerne,[59] M. Voutilainen,[68,‖] R. Wagner,[68] H. D. Wahl,[49] L. Wang,[61] M. H. L. S. Wang,[50] J. Warchol,[55] G. Watts,[82] M. Wayne,[55] G. Weber,[24] M. Weber,[50] L. Welty-Rieger,[54] A. Wenger,[23,¶] N. Wermes,[22] M. Wetstein,[61] A. White,[78] D. Wicke,[26] G. W. Wilson,[58] S. J. Wimpenny,[48] M. Wobisch,[60] D. R. Wood,[63] T. R. Wyatt,[44] Y. Xie,[77] S. Yacoob,[53] R. Yamada,[50] M. Yan,[61] T. Yasuda,[50] Y. A. Yatsunenko,[36] K. Yip,[73] H. D. Yoo,[77] S. W. Youn,[53] J. Yu,[78] A. Zatserklyaniy,[52] C. Zeitnitz,[26] T. Zhao,[82] B. Zhou,[64] J. Zhu,[72] M. Zielinski,[71] D. Zieminska,[54] A. Zieminski,[54,**] L. Zivkovic,[70] V. Zutshi,[52] and E. G. Zverev[38]

(D0 Collaboration)

[1]*Universidad de Buenos Aires, Buenos Aires, Argentina*
[2]*LAFEX, Centro Brasileiro de Pesquisas Físicas, Rio de Janeiro, Brazil*
[3]*Universidade do Estado do Rio de Janeiro, Rio de Janeiro, Brazil*
[4]*Universidade Federal do ABC, Santo André, Brazil*
[5]*Instituto de Física Teórica, Universidade Estadual Paulista, São Paulo, Brazil*
[6]*University of Alberta, Edmonton, Alberta, Canada,*
Simon Fraser University, Burnaby, British Columbia, Canada,
York University, Toronto, Ontario, Canada,
and McGill University, Montreal, Quebec, Canada
[7]*University of Science and Technology of China, Hefei, People's Republic of China*
[8]*Universidad de los Andes, Bogotá, Colombia*
[9]*Center for Particle Physics, Charles University, Prague, Czech Republic*
[10]*Czech Technical University, Prague, Czech Republic*
[11]*Center for Particle Physics, Institute of Physics, Academy of Sciences of the Czech Republic, Prague, Czech Republic*
[12]*Universidad San Francisco de Quito, Quito, Ecuador*
[13]*LPC, Université Blaise Pascal, CNRS/IN2P3, Clermont, France*
[14]*LPSC, Université Joseph Fourier Grenoble 1, CNRS/IN2P3, Institut National Polytechnique de Grenoble, France*
[15]*CPPM, IN2P3/CNRS, Université de la Méditerranée, Marseille, France*
[16]*LAL, Université Paris-Sud, IN2P3/CNRS, Orsay, France*
[17]*LPNHE, IN2P3/CNRS, Universités Paris VI and VII, Paris, France*
[18]*DAPNIA/Service de Physique des Particules, CEA, Saclay, France*
[19]*IPHC, Université Louis Pasteur et Université de Haute Alsace, CNRS/IN2P3, Strasbourg, France*
[20]*IPNL, Université Lyon 1, CNRS/IN2P3, Villeurbanne, France and Université de Lyon, Lyon, France*
[21]*III. Physikalisches Institut A, RWTH Aachen, Aachen, Germany*
[22]*Physikalisches Institut, Universität Bonn, Bonn, Germany*
[23]*Physikalisches Institut, Universität Freiburg, Freiburg, Germany*
[24]*Institut für Physik, Universität Mainz, Mainz, Germany*
[25]*Ludwig-Maximilians-Universität München, München, Germany*
[26]*Fachbereich Physik, University of Wuppertal, Wuppertal, Germany*
[27]*Panjab University, Chandigarh, India*
[28]*Delhi University, Delhi, India*
[29]*Tata Institute of Fundamental Research, Mumbai, India*
[30]*University College Dublin, Dublin, Ireland*
[31]*Korea Detector Laboratory, Korea University, Seoul, Korea*
[32]*SungKyunKwan University, Suwon, Korea*

[33]CINVESTAV, Mexico City, Mexico
[34]FOM-Institute NIKHEF and University of Amsterdam/NIKHEF, Amsterdam, The Netherlands
[35]Radboud University Nijmegen/NIKHEF, Nijmegen, The Netherlands
[36]Joint Institute for Nuclear Research, Dubna, Russia
[37]Institute for Theoretical and Experimental Physics, Moscow, Russia
[38]Moscow State University, Moscow, Russia
[39]Institute for High Energy Physics, Protvino, Russia
[40]Petersburg Nuclear Physics Institute, St. Petersburg, Russia
[41]Lund University, Lund, Sweden, Royal Institute of Technology and Stockholm University, Stockholm, Sweden, and Uppsala University, Uppsala, Sweden
[42]Lancaster University, Lancaster, United Kingdom
[43]Imperial College, London, United Kingdom
[44]University of Manchester, Manchester, United Kingdom
[45]University of Arizona, Tucson, Arizona 85721, USA
[46]Lawrence Berkeley National Laboratory and University of California, Berkeley, California 94720, USA
[47]California State University, Fresno, California 93740, USA
[48]University of California, Riverside, California 92521, USA
[49]Florida State University, Tallahassee, Florida 32306, USA
[50]Fermi National Accelerator Laboratory, Batavia, Illinois 60510, USA
[51]University of Illinois at Chicago, Chicago, Illinois 60607, USA
[52]Northern Illinois University, DeKalb, Illinois 60115, USA
[53]Northwestern University, Evanston, Illinois 60208, USA
[54]Indiana University, Bloomington, Indiana 47405, USA
[55]University of Notre Dame, Notre Dame, Indiana 46556, USA
[56]Purdue University Calumet, Hammond, Indiana 46323, USA
[57]Iowa State University, Ames, Iowa 50011, USA
[58]University of Kansas, Lawrence, Kansas 66045, USA
[59]Kansas State University, Manhattan, Kansas 66506, USA
[60]Louisiana Tech University, Ruston, Louisiana 71272, USA
[61]University of Maryland, College Park, Maryland 20742, USA
[62]Boston University, Boston, Massachusetts 02215, USA
[63]Northeastern University, Boston, Massachusetts 02115, USA
[64]University of Michigan, Ann Arbor, Michigan 48109, USA
[65]Michigan State University, East Lansing, Michigan 48824, USA
[66]University of Mississippi, University, Mississippi 38677, USA
[67]University of Nebraska, Lincoln, Nebraska 68588, USA
[68]Princeton University, Princeton, New Jersey 08544, USA
[69]State University of New York, Buffalo, New York 14260, USA
[70]Columbia University, New York, New York 10027, USA
[71]University of Rochester, Rochester, New York 14627, USA
[72]State University of New York, Stony Brook, New York 11794, USA
[73]Brookhaven National Laboratory, Upton, New York 11973, USA
[74]Langston University, Langston, Oklahoma 73050, USA
[75]University of Oklahoma, Norman, Oklahoma 73019, USA
[76]Oklahoma State University, Stillwater, Oklahoma 74078, USA
[77]Brown University, Providence, Rhode Island 02912, USA
[78]University of Texas, Arlington, Texas 76019, USA
[79]Southern Methodist University, Dallas, Texas 75275, USA
[80]Rice University, Houston, Texas 77005, USA
[81]University of Virginia, Charlottesville, Virginia 22901, USA
[82]University of Washington, Seattle, Washington 98195, USA

(Received 17 February 2008; published 6 August 2008)

We report on a measurement of the inclusive jet cross section in $p\bar{p}$ collisions at a center-of-mass energy $\sqrt{s} = 1.96$ TeV using data collected by the D0 experiment at the Fermilab Tevatron Collider corresponding to an integrated luminosity of 0.70 fb^{-1}. The data cover jet transverse momenta from 50 to 600 GeV and jet rapidities in the range -2.4 to 2.4. Detailed studies of correlations between systematic uncertainties in transverse momentum and rapidity are presented, and the cross section measurements are found to be in good agreement with next-to-leading order QCD calculations.

DOI: 10.1103/PhysRevLett.101.062001 PACS numbers: 13.87.Ce, 12.38.Qk

The measurement of the cross section for the inclusive production of jets in hadron collisions provides stringent tests of quantum chromodynamics (QCD). When the transverse momentum (p_T) of the jet with respect to the beam axis is large, contributions from long-distance processes are small and the production of jets can be calculated in perturbative QCD (pQCD). The inclusive jet cross section in $p\bar{p}$ collisions at large p_T provides one of the most direct probes of physics at small distances. In particular, it is directly sensitive to the strong coupling constant (α_s) and the parton distribution functions (PDFs) of the proton. Additionally, it can be used to set constraints on the internal structure of quarks [1]. Deviations from pQCD predictions at large p_T can indicate new physical phenomena not described by the standard model of particle physics. A measurement over the widest possible rapidity range provides simultaneous sensitivity to the PDFs as well as new phenomena expected to populate mainly low rapidities. These data will have a strong impact on physics at the CERN Large Hadron Collider (LHC) where searches for new particles and higher dimensions suffer from poor knowledge of PDFs [2].

In this Letter, we report on a measurement from the D0 experiment of the inclusive jet cross section in $p\bar{p}$ collisions at a center-of-mass of $\sqrt{s} = 1.96$ TeV. The data sample, collected with the D0 detector during 2004–2005 in run II of the Fermilab Tevatron Collider, corresponds to an integrated luminosity of $\mathcal{L} = 0.70$ fb^{-1} [3]. The increased $p\bar{p}$ center-of-mass energy between run I ($\sqrt{s} = 1.8$ TeV) and run II leads to a significant increase in the cross section at large p_T—a factor of 3 at $p_T \sim 550$ GeV. The cross section is presented in six bins of jet rapidity (y), extending out to $|y| = 2.4$, as a function of jet p_T starting at $p_T = 50$ GeV, and provides the largest data set of the inclusive jet spectra at the Tevatron with the smallest experimental uncertainties to date. The measurement also extends earlier inclusive jet cross section measurements by the CDF and D0 Collaborations [4,5] and improves the systematic uncertainties compared with previous measurements by up to a factor of 2 over a range of rapidity up to 2.4 at high p_T.

The primary tool for jet detection is the finely segmented liquid-argon and uranium calorimeter that has almost complete solid angular coverage [6]. The central calorimeter (CC) covers the pseudorapidity region $|\eta| < 1.1$ and the two end cap calorimeters (EC) extend the coverage up to $|\eta| \sim 4.2$. The intercryostat region (ICR) between the CC and EC contains scintillator-based detectors that supplement the coverage of the calorimeter. The run II iterative seed-based cone jet algorithm including midpoints [7] with cone radius $\mathcal{R} = \sqrt{(\Delta y)^2 + (\Delta\phi)^2} = 0.7$ in rapidity y and azimuthal angle ϕ is used to cluster energies deposited in calorimeter towers. The same algorithm is used for partons in the pQCD calculations. The binning in jet p_T is commensurate with the measured p_T resolution.

Events are required to satisfy jet trigger requirements. Only jets above a given p_T threshold are kept by the highest level trigger (L3). The cross section is corrected for jet trigger inefficiencies (always below 2%) determined using an independent sample of muon triggered events.

The jet p_T is corrected for the energy response of the calorimeter, energy showering in and out the jet cone, and additional energy from event pileup and multiple proton interactions. After applying these corrections, the jet four momentum is given at the particle level, which means that they represent the real energy of the jet made out of the stable particles resulting from the hadronization process following the hard $p\bar{p}$ interaction. The electromagnetic part of the calorimeter is calibrated using $Z \to e^+e^-$ events [8]. The jet response for the region $|\eta| < 0.4$ is determined using the momentum imbalance in γ + jet events. The p_T imbalance in dijet events with one jet in $|\eta| < 0.4$ and the other anywhere in η is used to intercalibrate the jet response in η, as a function of jet p_T. Jet energy scale corrections are typically ~50% (20%) of the jet energy at 50 (400) GeV. Further corrections due to the difference in response between quark- and gluon-initiated jets are computed using the PYTHIA [9] event generator, passed through a GEANT-based [10] simulation of the detector response. These corrections amount to $\sim +4\%$ at jet energies of 50 GeV and $\sim -2\%$ at 400 GeV in the CC. The relative uncertainty of the jet p_T calibration ranges from 1.2% at $p_T \sim 150$ GeV to 1.5% at 500 GeV in the CC, and 1.5%–2% in the ICR and EC.

The position of the $p\bar{p}$ interaction is reconstructed using a tracking system consisting of silicon microstrip detectors and scintillating fibers located inside a solenoidal magnetic field of 2 T [6]. The position of the vertex along the beam line is required to be within 50 cm of the detector center. The signal efficiency of this requirement is $93.0 \pm 0.5\%$. A requirement is placed on the missing transverse energy in the event, computed as the transverse component of the vector sum of the momenta in calorimeter cells, to suppress the cosmic ray background and is >99.5% efficient for signal. Requirements on characteristics of shower development are used to remove the remaining background due to electrons, photons, and detector noise that mimic jets. The efficiency for these requirements is >99% (>97.5% in the ICR). After all these requirements, the background is <0.1% in our sample.

The D0 detector simulation provides a good description of jet properties including characteristics of the shower development. The correction to the jet cross section for muons and neutrinos, not reconstructed within jets, is determined using PYTHIA and is 2%, independent of p_T and y. The corrections for jet migration between bins in p_T and y due to finite resolution in energy and position are determined in an unfolding procedure, based on the experimental p_T and y resolutions. The jet p_T resolution is obtained using the p_T imbalance in dijet events and is

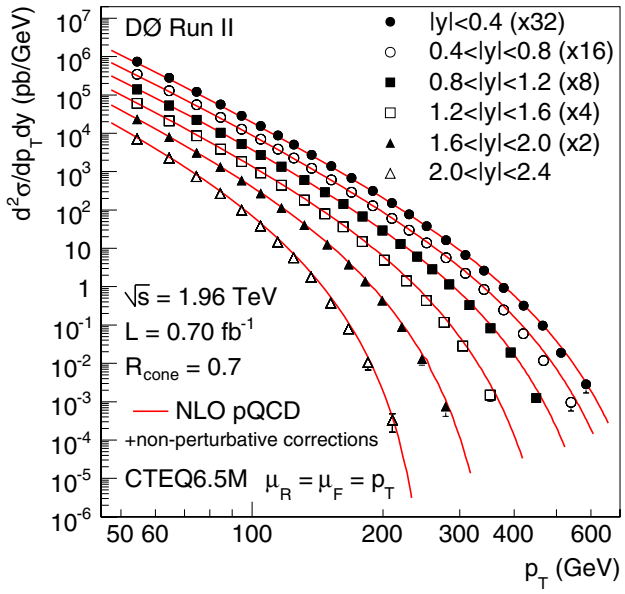

FIG. 1 (color online). The inclusive jet cross section as a function of jet p_T in six $|y|$ bins. The data points are multiplied by 2, 4, 8, 16, and 32 for the bins $1.6 < |y| < 2.0$, $1.2 < |y| < 1.6$, $0.8 < |y| < 1.2$, $0.4 < |y| < 0.8$, and $|y| < 0.4$, respectively.

found to decrease from 13% at $p_T \sim 50$ GeV to 7% at $p_T \sim 400$ GeV in both the CC and the EC. The resolution in the ICR is 16% at $p_T \sim 50$ GeV decreasing to 11% at $p_T \sim 400$ GeV. The method to unfold the data uses a four-parameter ansatz function [11] to parametrize the p_T dependence of the jet cross section convoluted with the measured p_T resolution and fitted to the experimental data.

The unfolding corrections vary between 20% at a jet $p_T \sim 50$ GeV and 40% at 400 GeV in the CC. In the EC and the ICR, the corrections are less than 20% at $p_T \sim 50$ GeV, but increase to 80% at the largest p_T and y. Bin sizes in p_T and y are chosen to minimize migration corrections due to the experimental resolution. The y resolution is better than 0.05 (0.01) for jets with $p_T \sim 50$ GeV (400 GeV), and leads to a migration correction less than 2% in most bins, and 10% in the highest y bin.

The results of the inclusive jet cross section measurement corrected to the particle level are displayed in Fig. 1 in six $|y|$ bins as a function of p_T. The cross section extends over more than 8 orders of magnitude from $p_T = 50$ GeV to $p_T > 600$ GeV. Perturbative QCD predictions to next-to-leading order (NLO) in α_S, computed using the FASTNLO program [12] (based on NLOJET++ [13]) and the PDFs from CTEQ6.5M [14], are compared to the data. The renormalization and factorization scales (μ_R and μ_F) are set to the individual jet p_T. The theoretical uncertainty, determined by changing μ_R and μ_F between $p_T/2$ and $2p_T$, is of the order of 10% in all bins. The predictions are corrected for nonperturbative contributions due to the underlying event and hadronization computed by PYTHIA with the CTEQ6.5M PDFs, the QW tune [15], and the two-loop formula for α_S. These nonperturbative corrections to theory extend from +10% to +20% at $p_T \sim 50$ GeV between $|y| < 0.4$ and $2.0 < |y| < 2.4$. The corrections are of order +5% for $p_T \sim 100$ GeV, and smaller than +2% above 200 GeV.

The ratio of the data to the theory is shown in Fig. 2. The dashed lines show the uncertainties due to the different PDFs coming from the CTEQ6.5 parametrizations. The predictions from MRST2004 [16] are displayed by the large dashed line. In all y regions, the predictions agree well with the data. There is a tendency for the data to be lower than the central CTEQ prediction—particularly at very large p_T—but they lie mostly within the CTEQ PDF uncertainty band. The p_T dependence of the data is well reproduced by the MRST parametrization whose systematic uncertainty is slightly smaller than that from the CTEQ

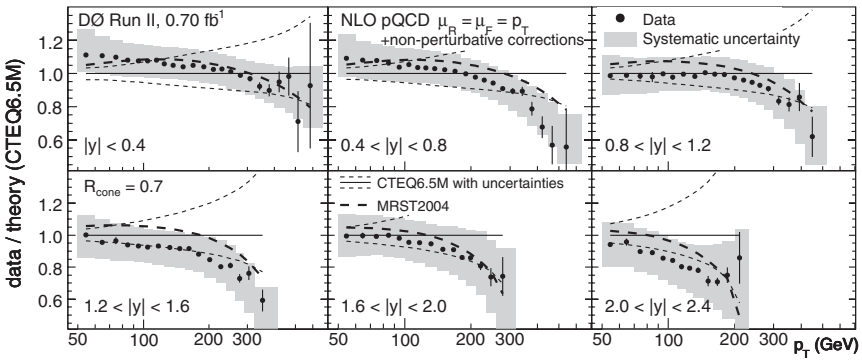

FIG. 2. Measured data divided by theory for the inclusive jet cross section as a function of jet p_T in six $|y|$ bins. The data systematic uncertainties are displayed by the full shaded band. NLO pQCD calculations, with renormalization and factorization scales set to jet p_T using the CTEQ6.5M PDFs and including nonperturbative corrections, are compared to the data. The CTEQ6.5 PDF uncertainties are shown as small dashed lines and the predictions with MRST2004 PDFs as large dashed lines. The theoretical scale uncertainty, obtained by varying the factorization and renormalization scales between $\mu_R = \mu_F = p_T/2$ and $\mu_R = \mu_F = 2p_T$, is typically 10%–15%.

parametrization. The experimental systematic uncertainty is comparable to the PDF uncertainties. The theoretical scale uncertainty, obtained by varying the factorization and renormalization scales between $\mu_R = \mu_F = p_T/2$ and $\mu_R = \mu_F = 2p_T$, is typically 10%–15%. In most bins, the experimental uncertainties are of the same order as the theoretical uncertainties. Tables of the cross sections together with their uncertainties are given in Ref. [17].

Correlations between systematic uncertainties are studied in detail to increase the value of these data in future PDF fits [17] and their impact on LHC physics, in particular. Point-to-point correlations in p_T and y are provided for the 24 sources of systematic uncertainty. The relative uncertainties in percent on the cross section measurement are shown in Fig. 3 for the five most significant sources of systematic uncertainty in $|y| < 0.4$ and $2.0 < |y| < 2.4$. The luminosity uncertainty of 6.1%, fully correlated in p_T and y, is not displayed in Fig. 3. The other y bins have similar correlations in shape and values between these two extreme bins. The total uncorrelated uncertainty is $<3\%$ in the CC, and $<15\%$ in the EC.

The two largest systematic uncertainties are due to the electromagnetic energy scale obtained from $Z \to e^+e^-$ events [8], and the photon energy scale in the CC obtained using the difference in the calorimeter response between photons and electrons in the detector simulation. The uncertainty on the photon energy scale is mainly due to the limited knowledge of the amount of dead material in front of the calorimeter and from the physics modeling

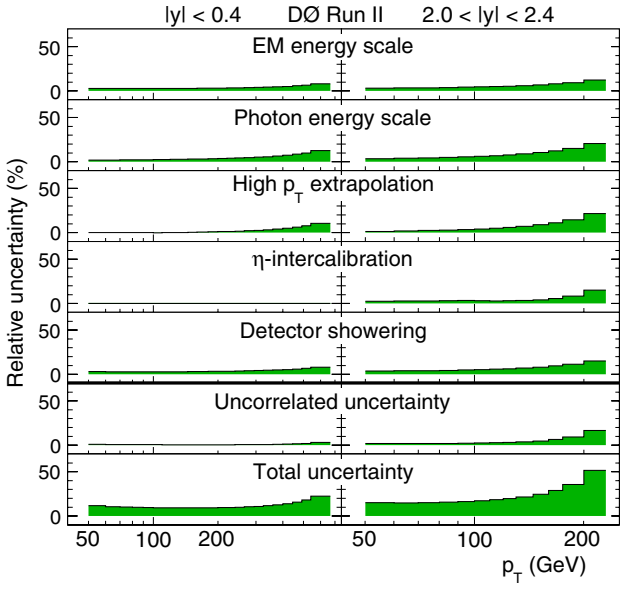

FIG. 3 (color online). Correlated uncertainties for $|y| < 0.4$ and $2.0 < |y| < 2.4$ as a function of jet p_T. The five largest systematic uncertainties are shown together with uncorrelated and total uncertainties, computed as a sum in quadrature of all sources.

of electromagnetic showers in the GEANT-based [10] simulation. These two contributions to the jet cross section uncertainty are $\sim 5\%$ in the CC and 5%–15% in the EC.

The large-p_T extrapolation of jet energy scale is determined using the detector simulation with the single-pion response tuned to γ + jet data. The uncertainty rises to 12% (30%) in the CC (EC), and is dominated by the uncertainty in the jet fragmentation, estimated by comparing the fragmentation models in PYTHIA and HERWIG [18]. The uncertainty in η intercalibration corresponds to systematic uncertainties associated with the procedure to equalize the calorimeter response in different regions of η in dijet events. These systematic uncertainties are negligible in the CC because the η dependent response is calibrated with respect to the CC, but extend up to 25% in the EC. Finally, systematic uncertainties associated with showering effects, due primarily to the modeling of the hadronic shower development in the detector and differences between PYTHIA and HERWIG, range from 3% at low p_T to 7% (15%) at large p_T in the CC (EC).

To show the potential impact of using point-to-point uncertainty correlations in jet p_T and y on PDF determination, we give in Fig. 3 the uncorrelated and total systematic uncertainties as a function of jet p_T as a percentage of the jet cross section measurement. The total uncorrelated uncertainties are less than 15% and 25% of the full uncertainties in the CC and EC, respectively. The full systematic uncertainties are similar in size to the PDF uncertainties (Fig. 2) and the detailed analysis of the correlations which have been performed will make it possible to further constrain the PDFs. Knowledge of these correlations is especially important for constraining the PDFs in next-to-next-leading-order pQCD fits where the uncertainties due to the dependence on the choice of the renormalization and factorization scales are smaller. The point-to-point correlations for the 24 different sources of systematic uncertainties are given in Ref. [17].

In conclusion, the measured inclusive jet cross section corrected for experimental effects to the particle level in $p\bar{p}$ collisions at $\sqrt{s} = 1.96$ TeV with $\mathcal{L} = 0.70$ fb^{-1} is presented for six $|y|$ bins as a function of jet p_T, substantially extending the kinematic reach and improving the precision of existing inclusive jet measurements. NLO pQCD calculations with CTEQ6.5M or MRST2004 PDFs agree with the data and favor the lower edge of the CTEQ6.5 PDF uncertainty band at large p_T and the shape of the p_T dependence for MRST2004. A full analysis of correlations between sources of systematic uncertainty is performed, increasing the potential impact of these data in global PDF fits and on new phenomena searches at the LHC.

We thank the staffs at Fermilab and collaborating institutions, and acknowledge support from the DOE and NSF (U.S.); CEA and CNRS/IN2P3 (France); FASI, Rosatom

and RFBR (Russia); CAPES, CNPq, FAPERJ, FAPESP, and FUNDUNESP (Brazil); DAE and DST (India); Colciencias (Colombia); CONACyT (Mexico); KRF and KOSEF (Korea); CONICET and UBACyT (Argentina); FOM (The Netherlands); STFC (U.K.); MSMT and GACR (Czech Republic); CRC Program, CFI, NSERC, and WestGrid Project (Canada); BMBF and DFG (Germany); SFI (Ireland); The Swedish Research Council (Sweden); CAS and CNSF (China); and the Alexander von Humboldt Foundation.

[*]Visitor from Augustana College, Sioux Falls, SD, USA.
[†]Visitor from The University of Liverpool, Liverpool, United Kingdom.
[‡]Visitor from ICN-UNAM, Mexico City, Mexico.
[§]Visitor from II. Physikalisches Institut, Georg-August-University, Göttingen, Germany.
[‖]Visitor from Helsinki Institute of Physics, Helsinki, Finland.
[¶]Visitor from Universität Zürich, Zürich, Switzerland.
[**]Deceased.

[1] E. J. Eichten, K. D. Lane, and M. E. Peskin, Phys. Rev. Lett. **50**, 811 (1983).
[2] A. Belyaev *et al.*, J. High Energy Phys. 01 (2006) 069.
[3] T. Andeen *et al.*, FERMILAB, Report No. FERMILAB-TM-2365, 2007.
[4] A. Abulencia *et al.* (CDF Collaboration), Phys. Rev. D **75**, 092006 (2007); Phys. Rev. D **74**, 071103 (2006).
[5] B. Abbott *et al.*, Phys. Rev. Lett. **82**, 2451 (1999); **86**, 1707 (2001); F. Abe *et al.* (CDF Collaboration), Phys. Rev. Lett. **77**, 438 (1996).
[6] V. M. Abazov *et al.* (D0 Collaboration), Nucl. Instrum. Methods Phys. Res., Sect. A **565**, 463 (2006).
[7] G. C. Blazey *et al.*, in *Proceedings of the Workshop: "QCD and Weak Boson Physics in Run II,"* edited by U. Baur, R. K. Ellis, and D. Zeppenfeld (Batavia, Illinois, 2000), p. 47.
[8] V. M. Abazov *et al.* (D0 Collaboration), Phys. Rev. D **76**, 012003 (2007).
[9] T. Sjöstrand *et al.*, Comput. Phys. Commun. **135**, 238 (2001).
[10] R. Brun and F. Carminati, CERN Program Library Long Writeup Report No. W5013, 1993 (unpublished).
[11] B. Abbott *et al.* (D0 Collaboration), Phys. Rev. D **64**, 032003 (2001).
[12] T. Kluge, K. Rabbertz, and M. Wobisch, arXiv:hep-ph/0609285.
[13] Z. Nagy, Phys. Rev. D **68**, 094002 (2003).
[14] W. K. Tung *et al.*, J. High Energy Phys. 02 (2007) 053; J. Pumplin *et al.*, J. High Energy Phys. 07 (2002) 12; D. Stump *et al.*, J. High Energy Phys. 10 (2003) 046.
[15] R. Field *et al.* (TeV4LHC QCD Working Group), arXiv:hep-ph/0610012.
[16] A. D. Martin *et al.*, Phys. Lett. B **604**, 61 (2004).
[17] See EPAPS Document No. E-PRLTAO-101-033833 for the inclusive jet cross section measurement and the correlation studies. For more information on EPAPS, see http://www.aip.org/pubservs/epaps.html.
[18] G. Marchesini *et al.*, Comput. Phys. Commun. **67**, 465 (1992).

PHYSICAL REVIEW D **85,** 052006 (2012)

Measurement of the inclusive jet cross section in $p\bar{p}$ collisions at $\sqrt{s}=1.96$ TeV

V. M. Abazov,[35] B. Abbott,[73] B. S. Acharya,[29] M. Adams,[49] T. Adams,[47] G. D. Alexeev,[35] G. Alkhazov,[39] A. Alton,[61,*] G. Alverson,[60] G. A. Alves,[2] M. Aoki,[48] A. Askew,[47] B. Åsman,[41] S. Atkins,[58] O. Atramentov,[65] K. Augsten,[10] C. Avila,[8] J. BackusMayes,[80] F. Badaud,[13] L. Bagby,[48] B. Baldin,[48] D. V. Bandurin,[47] S. Banerjee,[29] E. Barberis,[60] P. Baringer,[56] J. Barreto,[3] J. F. Bartlett,[48] U. Bassler,[18] V. Bazterra,[49] A. Bean,[56] M. Begalli,[3] C. Belanger-Champagne,[41] L. Bellantoni,[48] S. B. Beri,[27] G. Bernardi,[17] R. Bernhard,[22] I. Bertram,[42] M. Besançon,[18] R. Beuselinck,[43] V. A. Bezzubov,[38] P. C. Bhat,[48] V. Bhatnagar,[27] G. Blazey,[50] S. Blessing,[47] K. Bloom,[64] A. Boehnlein,[48] D. Boline,[70] E. E. Boos,[37] G. Borissov,[42] T. Bose,[59] A. Brandt,[76] O. Brandt,[23] R. Brock,[62] G. Brooijmans,[68] A. Bross,[48] D. Brown,[17] J. Brown,[17] X. B. Bu,[48] M. Buehler,[48] V. Buescher,[24] V. Bunichev,[37] S. Burdin,[42,†] T. H. Burnett,[80] C. P. Buszello,[41] B. Calpas,[15] E. Camacho-Pérez,[32] M. A. Carrasco-Lizarraga,[56] B. C. K. Casey,[48] H. Castilla-Valdez,[32] S. Chakrabarti,[70] D. Chakraborty,[50] K. M. Chan,[54] A. Chandra,[78] E. Chapon,[18] G. Chen,[56] S. Chevalier-Théry,[18] D. K. Cho,[75] S. W. Cho,[31] S. Choi,[31] B. Choudhary,[28] S. Cihangir,[48] D. Claes,[64] J. Clutter,[56] M. Cooke,[48] W. E. Cooper,[48] M. Corcoran,[78] F. Couderc,[18] M.-C. Cousinou,[15] A. Croc,[18] D. Cutts,[75] A. Das,[45] G. Davies,[43] K. De,[76] S. J. de Jong,[34] E. De La Cruz-Burelo,[32] F. Déliot,[18] R. Demina,[69] D. Denisov,[48] S. P. Denisov,[38] S. Desai,[48] C. Deterre,[18] K. DeVaughan,[64] H. T. Diehl,[48] M. Diesburg,[48] P. F. Ding,[44] A. Dominguez,[64] T. Dorland,[80] A. Dubey,[28] L. V. Dudko,[37] D. Duggan,[65] A. Duperrin,[15] S. Dutt,[27] A. Dyshkant,[50] M. Eads,[64] D. Edmunds,[62] J. Ellison,[46] V. D. Elvira,[48] Y. Enari,[17] H. Evans,[52] A. Evdokimov,[71] V. N. Evdokimov,[38] G. Facini,[60] T. Ferbel,[69] F. Fiedler,[24] F. Filthaut,[34] W. Fisher,[62] H. E. Fisk,[48] M. Fortner,[50] H. Fox,[42] S. Fuess,[48] A. Garcia-Bellido,[69] G. A. García-Guerra,[32,‡] V. Gavrilov,[36] P. Gay,[13] W. Geng,[15,62] D. Gerbaudo,[66] C. E. Gerber,[49] Y. Gershtein,[65] D. Gillberg,[6] G. Ginther,[48,69] G. Golovanov,[35] A. Goussiou,[80] P. D. Grannis,[70] S. Greder,[19] H. Greenlee,[48] Z. D. Greenwood,[58] E. M. Gregores,[4] G. Grenier,[20] Ph. Gris,[13] J.-F. Grivaz,[16] A. Grohsjean,[18] S. Grünendahl,[48] M. W. Grünewald,[30] T. Guillemin,[16] G. Gutierrez,[48] P. Gutierrez,[73] A. Haas,[68,§] S. Hagopian,[47] J. Haley,[60] L. Han,[7] K. Harder,[44] A. Harel,[69] J. M. Hauptman,[55] J. Hays,[43] T. Head,[44] T. Hebbeker,[21] D. Hedin,[50] H. Hegab,[74] J. G. Hegeman,[33] A. P. Heinson,[46] U. Heintz,[75] C. Hensel,[23] I. Heredia-De La Cruz,[32] K. Herner,[61] G. Hesketh,[44,‖] M. D. Hildreth,[54] R. Hirosky,[79] T. Hoang,[47] J. D. Hobbs,[70] B. Hoeneisen,[12] M. Hohlfeld,[24] Z. Hubacek,[10,18] V. Hynek,[10] I. Iashvili,[67] Y. Ilchenko,[77] R. Illingworth,[48] A. S. Ito,[48] S. Jabeen,[75] M. Jaffré,[16] D. Jamin,[15] A. Jayasinghe,[73] R. Jesik,[43] K. Johns,[45] M. Johnson,[48] A. Jonckheere,[48] P. Jonsson,[43] J. Joshi,[27] A. W. Jung,[48] A. Juste,[40] K. Kaadze,[57] E. Kajfasz,[15] D. Karmanov,[37] P. A. Kasper,[48] I. Katsanos,[64] R. Kehoe,[77] S. Kermiche,[15] N. Khalatyan,[48] A. Khanov,[74] A. Kharchilava,[67] Y. N. Kharzheev,[35] J. M. Kohli,[27] A. V. Kozelov,[38] J. Kraus,[62] S. Kulikov,[38] A. Kumar,[67] A. Kupco,[11] T. Kurča,[20] V. A. Kuzmin,[37] J. Kvita,[9] S. Lammers,[52] G. Landsberg,[75] P. Lebrun,[20] H. S. Lee,[31] S. W. Lee,[55] W. M. Lee,[48] J. Lellouch,[17] L. Li,[46] Q. Z. Li,[48] S. M. Lietti,[5] J. K. Lim,[31] D. Lincoln,[48] J. Linnemann,[62] V. V. Lipaev,[38] R. Lipton,[48] Y. Liu,[7] A. Lobodenko,[39] M. Lokajicek,[11] R. Lopes de Sa,[70] H. J. Lubatti,[80] R. Luna-Garcia,[32,¶] A. L. Lyon,[48] A. K. A. Maciel,[2] D. Mackin,[78] R. Madar,[18] R. Magaña-Villalba,[32] N. Makovec,[16] S. Malik,[64] V. L. Malyshev,[35] Y. Maravin,[57] J. Martínez-Ortega,[32] R. McCarthy,[70] C. L. McGivern,[56] M. M. Meijer,[34] A. Melnitchouk,[63] D. Menezes,[50] P. G. Mercadante,[4] M. Merkin,[37] A. Meyer,[21] J. Meyer,[23] F. Miconi,[19] N. K. Mondal,[29] G. S. Muanza,[15] M. Mulhearn,[79] E. Nagy,[15] M. Naimuddin,[28] M. Narain,[75] R. Nayyar,[28] H. A. Neal,[61] J. P. Negret,[8] P. Neustroev,[39] S. F. Novaes,[5] T. Nunnemann,[25] G. Obrant,[39,§§] J. Orduna,[78] N. Osman,[15] J. Osta,[54] G. J. Otero y Garzón,[1] M. Padilla,[46] A. Pal,[76] N. Parashar,[53] V. Parihar,[75] S. K. Park,[31] R. Partridge,[75,§] N. Parua,[52] A. Patwa,[71] B. Penning,[48] M. Perfilov,[37] Y. Peters,[44] K. Petridis,[44] G. Petrillo,[69] P. Pétroff,[16] R. Piegaia,[1] M.-A. Pleier,[71] P. L. M. Podesta-Lerma,[32,**] V. M. Podstavkov,[48] P. Polozov,[36] A. V. Popov,[38] M. Prewitt,[78] D. Price,[52] N. Prokopenko,[38] J. Qian,[61] A. Quadt,[23] B. Quinn,[63] M. S. Rangel,[2] K. Ranjan,[28] P. N. Ratoff,[42] I. Razumov,[38] P. Renkel,[77] M. Rijssenbeek,[70] I. Ripp-Baudot,[19] F. Rizatdinova,[74] M. Rominsky,[48] A. Ross,[42] C. Royon,[18] P. Rubinov,[48] R. Ruchti,[54] G. Safronov,[36] G. Sajot,[14] P. Salcido,[50] A. Sánchez-Hernández,[32] M. P. Sanders,[25] B. Sanghi,[48] A. S. Santos,[5] G. Savage,[48] L. Sawyer,[58] T. Scanlon,[43] R. D. Schamberger,[70] Y. Scheglov,[39] H. Schellman,[51] T. Schliephake,[26] S. Schlobohm,[80] C. Schwanenberger,[44] R. Schwienhorst,[62] J. Sekaric,[56] H. Severini,[73] E. Shabalina,[23] V. Shary,[18] A. A. Shchukin,[38] R. K. Shivpuri,[28] V. Simak,[10] V. Sirotenko,[48] P. Skubic,[73] P. Slattery,[69] D. Smirnov,[54] K. J. Smith,[67] G. R. Snow,[64] J. Snow,[72] S. Snyder,[71] S. Söldner-Rembold,[44] L. Sonnenschein,[21] K. Soustruznik,[9] J. Stark,[14] V. Stolin,[36] D. A. Stoyanova,[38] M. Strauss,[73] D. Strom,[49] L. Stutte,[48] L. Suter,[44] P. Svoisky,[73] M. Takahashi,[44] A. Tanasijczuk,[1] M. Titov,[18] V. V. Tokmenin,[35] Y.-T. Tsai,[69] K. Tschann-Grimm,[70] D. Tsybychev,[70] B. Tuchming,[18] C. Tully,[66] L. Uvarov,[39] S. Uvarov,[39] S. Uzunyan,[50] R. Van Kooten,[52] W. M. van Leeuwen,[33] N. Varelas,[49] E. W. Varnes,[45] I. A. Vasilyev,[38] P. Verdier,[20] L. S. Vertogradov,[35] M. Verzocchi,[48] M. Vesterinen,[44] D. Vilanova,[18] P. Vokac,[10] M. Voutilainen,[64,††] H. D. Wahl,[47] M. H. L. S. Wang,[48]

J. Warchol,[54] G. Watts,[80] M. Wayne,[54] M. Weber,[48,‡‡] L. Welty-Rieger,[51] A. White,[76] D. Wicke,[26] M. R. J. Williams,[42] G. W. Wilson,[56] M. Wobisch,[58] D. R. Wood,[60] T. R. Wyatt,[44] Y. Xie,[48] R. Yamada,[48] W.-C. Yang,[44] T. Yasuda,[48] Y. A. Yatsunenko,[35] Z. Ye,[48] H. Yin,[48] K. Yip,[71] S. W. Youn,[48] J. Yu,[76] T. Zhao,[80] B. Zhou,[61] J. Zhu,[61] M. Zielinski,[69] D. Zieminska,[52] and L. Zivkovic[75]

(D0 Collaboration)

[1]*Universidad de Buenos Aires, Buenos Aires, Argentina*
[2]*LAFEX, Centro Brasileiro de Pesquisas Físicas, Rio de Janeiro, Brazil*
[3]*Universidade do Estado do Rio de Janeiro, Rio de Janeiro, Brazil*
[4]*Universidade Federal do ABC, Santo André, Brazil*
[5]*Instituto de Física Teórica, Universidade Estadual Paulista, São Paulo, Brazil*
[6]*Simon Fraser University, Vancouver, British Columbia, and York University, Toronto, Ontario, Canada*
[7]*University of Science and Technology of China, Hefei, People's Republic of China*
[8]*Universidad de los Andes, Bogotá, Colombia*
[9]*Charles University, Faculty of Mathematics and Physics, Center for Particle Physics, Prague, Czech Republic*
[10]*Czech Technical University in Prague, Prague, Czech Republic*
[11]*Center for Particle Physics, Institute of Physics, Academy of Sciences of the Czech Republic, Prague, Czech Republic*
[12]*Universidad San Francisco de Quito, Quito, Ecuador*
[13]*LPC, Université Blaise Pascal, CNRS/IN2P3, Clermont, France*
[14]*LPSC, Université Joseph Fourier Grenoble 1, CNRS/IN2P3, Institut National Polytechnique de Grenoble, Grenoble, France*
[15]*CPPM, Aix-Marseille Université, CNRS/IN2P3, Marseille, France*
[16]*LAL, Université Paris-Sud, CNRS/IN2P3, Orsay, France*
[17]*LPNHE, Universités Paris VI and VII, CNRS/IN2P3, Paris, France*
[18]*CEA, Irfu, SPP, Saclay, France*
[19]*IPHC, Université de Strasbourg, CNRS/IN2P3, Strasbourg, France*
[20]*IPNL, Université Lyon 1, CNRS/IN2P3, Villeurbanne, France and Université de Lyon, Lyon, France*
[21]*III. Physikalisches Institut A, RWTH Aachen University, Aachen, Germany*
[22]*Physikalisches Institut, Universität Freiburg, Freiburg, Germany*
[23]*II. Physikalisches Institut, Georg-August-Universität Göttingen, Göttingen, Germany*
[24]*Institut für Physik, Universität Mainz, Mainz, Germany*
[25]*Ludwig-Maximilians-Universität München, München, Germany*
[26]*Fachbereich Physik, Bergische Universität Wuppertal, Wuppertal, Germany*
[27]*Panjab University, Chandigarh, India*
[28]*Delhi University, Delhi, India*
[29]*Tata Institute of Fundamental Research, Mumbai, India*
[30]*University College Dublin, Dublin, Ireland*
[31]*Korea Detector Laboratory, Korea University, Seoul, Korea*
[32]*CINVESTAV, Mexico City, Mexico*
[33]*Nikhef, Science Park, Amsterdam, the Netherlands*
[34]*Radboud University Nijmegen, Nijmegen, the Netherlands and Nikhef, Science Park, Amsterdam, the Netherlands*
[35]*Joint Institute for Nuclear Research, Dubna, Russia*
[36]*Institute for Theoretical and Experimental Physics, Moscow, Russia*
[37]*Moscow State University, Moscow, Russia*
[38]*Institute for High Energy Physics, Protvino, Russia*
[39]*Petersburg Nuclear Physics Institute, St. Petersburg, Russia*
[40]*Institució Catalana de Recerca i Estudis Avançats (ICREA) and Institut de Física d'Altes Energies (IFAE), Barcelona, Spain*
[41]*Stockholm University, Stockholm and Uppsala University, Uppsala, Sweden*
[42]*Lancaster University, Lancaster LA1 4YB, United Kingdom*
[43]*Imperial College London, London SW7 2AZ, United Kingdom*
[44]*The University of Manchester, Manchester M13 9PL, United Kingdom*
[45]*University of Arizona, Tucson, Arizona 85721, USA*
[46]*University of California Riverside, Riverside, California 92521, USA*
[47]*Florida State University, Tallahassee, Florida 32306, USA*
[48]*Fermi National Accelerator Laboratory, Batavia, Illinois 60510, USA*
[49]*University of Illinois at Chicago, Chicago, Illinois 60607, USA*
[50]*Northern Illinois University, DeKalb, Illinois 60115, USA*
[51]*Northwestern University, Evanston, Illinois 60208, USA*
[52]*Indiana University, Bloomington, Indiana 47405, USA*

[53]Purdue University Calumet, Hammond, Indiana 46323, USA
[54]University of Notre Dame, Notre Dame, Indiana 46556, USA
[55]Iowa State University, Ames, Iowa 50011, USA
[56]University of Kansas, Lawrence, Kansas 66045, USA
[57]Kansas State University, Manhattan, Kansas 66506, USA
[58]Louisiana Tech University, Ruston, Louisiana 71272, USA
[59]Boston University, Boston, Massachusetts 02215, USA
[60]Northeastern University, Boston, Massachusetts 02115, USA
[61]University of Michigan, Ann Arbor, Michigan 48109, USA
[62]Michigan State University, East Lansing, Michigan 48824, USA
[63]University of Mississippi, University, Mississippi 38677, USA
[64]University of Nebraska, Lincoln, Nebraska 68588, USA
[65]Rutgers University, Piscataway, New Jersey 08855, USA
[66]Princeton University, Princeton, New Jersey 08544, USA
[67]State University of New York, Buffalo, New York 14260, USA
[68]Columbia University, New York, New York 10027, USA
[69]University of Rochester, Rochester, New York 14627, USA
[70]State University of New York, Stony Brook, New York 11794, USA
[71]Brookhaven National Laboratory, Upton, New York 11973, USA
[72]Langston University, Langston, Oklahoma 73050, USA
[73]University of Oklahoma, Norman, Oklahoma 73019, USA
[74]Oklahoma State University, Stillwater, Oklahoma 74078, USA
[75]Brown University, Providence, Rhode Island 02912, USA
[76]University of Texas, Arlington, Texas 76019, USA
[77]Southern Methodist University, Dallas, Texas 75275, USA
[78]Rice University, Houston, Texas 77005, USA
[79]University of Virginia, Charlottesville, Virginia 22901, USA
[80]University of Washington, Seattle, Washington 98195, USA

(Received 17 October 2011; published 20 March 2012)

We present a measurement of the inclusive jet cross section using the Run II cone algorithm and data collected by the D0 experiment in $p\bar{p}$ collisions at a center-of-mass energy $\sqrt{s} = 1.96$ TeV, corresponding to an integrated luminosity of 0.70 fb^{-1}. The jet energy calibration and the method used to extract the inclusive jet cross section are described. We discuss the main uncertainties, which are dominated by the jet energy scale uncertainty. The results cover jet transverse momenta from 50 GeV to 600 GeV with jet rapidities in the range -2.4 to 2.4 and are compared to predictions using recent proton parton distribution functions. Studies of correlations between systematic uncertainties in transverse momentum and rapidity are presented.

DOI: 10.1103/PhysRevD.85.052006 PACS numbers: 13.87.Ce, 12.38.Qk

I. INTRODUCTION AND MOTIVATION

The measurement of the cross section for inclusive production of hadronic jets in hadron collisions provides stringent tests of quantum chromodynamics (QCD). The inclusive jet cross section in $p\bar{p}$ collisions for jets with large momentum transverse to the beam axis (p_T) is directly sensitive to the strong coupling constant (α_s) [1] and the parton distribution functions (PDFs) of the proton [2]. At the Tevatron $p\bar{p}$ collider, data are divided into two sets corresponding to Run I (1992—1996) and Run II (2002—2011). The increased $p\bar{p}$ center-of-mass energy between Run I ($\sqrt{s} = 1.8$ TeV) and Run II ($\sqrt{s} = 1.96$ TeV) leads to a significant increase in the cross section at large p_T—a factor of three at $p_T \approx 550$ GeV, as shown in Fig. 1 obtained using the next-to-leading order (NLO) QCD calculation as implemented in NLOJET++ [3]. This increases the sensitivity to potential new observations such as quark compositeness [4,5] and extra dimensions [6,7]. The integrated luminosity of the inclusive jet cross section measurement discussed in this paper exceeds the Run I luminosity by more than a factor of five, allowing for more stringent constraints on the PDFs. In Fig. 2 we show the different subprocesses that contribute to the

*With visitor from Augustana College, Sioux Falls, SD, USA
†With visitor from The University of Liverpool, Liverpool, UK
‡With visitor from UPIITA-IPN, Mexico City, Mexico
§With visitor from SLAC, Menlo Park, CA, USA
‖With visitor from University College London, London, UK
¶With visitor from Centro de Investigacion en Computacion—IPN, Mexico City, Mexico
**With visitor from ECFM, Universidad Autonoma de Sinaloa, Culiacán, Mexico
††With visitor from Helsinki Institute of Physics, Helsinki, Finland
‡‡With visitor from Universität Bern, Bern, Switzerland
§§Deceased.

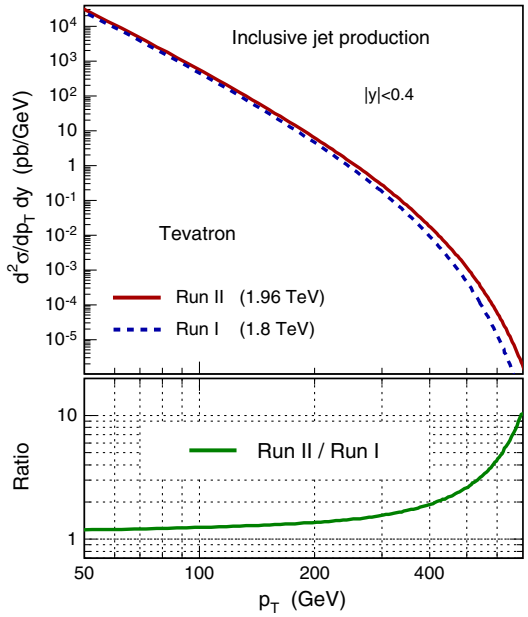

FIG. 1 (color online). (color online) Inclusive jet production cross section for central jets ($|y| < 0.4$) for Run I and Run II energies at the Tevatron obtained using NLO QCD as implemented in NLOJET++. The ratio of the two curves is shown in the bottom panel. We note an increase of the Run II cross section with respect to Run I of up to a factor 10 at highest jet p_T.

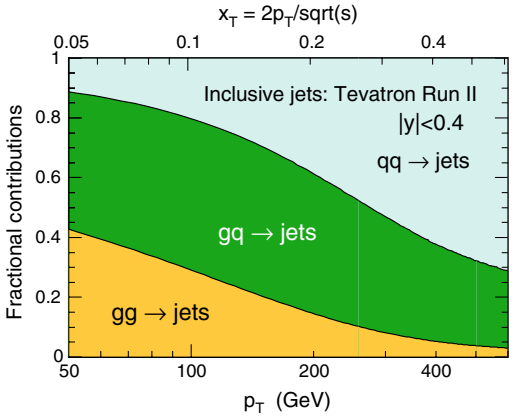

FIG. 2 (color online). (color online) Fractional contributions of the qq, qg and gg subprocesses to the inclusive jet cross section for central jets as a function of jet p_T and of the fraction of the beam energy carried by the jet, x_T.

inclusive jet cross section. In particular the gluon density can be further constrained using these data, since the gg and qg initial states contribute significantly to the cross section across almost the full p_T range of the measurement. The gluon distribution is still poorly known, especially for gluons carrying a large momentum fraction x. In contrast, the quark PDFs are already well constrained by fixed target and electron-proton collider experiments [2].

In this paper, we report measurements by the D0 collaboration of the inclusive jet cross section in $p\bar{p}$ collisions at a center-of-mass energy of $\sqrt{s} = 1.96$ TeV. We give details of the analysis leading to the results published in Refs. [8,9], with particular attention to the jet energy scale determination. The precision achieved for the jet energy scale in the D0 experiment is unprecedented for any hadron collider experiment to date, and the methods applied to reach this precision will be useful for future hadron collider experiments.

The data sample, collected with the D0 detector during 2004–2005 in Run II of the Fermilab Tevatron, corresponds to an integrated luminosity of $\mathcal{L} = 0.70$ fb^{-1} [10]. The cross section is presented in six bins of jet rapidity (y), extending to $|y| = 2.4$, as a function of jet p_T starting at $p_T = 50$ GeV. The rapidity is related to the polar scattering angle θ with respect to the beam axis by $y = 0.5\ln[(1 + \beta\cos\theta)/(1 - \beta\cos\theta)]$ with $\beta = |\vec{p}|/E$. The measurement also extends the kinematic reach of earlier measurements of the inclusive jet cross section by the CDF and D0 Collaborations [11–14].

This paper is organized as follows. After a brief description of the D0 detector in Sec. II, we discuss the jet algorithm used in Run II in Sec. III. Section IV describes the theoretical predictions for the inclusive jet cross section before the D0 measurement in Ref. [8]. Section V gives an extensive description of the methods used to measure the jet energy scale and to determine the corresponding uncertainty. This is the leading uncertainty for the measurement of the inclusive jet cross section. Sections VI, VII, VIII, IX, X, and XI describe the jet triggers, event and jet selection criteria, determination of the jet p_T resolution and the unfolding method. In Secs. XII, XIII, and XIV, we describe our results and compare them with predictions using recent PDF parameterizations.

II. DETECTOR

In this section, we briefly describe the Run II D0 detector [15] and the main components used in the measurement of the inclusive jet cross section.

A. Calorimeter

The calorimeter and the tracking detectors, used to measure the position of the interaction point, are the most important detector components used to measure the jet p_T. An accurate and stable energy response is required for reliable measurements of the cross section for jet production. The calorimeter consists of the following subdetectors: the uranium/liquid argon calorimeter divided into a central (CC) and two end (EC) sections, the plastic scintillator intercryostat detector (ICD), and the massless gap (MG) detectors. Both the CC and ECs are segmented longitudinally into electromagnetic (EM), fine hadronic (HAD), and coarse hadronic (CH) sections. A schematic view of the calorimeter showing its projective tower geometry as a function of pseudorapidity $\eta = -\ln\tan(\theta/2)$,

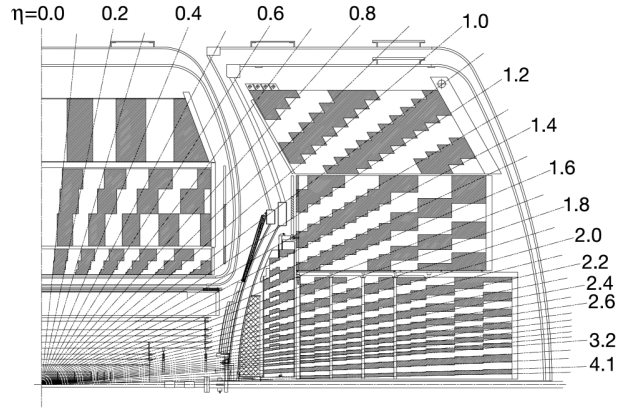

FIG. 3. Side view of a quadrant of the D0 calorimeters (CC, EC, and ICR) showing the transverse and longitudinal segmentation [15]. The shading pattern indicates the cells for signal readout. The lines indicate the pseudorapidity intervals defined from the center of the detector. The CC covers the region $|\eta| < 1.2$ and the EC extends the coverage up to $|\eta| \sim 4.2$. The intercryostat detector is visible as a thin dark shaded tile between the cryostats, within $1.1 < |\eta| < 1.4$, and the massless gap detectors are inside the cryostats, within $0.8 < |\eta| < 1.2$ (in the CC) and $1.0 < |\eta| < 1.3$ (in the EC).

where θ is the polar angle from the beam line, is given in Fig. 3. The choice of binning in the inclusive jet cross section measurement closely follows the structure of the calorimeter: $|\eta| < 0.8$ is well contained within the CC, $1.6 < |\eta| < 2.4$ within the EC, whereas the more challenging intercryostat region (ICR) $0.8 < |\eta| < 1.6$ has energy sharing between the four subdetectors.

1. Central and end calorimeters

The CC covers detector pseudorapidity $|\eta| < 1.2$, and the two ECs extend the range up to $|\eta| = 4.2$. Both the electromagnetic and fine hadronic calorimeters are sampling calorimeters with an active medium of liquid argon and absorber plates of nearly pure depleted uranium. Incoming particles traversing the uranium absorber plates initiate showers of secondary particles that ionize the argon in the gaps between the absorber plates. A high-voltage electric field collects the free electrons on resistively coated copper pads that act as signal boards [15,16]. The outer part of the calorimeter, the coarse hadronic section, uses copper in the CC and stainless steel in the EC for the absorber plates. The calorimeter is transversely segmented into cells in pseudorapidity and azimuthal angle of 0.1×0.1 (and 0.05×0.05 in the third layer of the EM calorimeter) for $|\eta| < 3.2$ to allow for more precise location of EM shower centroids. At $|\eta| > 3.2$, the cell size grows to 0.2 or more for both η and the azimuthal angle ϕ. These high pseudorapidities are not used for the jet cross section measurements since the jet triggers are limited to $|\eta| < 3.2$. The total depth of the EM calorimeter is about 20 electromagnetic radiation lengths, and the combined thickness of the electromagnetic and hadronic calorimeters is about 7 nuclear interaction lengths [16].

A typical calorimeter cell consists of an absorber plate and a liquid argon gap. The metal plate is grounded, while the resistive plate of the signal board located in the liquid argon gap is kept at a high voltage of ~2.0 kV. The drift time of the electrons across the typical 2.3 mm gap is 450 ns, longer than the separation between two subsequent Tevatron bunch crossings of 396 ns. To minimize the effect of pileup from interactions from different bunch crossings, only two-thirds of the charge collected is used in the shaper circuits and then provided to baseline subtraction boards. To remove the baseline, the signal corresponding to a sampling occurring 396 ns earlier (the time between two bunch crossings) is subtracted. Only cells with a signal at least 2.5 times the standard deviation of the electronic noise after baseline subtraction are kept in nominal conditions of data taking. This defines the online zero-suppression mode of the calorimeter.

2. Intercryostat detector and massless gaps

The regions between the CC and the ECs are instrumented with the intercryostat detector and massless gaps. The ICD and MG detectors provide energy measurement for the otherwise poorly instrumented regions located at roughly $0.8 < |\eta| < 1.4$, where the depth of the passive material coming from cryostat walls, stiffening rings and cables varies rapidly with rapidity. The ICD relies on photomultipliers to record the signals from plates of scintillating plastic and covers the region $1.1 < |\eta| < 1.4$. The signal from the ICD is stretched in time to match that of the EM calorimeter and augments the EM calorimetry that is absent in the region $1.2 < |\eta| < 1.35$. The ICD is supplemented by the MG detectors that are placed inside the cryostat walls in the CC and the ECs from $0.8 < |\eta| < 1.2$ and $1.0 < |\eta| < 1.3$, respectively. Unlike typical calorimeter cells, the massless gap detectors do not have absorber plates, but they sample the showers that develop in the cryostat walls, calorimeter support structures, and other calorimeter cells.

In addition to the CC, ECs, and ICD, preshower detectors are located in the central and forward regions, but they are not used in this analysis.

B. Tracking detectors

The tracking detectors are not used directly in jet reconstruction since the jet-finding algorithms in D0 use only energy deposits in the calorimeter towers. However, the tracking detectors are used to reconstruct the position of the primary vertex of the $p\bar{p}$ interaction, which is necessary to precisely measure the jet rapidity and transverse momentum. The position of the primary vertex is typically distributed as a 20 cm-wide Gaussian distribution along the beam line direction around the nominal interaction point of $(x, y, z) = (0, 0, 0)$ located in the center of the detector. In

the detector description and data analysis, we use a right-handed coordinate system in which the z-axis is along the proton direction and the y-axis is upward. The inner tracking system, consisting of the silicon microstrip tracker, provides a 35 μm vertex resolution along the beam line and 15 μm resolution in the $r - \phi$ plane for tracks with a minimum p_T of 10 GeV at $\eta = 0$. The outer tracking system, consisting of the central fiber tracker, uses scintillating fiber technology to complement the silicon tracker. Both detectors are located in the 2 T magnetic field of the superconducting solenoidal magnet to allow measurements of the momentum of charged particles.

C. Muon detector

The muon detector is composed of a combination of proportional drift tubes in the central region ($|\eta| \lesssim 1.0$), and smaller, faster mini-drift tubes in the forward region ($1.0 \leq |\eta| \leq 2.0$). Both are separated in three layers (A, B, C). Toroidal magnets are located between the A and B layers of the muon detector in the central and forward regions to allow reconstruction of the muon momentum. The muon system is not used directly in our analysis (we do not correct for muons in jets), but very high energy jets can leak outside the calorimeter and show some hits in the A layer. We do not include these hits in jet reconstruction, but instead correct the jet cross sections for asymmetries introduced in the jet energy resolution (described in Sec IX C).

D. Luminosity detector

The luminosity monitor (LM) is constructed of scintillating tiles on both sides of the interaction point that detect the particles coming from inelastic collisions. The luminosity $\mathcal{L}$ is determined from the average number of observed interactions $\bar{N}_{\mathrm{LM}}$ using the formula

$$\mathcal{L} = \frac{f\bar{N}_{\mathrm{LM}}}{\sigma_{\mathrm{LM}}}, \tag{1}$$

where f is the $p\bar{p}$ bunch crossing frequency, and σ_{LM} is the effective cross section for inelastic collisions measured by the LM that takes into account event losses due to inefficiencies and geometric acceptance [10]. In practice, $\bar{N}_{\mathrm{LM}}$ is calculated by inverting the expression for the Poisson probability of observing zero LM hits in either of the two arrays

$$P(0) = \mathrm{e}^{-\sigma_{\mathrm{LM}}\mathcal{L}/f} \times (2\mathrm{e}^{-\sigma_{\mathrm{SS}}\mathcal{L}/(2f)} - \mathrm{e}^{-\sigma_{\mathrm{SS}}\mathcal{L}/f}). \tag{2}$$

The right-most term of Eq. (2) accounts for the possibility of producing double-sided LM hits from a combination of single-sided (SS) LM hits, where σ_{SS} is the effective cross section for only one of the arrays to show hits. The uncertainty on the luminosity determination is estimated to be 6.1% [10]. This uncertainty is dominated by the 5.4% uncertainty coming from the determination of σ_{LM}, roughly half of which is due to acceptance and efficiency of the LM detectors with the remainder due to the uncertainty in the total inelastic cross section at 1.96 TeV described in [10,17].

III. JET RECONSTRUCTION

Jets are reconstructed using the Run II midpoint cone algorithm [18], which is an iterative cone algorithm that considers energy deposits as four-vectors to construct the jet four-momentum. The same algorithm is used with different inputs in data and Monte Carlo (MC). It is used to build jets from energy deposits in the calorimeter in data or in fully simulated MC events, out of stable particles in simulation, and out of partons produced either in a parton shower simulation or from a next-to-leading order theoretical calculation.

In data and in MC events processed through a simulation of the response of the D0 detector, the first step is to define the seeds for jet reconstruction. Pseudoprojective towers, as illustrated in Fig. 3, are built by adding the 4-momenta of the calorimeter cells. The 4-momentum associated with the energy deposit in each cell of the calorimeter is computed using the direction defined by the reconstructed $p\bar{p}$ interaction vertex and the center of the cell and assuming $E = |p|$. All non-zero-suppressed cells are used in jet reconstruction. Calorimeter towers are ordered in decreasing transverse momentum and are used as seeds to form preclusters using a simple cone algorithm of radius 0.3 in the (η, ϕ) plane, starting with the tower having the highest p_T and then descending the list until no towers remain above a minimum threshold of $p_T > 500$ MeV. All towers added to a precluster are removed from the list, avoiding overlaps between preclusters. Preclusters with $p_T > 1$ GeV are used as seeds for the jet-clustering algorithm. The goal of preclustering in data is to reduce the number of seeds and the computing time to reconstruct jets. As verified by MC studies [18], the low value of the p_T threshold on the jet seeds ensures that there are no significant variations in the jet observables for the p_T range considered in this measurement ($p_T > 50$ GeV).

The seeds—preclusters in data and in MC events processed through a simulation of the response of the D0 detector, or stable particles in MC, or partons from NLO calculation—are used as center points for proto-jets. All calorimeter towers, particles, or partons within $\Delta R = \sqrt{(\Delta y)^2 + (\Delta\phi)^2} \leq R_{\mathrm{cone}}$, where $R_{\mathrm{cone}} = 0.7$, are added to the proto-jet. The four-momentum of the proto-jet is the sum of the four-momenta of all included calorimeter towers, particles, or partons. The direction of the resulting four-vector is used as the center point for a new cone. When the proto-jet four-momentum does not coincide with the cone axis, the procedure is repeated using the new axis as the center point until a stable solution is found. The maximum number of iterations is 50 and the solution

is considered to be stable if the difference in ΔR between two iterations is smaller than 0.001. In the rare cases of bistable solutions the last iteration is retained. Any proto-jets falling below a threshold, $p_{T,\mathrm{jet}} < p_{T,\mathrm{min}}$, with $p_{T,\mathrm{min}} = 3$ GeV, are discarded.

The presence of a threshold requirement on the cluster seeds introduces a dependency on infrared and collinear radiation. In order to reduce the sensitivity to soft radiation, p_T-weighted midpoints between pairs of proto-jets are used as additional seeds if the distance between pairs, ΔR in the (y, ϕ) plane to the proto-jet, is between 0.7 and 1.4. The list of stable proto-jets obtained from this procedure may contain many overlapping and identical jet candidates. To resolve these ambiguities the proto-jets are sorted in order of decreasing p_T and processed through a split-and-merge procedure to remove overlaps. If two proto-jets have overlapping cones, they are merged if the overlap region contains more than 50% of the transverse momentum of the lower p_T jet. Otherwise, the jets are split with calorimeter cells or particles in the overlap region being assigned to the nearest jet in (y, ϕ). In both cases, the jet four-momenta are recomputed after this reassignment. In case of multiple overlaps, the algorithm always starts with the highest p_T proto-jet to redistribute the shared towers. As mentioned above, the jet four-momentum is computed as the sum of the four-momenta of the (massless) calorimeter energy deposits included in the jet, and consequently the calorimeter jets are massive by construction if the jet cone contains cells with different locations in the (η, ϕ) plane. The variables used to characterize the jets are the jet p_T and y. The split-and-merge procedure may modify the cone axis and jet four-momentum for the final jets, and include towers outside the initial 0.7 cone.

IV. THEORETICAL PREDICTIONS

In this section, we describe how we compute the predictions of the inclusive jet cross sections that are later compared to our measurements.

A. Jet cross section at NLO

We use the program FASTNLO [19], which is based on the matrix elements implemented in NLOJET++, to calculate the inclusive cross sections to next-to-leading order precision and to evaluate the effects of the choice of proton PDFs, such as CTEQ6 or MRST2004 [20,21], in a computationally efficient manner. Perturbative QCD (PQCD) requires the specification of the renormalization scale μ_R and the factorization scale μ_F. Typical choices set both $\mu_R = \mu_F$ to the p_T of each of the individual jets, with half and twice this scale used to estimate the theoretical scale uncertainty. The uncertainty on the NLO prediction of the inclusive jet cross section due to the choice of renormalization and factorization scales is given in Fig. 4 and is about 10%–20%.

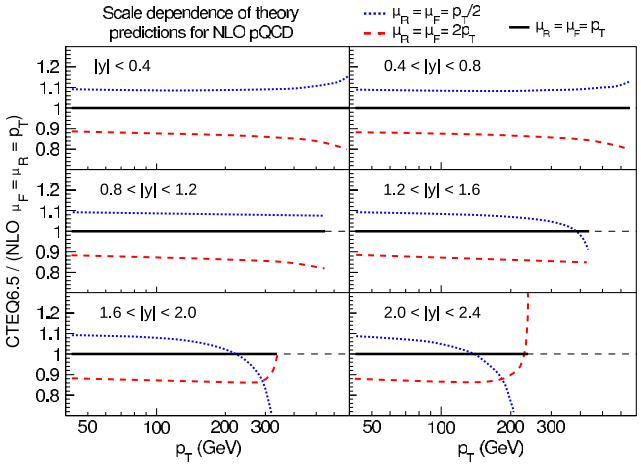

FIG. 4 (color online). (color online) Uncertainty on the inclusive jet cross section due to the choice of the renormalization and factorization scales μ_R and μ_F in the NLO QCD calculation using NLOJET++.

B. Parton distribution functions

A discussion of the different PDFs and methods to reduce their uncertainties using various measurements at the Tevatron and the LHC can be found in Ref. [2]. In this paper, we briefly describe the PDFs used in the comparison between the measurements and the theoretical predictions.

One of the PDF sets used in this analysis is provided by the CTEQ Collaboration. This most recent global fit from the CTEQ Collaboration performed prior to the measurement described in this paper, called CTEQ6.5M [20], utilizes D0 and CDF Run I measurements, as well as the most recent deep inelastic scattering (DIS) data from the HERA collider at DESY and existing fixed target DIS and Drell-Yan data. The central prediction of the CTEQ6.5M PDF is supplemented with the provision of 20 eigenvector basis PDF sets to estimate the PDF uncertainty, representing independent variations of the PDFs within the 90% C.L. of the data sets used in the fit.

Another widely used PDF parameterization is provided by the MRST Collaboration [21]. Our measurements are compared to the MRST2004 parameterization, which does not include our results. A third PDF parameterization is MSTW2008 [22] which uses our results. The differences with respect to CTEQ6.5M are mainly in the description of the gluons at high-x and are within the CTEQ6.5M uncertainty band, as shown in Fig. 5. We also note that the uncertainty on the gluon density calculated by the CTEQ6.5M parameterization is larger than 40% for $x \geq 0.5$ and squared four-momentum transfer $Q^2 = (500\ \mathrm{GeV})^2$. Comparisons between our data and NLO calculations using these and other PDF parameterizations are given in Sec. XII.

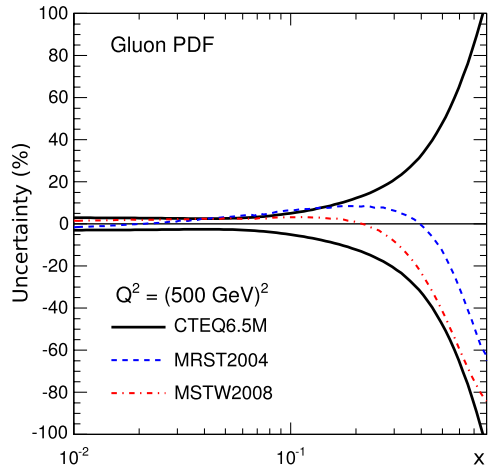

FIG. 5 (color online). (color online) Uncertainty of the CTEQ6.5M gluon PDF (solid lines) in percent compared to the differences between CTEQ6.5M and MRST2004 (dashed line), MSTW2008 (dash-dotted line) central values.

V. JET ENERGY SCALE MEASUREMENT

In this section we describe the method used to obtain the jet energy scale (JES) applied in the measurement of the inclusive jet cross section as a function of jet p_T. To compare the theoretical predictions to data, both need to be corrected to a common reference-level, chosen here to be the "particle-level jets." We correct the calorimeter jet energies to the particle level, and apply nonperturbative corrections (hadronization and underlying event) to theoretical NLO cross sections to move from the parton to the particle level. Particle jets [23] are clustered from stable particles after fragmentation, including particles from the underlying event, but excluding undetected energy from muons and neutrinos. The JES procedure provides a correction factor that translates on average the energy of jets measured in the calorimeter to the energy of the corresponding particle jets. The jet energy scale is determined from data acquired during the same running period as used in the measurement of the inclusive jet cross section.

The main effects that need to be considered when correcting jet energies from the calorimeter measurement $E_{\text{jet}}^{\text{measured}}$ to the particle level $E_{\text{jet}}^{\text{particle}}$ are the offset energy (O), calorimeter response (R), and detector showering (S). These corrections can be expressed as a simple formula

$$E_{\text{jet}}^{\text{particle}} = \frac{E_{\text{jet}}^{\text{measured}} - O}{R \cdot S}. \quad (3)$$

The offset energy O originates from electronics noise, calorimeter noise from uranium decays, residual energy from previous bunch crossings ("pile-up"), and energy from multiple $p\bar{p}$ collisions during a bunch crossing. The underlying event energy corresponding to multiple parton interactions in a single $p\bar{p}$ collision is not considered as part of the offset energy since it is included in the jet energy at the particle level. This also avoids correcting the data with model-dependent offset corrections. The calorimeter response R is the average fraction of the energy measured in the calorimeter for the particles inside the jet cone. The detector showering is the net flow of energy in and out of the jet cone due to detector effects, such as the magnetic field, scattering from passive material, and shower development in the calorimeter. The correction S is defined as the ratio of the response-corrected calorimeter jet energy, in the absence of offset, and the particle jet energy. The correction does not include the effects of real QCD emissions (S_{phys}), which arise from partons that shower outside the jet cone. We discuss each correction in turn below.

A. Determination of the offset energy

The offset energy consists of the energy in the jet that is not related to the primary $p\bar{p}$ collision (hard scatter and underlying event). The offset energy is divided into two distinct categories, noise and pileup (NP), and multiple $p\bar{p}$ interactions (MI). The noise component corresponds to the contributions of calorimeter and electronics noise, as well as the decay of the uranium nuclei in the calorimeter. The pile-up energy corresponds to the energy left in the calorimeter from previous or next collisions because of the long integration time of the calorimeter electronics. The typical value of the NP offset in a cone, $R = 0.7$, is 0.2 GeV in the CC and ECs and 0.5 GeV in the ICR for the instantaneous luminosities considered in this analysis.

The MI offset is the energy deposited by additional collisions during the bunch crossing. The value of the MI offset increases linearly with the number of additional interactions, which is characterized by the number of reconstructed $p\bar{p}$ interaction vertices in a given event. A typical value of MI is of the order of 0.5 GeV in the CC per additional interaction.

The offset energies are measured directly from data using "zero bias" and "minimum bias" data collected at a constant rate of about 0.5 Hz during data taking. The only requirement for zero bias events is coincident timing with the beam crossing; minimum bias events additionally require energy depositions above thresholds in coincidence in the two luminosity monitors, indicating that an inelastic collision took place. The offset is estimated from the average energy density in all calorimeter towers within detector rings of fixed pseudorapidity. The offset energy for a given jet cone is then calculated by summing the average offset in towers within the cone radius around the jet center. The NP offset energy is measured using zero bias data with a veto on the luminosity monitor (no interaction occurred). The MI energy for a given number N of reconstructed vertices is estimated as the difference in the energy in minimum bias events with $(N + 1)$ vertices and with a single vertex.

The offset energy for different numbers of reconstructed $p\bar{p}$ vertices is displayed in Fig. 6 and is found to depend

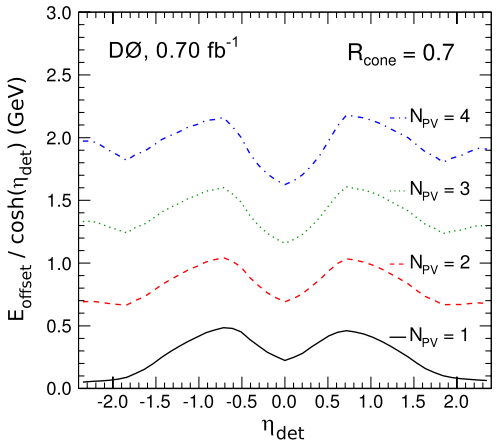

FIG. 6 (color online). (color online) Offset corrections as a function of the jet pseudorapidity in the detector (without taking into account the vertex position) for different numbers of reconstructed primary vertices N_{PV}. The special case $N_{\mathrm{PV}} = 1$ includes only the noise contribution to the offset.

linearly on the number of reconstructed vertices within a 5% uncertainty. The average vertex multiplicity in the sample used to measure the inclusive jet p_T cross section is ~1.5–2.0, hence the average offset correction to jet p_T is ~0.5 GeV in the CC and EC and ~0.7 GeV in the ICR. The uncertainties on the offset corrections are of the order of 1% of the overall energy correction at low jet p_T and are negligible for jet p_T above ~100 GeV. They are significantly smaller than the total jet energy scale uncertainties.

B. Determination of the jet energy response

The jet energy response, R, can be factorized into two parts $R = R_{\mathrm{cc}}(E) \cdot F_\eta(\eta, E)$. The R_{cc} term uses the p_T balance between the γ and the jet in γ + jet events with a high (photon) purity in the CC region to determine an absolute response correction, while the second term F_η normalizes the response of the calorimeter as a function of jet pseudorapidity.

1. Jet response in the CC

The missing transverse energy ($\not\!\!E_T$) projection fraction (MPF) method [24] is applied in γ + jet events to measure the response for jet energies in the CC region. Use of the MPF reduces the sensitivity of the measurement to showering and additional unreconstructed jets. We project the vector sum of all calorimeter tower energies transverse to the beam (including those of the photon), which equals the opposite of the $\not\!\!E_T$ in the event, onto the photon transverse momentum vector $\vec{p}_{T,\gamma}$. At the particle level, the photon is balanced against the hadronic recoil, $\vec{p}_{T,\gamma} + \vec{p}_{T,\mathrm{had}} = 0$, where $\vec{p}_{T,\gamma}$ and $\vec{p}_{T,\mathrm{had}}$ are the transverse momentum of the photon and the hadronic recoil system, respectively. The measured jet p_T will be affected by the energy response of the calorimeter causing an imbalance in the jet and photon transverse momenta, resulting in a nonzero $\not\!\!E_T$,

$$R_{\mathrm{em}} \cdot \vec{p}_{T,\gamma} + R_{\mathrm{had}} \cdot \vec{p}_{T,\mathrm{had}} = -\vec{\not\!\!E}_T, \tag{4}$$

where R_{em} and R_{had} are the electromagnetic and hadronic calorimeter responses, respectively.

The MPF method necessitates a precise energy calibration for electrons and photons. The electron energy scale is determined from data using $Z \to e^+e^-$ decays [25]. MC simulations tuned to reproduce the response for electrons in data are used to derive the response difference between photons and electrons and to constrain the response at higher energies. The leading uncertainty in this simulation is caused by limited knowledge of the number of radiation lengths of material in front of the calorimeter.

Using the corrected photon energy scale ($R_{\mathrm{em}} = 1$), R_{had} is determined after projecting all terms in Eq. (4) on the photon p_T unit vector $\hat{n}_\gamma$. In the MPF method, the jet response R_{had} is thus directly defined through the $\not\!\!E_T$

$$R_{\mathrm{had}} = 1 + \frac{\vec{\not\!\!E}_T \cdot \hat{n}_\gamma}{|\vec{p}_{T,\gamma}|}, \tag{5}$$

where we use $|\vec{p}_{T,\gamma}| = -\hat{n}_\gamma \cdot \vec{p}_{T,\mathrm{had}}$. When the jet is required to be back-to-back with the photon (difference in azimuthal angle larger than 2.9 radians) and no additional jets are allowed in events with a single $p\bar{p}$ interaction, the hadronic recoil response R_{had} can be identified with the jet response R_{jet}. The impact of the proton remnants is small on average. The jet energy response depends on the particle jet energy and the results are usually binned in jet p_T. However, the measured jet energy has poor resolution and can lead to a large bias in the measurement of the response. To avoid this resolution bias, the jet energy response is measured as a function of the estimator

$$E' = p_{T,\gamma} \cdot \cosh\eta_{\mathrm{jet}}. \tag{6}$$

E' is strongly correlated to the particle level jet energy and has a better resolution than the measured jet energy. We parameterize all corrections as a function of E' and map back to the measured jet energy $E_{\mathrm{jet}}^{\mathrm{measured}}$ on a jet-by-jet basis by inverting the equation

$$E_{\mathrm{jet}}^{\mathrm{measured}} - O = R_{\mathrm{had}}(E')S_{\mathrm{phys}}(E')E', \tag{7}$$

where O is the offset contribution, $R_{\mathrm{had}}(E')$ contains all jet energy corrections back to particle level, and $S_{\mathrm{phys}}(E') = E_{\mathrm{jet}}^{\mathrm{particle}}/E'$ accounts for energy loss from out-of-cone radiation, leading to a correction of 0.90–1.00 for jet $p_T >$ 50 GeV and $|y| < 3.0$. This is necessary because the quantity E' represents the jet energy in an exclusive 2-body final state, whereas physics showering can reduce the energy observed within a fixed jet cone. Furthermore E' is essentially insensitive to showering effects (related to the jet

cone size), because it is based on the total hadronic recoil opposite the photon. The mapping in Eq. (7) relates E' to the measured energy for jets in the calorimeter and the term $S_{\rm phys}$ varies with the cone size used for jet reconstruction. The equation is iteratively solved using Newton's method. The resulting estimate of the jet energy is observed to agree with E' to better than 2% at jet $p_T > 50$ GeV, resulting in less than 0.2% uncertainty due to parameterization of the jet response $R_{\rm had}$.

Another issue in using the MPF is related to photon identification. To have a clean γ + jet sample in data, only CC photons are used with tight selection criteria. However, in some jets a large fraction of their transverse momentum is carried by photons from π^0, η, or K_s^0 decays, which form a sample of "electromagnetic" jets ("EM-jets"). If these photons are sufficiently close together, and there is little activity around the photons, the jet can mimic an isolated single photon typical for γ + jet events. Because the cross section for dijet events is ~3–4 orders of magnitude larger than that for γ + jet events, dijets constitute a significant source of background. An artificial neural network (ANN) is trained to discriminate between photon and EM-jets [26] using input variables based on the shape of the calorimeter shower and measurements of charged particle tracks in the vicinity of the photon candidate. The distribution of the photon ANN output for the simulated photon signal and for the EM-jet background samples are fitted to the data for each E' and η bin using a maximum likelihood optimization to obtain the fractions of signal events in the data. To reduce the uncertainty in the jet energy scale due to contamination from background in the γ + jet events, the difference in the response determined from real γ + jet and dijet events, where one of the jets is misidentified as a prompt photon, is estimated using MC and applied as a correction based on the estimated purity of the selected photons in data. The jet energy response after all corrections as a function of E' in the CC is given in Fig. 7. The main uncertainty is due to the uncertainty on the photon energy scale, which is on the order of 0.5% at $E' \approx 20$ GeV and 0.8% at $E' \approx 500$ GeV. The choice of fragmentation model used in PYTHIA [27] is an additional source of systematic uncertainty on the photon purity [28].

The statistics of the γ + jets sample limits the direct response measurements in the CC to $E' < 350$ GeV. The measured energy response in this region must be extrapolated to the highest jet energies at ≈ 600 GeV. To avoid a statistical uncertainty of more than 2% for high-p_T jets in the CC, MC models are used to constrain the response. For this purpose, the measurement of the response in γ + jet events in the MC is rescaled to the measurement in data by modifying the response of the calorimeter for single pions in MC. This rescaling is performed by accounting separately for the energy deposited in the calorimeter by each generated particle and then modifying this energy by the measured single-pion response in data and finally summing the energies in each calorimeter cell. This provides a tuned MC prediction that is used to extend available measurements and to evaluate methods used in this analysis. Figure 7 shows the measured response for jets in data compared to the rescaled MC prediction and to a quadratic fit in logE'. The dominant uncertainty, arising from the fragmentation model for the high E' extrapolation, is estimated using the differences between the PYTHIA and HERWIG [29] generators after turning off the underlying event modeling. This leads to a systematic uncertainty of about 0.8% at $E' = 600$ GeV. The systematic uncertainties related to PDFs (especially due to the uncertainty on the gluon fraction in the proton) are about 0.2%.

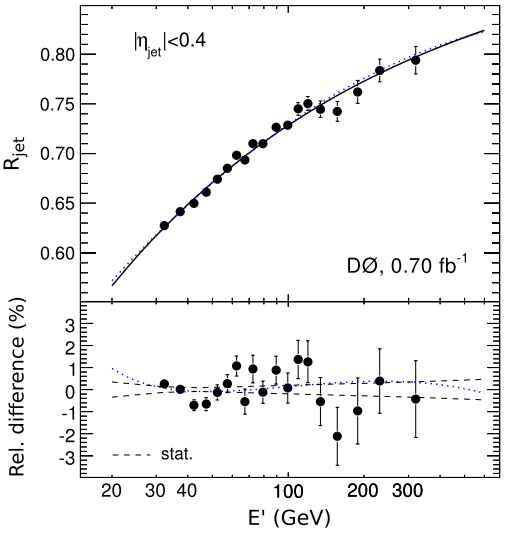

FIG. 7 (color online). (color online) Extrapolation of the jet energy response in the CC at high E' using the rescaled MC (see the main text) and a fit to the MC points. The dotted line shows a simple quadratic-logarithmic fit to data for comparison with the tuned MC results displayed by the solid line. We also display in the bottom panel the relative difference between both curves and the statistical uncertainty on the fit to the rescaled MC in dashed lines.

The total uncertainty on the jet p_T response as a function of E' is given in Fig. 8. The dominant uncertainty comes from the photon energy scale. The uncertainty due to photon identification is related to the uncertainty on the sample purity and contributes mainly at E' energies below 50 GeV.

2. Pseudorapidity dependent corrections

The purpose of the η-dependent corrections is to equalize the jet response everywhere as a function of pseudorapidity in the calorimeter after the jets are corrected for offset effects. The D0 calorimeter is intercalibrated at the cell level as a function of the azimuthal angle ϕ by equalizing the response of the calorimeter in dedicated ϕ-symmetric data samples. This yields a jet response

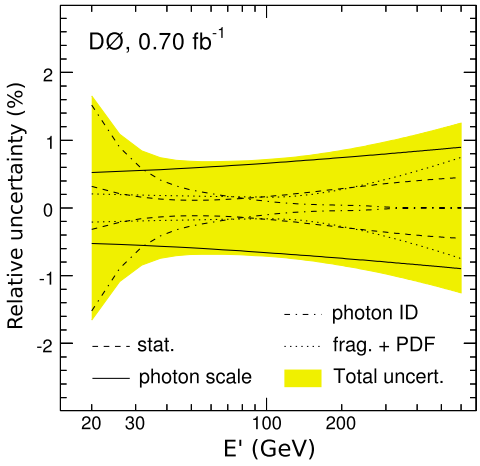

FIG. 8 (color online). (color online) Different sources of uncertainty on the jet p_T response in the CC: photon energy scale, photon identification, fragmentation, and PDF.

that is independent of ϕ, so only the η dependence of the response needs to be corrected. The η dependence of the response is mostly due to the changing calorimeter detector elements, especially in the ICR, different amounts of passive material and the varying angle of incidence with jet η. The η-dependent corrections $F_\eta(E, \eta)$ normalize the response at forward pseudorapidities to that measured in the CC (R_{CC}). This leads to the definition

$$F_\eta(E, \eta) \equiv R(E, \eta)/R_{\mathrm{CC}}(E), \tag{8}$$

where $R(E, \eta)$ is the response of the detector for a jet of energy E, located at detector pseudorapidity η. We use both dijet and γ + jet samples to determine F_η. The dijet sample provides high statistics and high reach in jet energy for the forward region. One of the jets is required to be central and the response measurement is binned in terms of the p_T of the central jet [using the dijet E', defined as in Eq. (6) where the photon is replaced by the central jet] after correcting for the offset and calorimeter response. This binning leads to a resolution bias, which is later corrected.

The η-dependence of the response, F_η, is fitted using a quadratic-logarithmic function of E'

$$F_\eta(E', \eta) = \frac{p_0(\eta) + p_1(\eta)\ln(E') + p_2(\eta)\ln^2(E')}{R_{\mathrm{CC}}(E')}, \tag{9}$$

where the p_i are fitted as a function of detector η. The F_η and p_i's are given in Figs. 9(a)–9(c). As an example of the data used in this fit, we give in Fig. 10 the η-dependent corrections for two bins in η for the dijet and γ + jet samples. Although the correction factors depend on the sample (γ + jet, dijets), we can remove this dependency

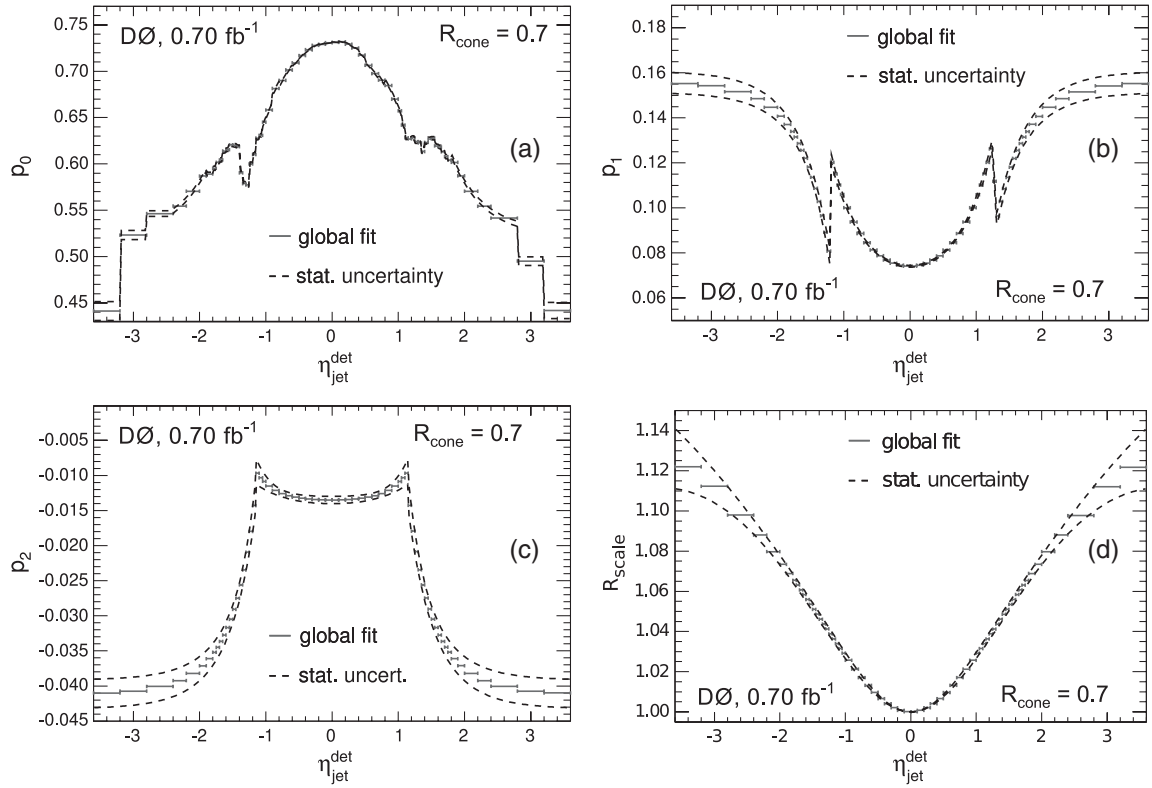

FIG. 9. The (a-c) parameters of the η-dependent correction and (d) the η-dependent scaling factor applied to the dijet samples. The sharp features are due to changes in the detector structure, moving from the central to forward calorimeters.

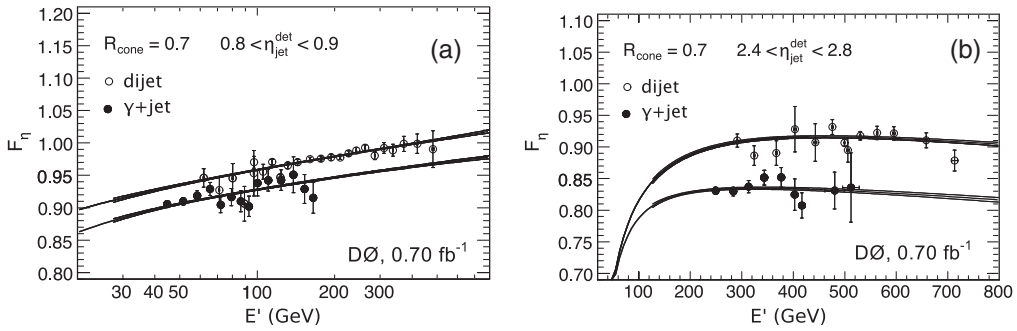

FIG. 10. Fits of F_η in γ + jet and dijet data for two different regions in η as a function of E'. The central fit values and the uncertainty band are displayed on the figure.

by scaling the dijet correction in the overlap region between the CC and the EC by an energy-independent factor R_{scale}:

$$R_{\text{scale}}(\eta) = 1 + q_1 \ln[\cosh(\eta)] + q_2 \ln^2[\cosh(\eta)], \qquad (10)$$

where q_1 and q_2 are two parameters fitted to data and the result is given in Fig. 9(d). This functional form is motivated by phenomenological studies of the difference in the jet responses measured in γ + jet and dijet samples, as discussed in the next section.

The jet p_T resolution is worse than the γ p_T resolution. Because of the steeply falling inclusive jet cross section, more jets migrate into a given p_T bin from lower p_T than from higher p_T, giving rise to a p_T bias compared to the particle level. The effect of this resolution bias is taken into account in the final measurement of the jet p_T response versus η using the CC jet p_T resolutions obtained from dijet events as described in Sec. IX. In particular, the jet transverse momenta in dijet events in the CC are *a priori* perfectly balanced on average by definition $[F_\eta(E', \eta = 0) = R_{\text{scale}}(\eta = 0) = 1]$, which provides a strong constraint for the bias correction.

With the application of the dijet-specific scale factor and resolution bias corrections we obtain systematic uncertainties in the η-dependent corrections that are less than 1% for $|\eta| < 2.8$ as illustrated in Fig. 11. The leading systematic uncertainty in most regions is from the average residuals of the fits for F_η and is estimated to be 0.5% for $0.4 < |y| < 2.4$ and constant versus energy. This residual accounts for the scatter of the data points around the central fit and covers possible variation in the shape of the fit function. The uncertainty due to the resolution bias correction is of the order of 0.5% at $|\eta| = 2.0$ and reduces to zero at $\eta = 0$. Direct measurements in data are available up to $p_T \sim 350(150)$ GeV for $0.4 < |\eta_{\text{jet}^{\text{det}}}| < 0.8 (2.0 < |\eta_{\text{jet}^{\text{det}}}| < 2.4)$, which allows a precise extrapolation to higher p_T, given the logarithmic dependence of response as a function of energy. The validity the extrapolation can be tested in MC, by performing the fit procedure using samples of γ + jet and dijet events in a similar energy range as available in data, and comparing the predicted relative response correction for dijets at high p_T with the direct measurements. No evidence of a systematic effect is observed and a maximum systematic uncertainty of 1% is assigned for $E' \sim 800$ GeV, decreasing linearly to zero at the typical E' where sufficiently precise measurements are available in data in each $|\eta_{\text{jet}^{\text{det}}}|$ bin. This covers the expected variation of the response throughout the extrapolation regions.

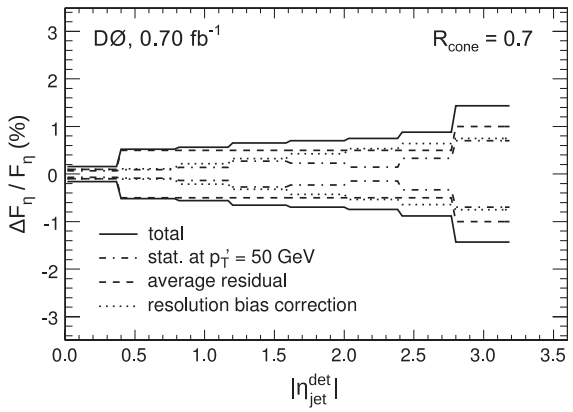

FIG. 11. Relative uncertainties on the η-dependent corrections as a function of jet detector rapidity.

3. Dijet-specific response

The methods presented so far allow for a precise measurement of the MPF response in the CC for the γ + jet sample. However, the response for dijet and γ + jet events is different. Figure 12 displays response for the quark and gluon-initiated jets measured in MC simulations after rescaling the single-pion response to data. The gluon-initiated jets have a lower response than quark-initiated jets because they have on average higher particle multiplicity with softer particles. The soft particles lead to a lower jet response due to the falling single-pion response at low energy. Figure 13 displays the fraction of gluon-initiated jets in MC for γ + jet and dijet events. The γ + jet jet energy scale cannot be used directly for the measurement of the inclusive jet cross section, because this

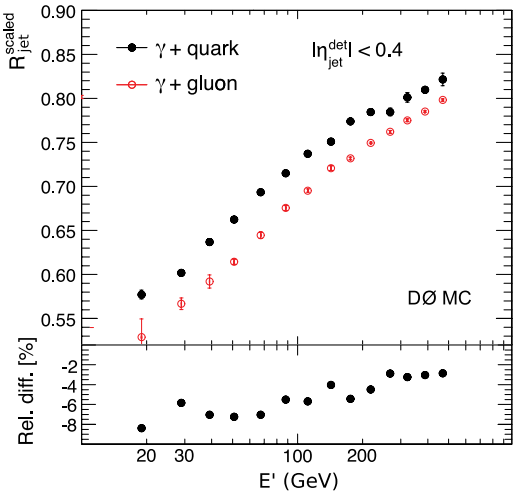

FIG. 12 (color online). (color online) Quark- and gluon-initiated jet responses and their relative differences for CC jets as a function of E'.

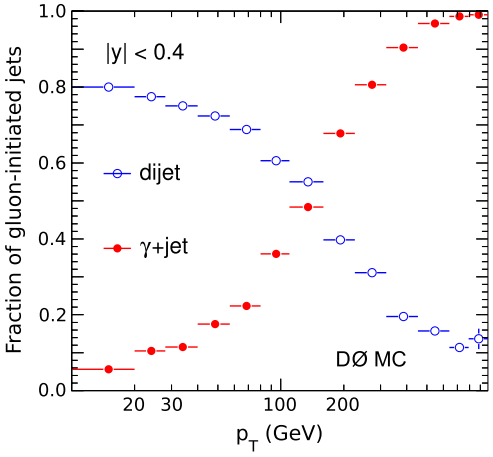

FIG. 13 (color online). (color online) Fraction of gluon-initiated jets in γ + jet and dijet events in the CC.

sample is strongly dominated by dijets. This effect also explains the differences we observe in Fig. 10 for the η-dependent corrections in γ + jet and dijet samples. The difference observed in F_η versus E' at fixed η is due to the different amounts of quark and gluon jets in the samples. The gluon versus quark fractions depend primarily on energy (not p_T or η) which leads to a correction factor dependent on $\cosh(\eta)$. Once this difference is taken into account, it is possible to combine both samples to fit F_η.

To calculate the relative difference in response between γ + jet and dijet samples in the CC, we first scale the single-pion response in MC to reproduce the measured jet response in the γ + jet data. The measurement from data of the absolute jet response in γ + jet events in the CC is then scaled to its dijet equivalent. The dijet η-dependent corrections are obtained from a global fit to γ + jet and dijet data, which accounts for the sample-dependent response.

The differences between the dijet response used in this analysis and the γ + jet response used in most other analyses are contained in the η-dependent scale factor F_η and the ratio of the responses $R_{\mathrm{dijet}/\gamma+\mathrm{jet}}$ at $\eta = 0$

$$R_{\mathrm{dijet}}(E', \eta) = R_{\mathrm{dijet}/\gamma+\mathrm{jet}}(E') \cdot F_\eta(\eta) \cdot R_{\gamma+\mathrm{jet}}(E', \eta). \quad (11)$$

The ratio between the dijet and γ + jet responses $R_{\mathrm{dijet}/\gamma+\mathrm{jet}}$ is in principle given by the information presented in Figs. 12 and 13 and can be expressed using the responses for the gluon- and quark-jets [30] (R_{gluon} and R_{quark}) and the fractions of gluon-jets in the dijet and γ + jet samples ($f_{\mathrm{gluon}}^{\mathrm{dijet}}$ and $f_{\mathrm{gluon}}^{\gamma+\mathrm{jet}}$)

$$R_{\mathrm{dijet}/\gamma+\mathrm{jet}} = \frac{(R_{\mathrm{gluon}} f_{\mathrm{gluon}}^{\mathrm{dijet}} + R_{\mathrm{quark}}(1 - f_{\mathrm{gluon}}^{\mathrm{dijet}}))}{(R_{\mathrm{gluon}} f_{\mathrm{gluon}}^{\gamma+\mathrm{jet}} + R_{\mathrm{quark}}(1 - f_{\mathrm{gluon}}^{\gamma+\mathrm{jet}}))}. \quad (12)$$

In this analysis the ratio $R_{\mathrm{dijet}/\gamma+\mathrm{jet}}$ is determined using responses measured in the tuned MC. Associated effects due to variations in PDFs and fragmentation models are included in uncertainties assigned to the MPF response.

C. Detector showering correction

Jets are extended objects and deposit their energy over a wide area in the calorimeter. When the cone algorithm is used, some of this energy is deposited outside the jet cone due to interactions with the magnetic field and passive material. This is called detector showering and needs to be taken into account in the jet energy scale determination. In addition, part of the energy of the incident parton is lost outside the jet cone because of hadronization and the finite size of the jet cone. This is called physics showering and is considered in mapping the energy scale correction, determined in terms of E', to the measured jet energies as described in Sec. V B 1.

The determination of the detector showering corrections requires a good understanding of the transverse jet energy profile. In a dedicated study, the cell-level information from MC is kept to generate energy density profiles as a function of the distance $\Delta R = \sqrt{(y_{\mathrm{particle}} - y_{\mathrm{jet}})^2 + (\phi_{\mathrm{particle}} - \phi_{\mathrm{jet}})^2}$ between the particle and the jet axis for particles originating from inside the particle jet, from outside the jet, and from offset due, in particular, to pile up or additional interactions in one bunch crossing. The sum of these profiles is fitted to the measured energy profile in data to account for possible response differences between data and MC. The energy profiles are created by summing the energy in the cells at a given radius from the cone axis. The profiles are calculated for back-to-back γ + jet events and show the jet core at ΔR around 0 and the photon contribution at $\Delta R \approx \pi$. The energy density in the range $R_{\mathrm{cone}} < \Delta R < \pi$ is primarily

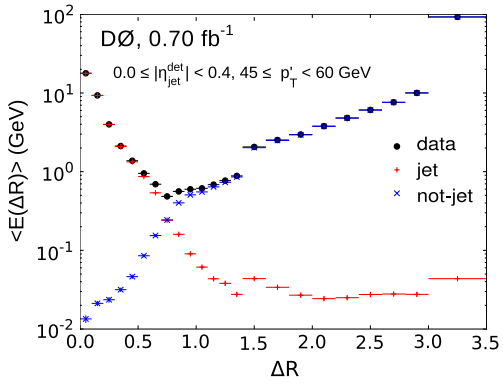

FIG. 14 (color online). (color online) Jet energy profiles as a function of distance from the jet axis ΔR for MC and data used to compute showering corrections. The data are corrected for offset energy from noise and additional $p\bar{p}$ collisions and are compared to MC jets without offset (jet) and contributions from the underlying event (not-jet). We note the good agreement between data and the sum of energy contributions from inside and outside the jet in MC.

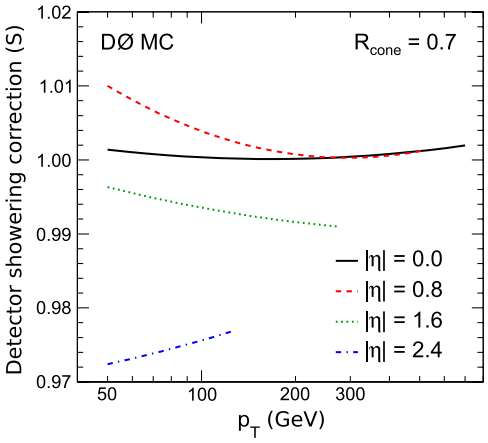

FIG. 15 (color online). (color online) Jet showering corrections shown as a function of jet p_T for different regions of jet pseudorapidity.

offset energy. Figure 14 shows an example of the showering profiles in MC without any zero bias event overlay (i.e. with only the underlying event and no offset). It gives the average energy in a given rapidity and transverse energy bin coming from inside and outside the jet as a function of the distance ΔR in rapidity and azimuthal angle from the center of the jet. The MC describes the data when both the energies inside and outside the jet are considered.

The estimate of the showering correction $\hat{S}$ for γ + jet events in MC and data is obtained by comparing the energy deposited by all particles inside the calorimeter jet cone $\sum_{\Delta R=0}^{R_{\rm cone}} E_{\rm in} + \sum_{\Delta R=0}^{R_{\rm cone}} E_{\rm out}$ originating from inside or outside the particle jet to that from the original particle jet $\sum_{\Delta R=0}^{\infty} E_{\rm in}$ using the fit-weighted templates

$$\hat{S} = \frac{\sum_{\Delta R=0}^{R_{\rm cone}} E_{\rm in} + \sum_{\Delta R=0}^{R_{\rm cone}} E_{\rm out}}{\sum_{\Delta R=0}^{\infty} E_{\rm in}}, \tag{13}$$

where $E_{\rm in}$ and $E_{\rm out}$ are the energies coming from inside and outside the jet. To take into account any potential bias in the method, the final value of the showering correction in data is computed as

$$S_{\rm data} = \hat{S}_{\rm data} \cdot \frac{S_{\rm MC}^{\rm true}}{\hat{S}_{\rm MC}}, \tag{14}$$

where the true showering $S_{\rm MC}^{\rm true}$ is directly available in MC by measuring the contribution of each generated particle to the energy inside or outside the jet cone. This bias correction amounts to less than 0.3%.

While the showering templates are measured in energy, the applicable quantity for the cross section measurement is jet p_T. When mapping the showering templates to p_T the deposits in rapidity are weighted by $\cosh(y_0)/\cosh(y_i)$, where y_0 is the cone axis and y_i is the rapidity of the energy deposit. As a result of this weighting, the effects of showering in p_T are generally suppressed relative to energy showering. This can also tilt the jet toward $y = 0$ and cause a net increase in the jet p_T, leading to $S_{\rm data} > 1$. The differences between energy and p_T showering can be up to (1%–2%) over the kinematic region of the cross section measurements.

The last step of the showering correction is to make the transition from γ + jet to dijet events. This remaining correction is computed directly using the differences in showering in γ + jet and dijet MC. The final jet p_T showering corrections are given in Fig. 15.

The uncertainties on the showering correction are less than 1% of the overall correction factor at $p_T > 50$ GeV. The main sources of uncertainty come from the difference between data and MC in the single-pion response at low p_T, the quality of the fits of MC templates to data, and the description of the underlying event determined by varying PYTHIA tunes for Tevatron data at higher p_T.

D. Potential biases in the method

1. Topology bias of the MPF method

The MPF method balances a photon or a central jet against the full remaining hadronic recoil, but the measured MPF response is interpreted as the response of the probe jet. The precision of this interpretation may be biased because the hadronic recoil includes particles not related to the probe jet, for example, particles coming from soft gluon radiation. These additional particles are generally softer than those in the core of the jet and are expected to lower the response of the recoil with respect to that of the jet core.

In the case of the energy measurement, an additional bias is caused by the systematic mismeasurement of the jet rapidity, because the MPF method is inherently based on balancing p_T. As we will see in the following, the rapidity

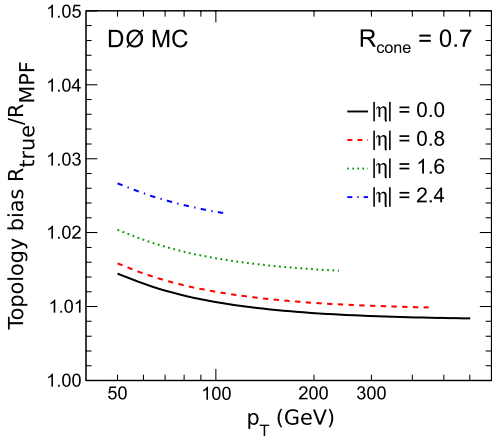

FIG. 16 (color online). (color online) Topology bias in the MPF method for jet p_T response.

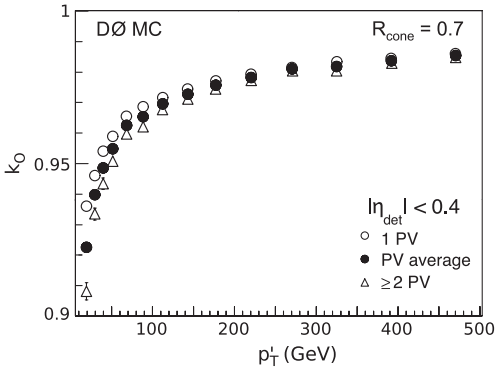

FIG. 17. Bias in the measurement of jet energy, k_O, due to zero-suppression effects on the offset correction, shown as a function of p'_T for central jets and different number of reconstructed vertices.

bias is particularly large in the ICR, where the absolute rapidity is systematically underestimated and causes a corresponding increase in the MPF response: the same calorimeter energy now corresponds to higher p_T. Since the bias versus energy has a nontrivial rapidity dependence and the cross section measurement is performed as a function of p_T, we derive and apply topology bias corrections as a function of jet p_T.

The bias of the MPF response is determined in tuned MC by comparing the response measured by the MPF method to the true response, defined as the ratio of jet energy measured at detector and particle levels [31]. The result for the p_T response is shown in Fig. 16. This bias is about 1%–2.5% for the different rapidity regions with little p_T dependence ($< 0.5\%$) for $p_T > 50$ GeV. The MPF response bias is quite small since the method is based on the p_T balance and the cone size of $R = 0.7$ is large enough to contain most of the hadronic recoil in the absence of additional soft nonreconstructed jets. The bias is significantly larger, 2%–4%, for $R = 0.5$ jet cones. The systematic uncertainty on the MPF method bias can depend on fragmentation models and is computed as the difference between the γ + jet and dijet samples and found to be of the order of 0.1%.

2. Zero-suppression bias

An offline zero-suppression further suppresses the energies of calorimeter cells in order to reduce the amount of noise, in particular, in the coarse hadronic section, that can contribute to jet energies. The algorithm used for this zero-suppression retains calorimeter cells if their energy exceeds the average baseline noise by 4σ, where σ represents the measured standard deviation of the noise for a given cell. Neighboring cells are also retained if their energy exceeds a threshold of 2.5σ.

The zero-suppression algorithm produces a small positive noise offset contribution because of the asymmetric zero-suppression (negative energies are never kept). For cells with high enough real energy deposits, as within the jet core, the zero-suppression produces no net offset, and positive and negative noise offset contributions are expected to cancel. Conversely, the energies measured for particles incident on the calorimeter, including those from uranium decay, are reduced by the zero-suppression when cells are below threshold. Therefore the average offset within a jet is different from the offset outside of a jet which we measure using zero bias and minimum bias events.

The offset measured inside the jet environment is increased compared to the average energy density measured outside jets in zero bias and minimum bias events. The correction factor for the offset inside a jet, k_O, is defined as

$$k_O = \frac{\langle E_{\text{jet}}^{\text{measured}}(\text{no ZB overlay})\rangle}{\langle E_{\text{jet}}^{\text{measured}}(\text{ZB overlay}) - O^{\text{measured}}\rangle}, \quad (15)$$

where $E_{\text{jet}}^{\text{measured}}$ is the energy of a reconstructed jet and O^{measured} is the measured offset correction described in Sec. VA. The same MC events are reconstructed with

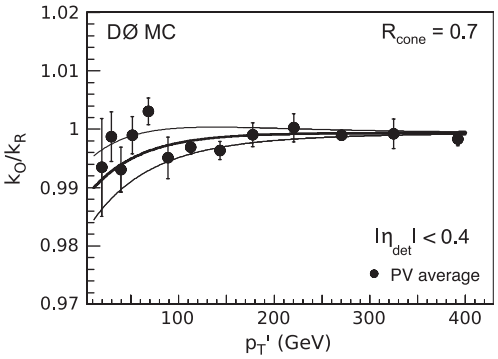

FIG. 18. Zero-suppression bias k_O/k_R in CC. The outer solid lines show the uncertainty attributed to the bias correction and the 1σ contours.

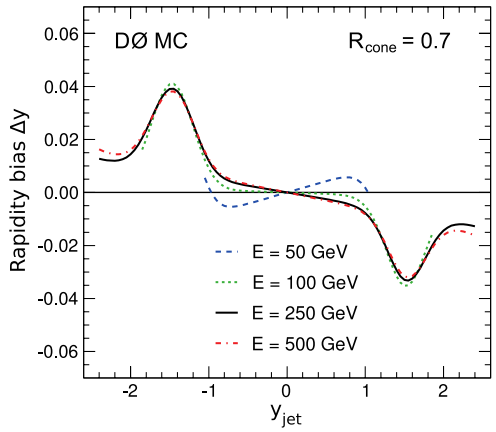

FIG. 19 (color online). (color online) Rapidity bias obtained in MC for different jet energies E. The curves cover the range $p_T > 30$ GeV and $|y_{\text{jet}}| < 2.4$.

and without zero bias event overlay (offset). The zero bias event sample was collected without any calorimeter zero-suppression so that its effect can be studied in detail. Figure 17 shows the effect of zero-suppression on the offset correction for jets in the CC. For jet $p_T' > 50$ GeV, where $p_T' = E'/\cosh \eta_{\text{jet}}$, the resulting bias on jet energy varies between 5% at low p_T' and 2% at higher p_T'.

The bias in offset is almost fully canceled by an opposite bias in the MPF response, defined as

$$k_R = \frac{\langle R_{\text{had}}(\text{no ZB overlay})\rangle}{\langle R_{\text{had}}(\text{ZB overlay})\rangle}, \tag{16}$$

because the increased offset inside the jet increases the $\not{E}_T$ in the photon direction. This artificially increases the estimated MPF response [see Eq. (5)]. Only the ratio k_O/k_R is therefore relevant for the final bias correction due to the zero-suppression bias. The combined bias is found to be less than 0.5% for jet $p_T > 50$ GeV in all rapidity bins, largely cancelling the topological bias, and approaches zero at high p_T, as shown in Fig. 18.

3. Rapidity bias

Since the inclusive jet cross section is measured in bins of rapidity, we checked for any potential bias in the reconstruction of jet rapidity using the simulation, as shown in Fig. 19. The rapidity is generally biased towards the central calorimeter, with the largest deviations observed in the ICR. This is attributed to detector effects in the ICR in addition to the jet cone algorithm itself. The absolute effect on the inclusive jet measurement is small compared to the effect of jet p_T calibration.

E. Final jet energy scale corrections and uncertainties

Figure 20 shows the jet energy scale corrections as a function of jet p_T for central and forward rapidity, and as a function of jet rapidity at low and high jet p_T. The corrections range between 1.2 and 1.8 for the kinematic range of the cross section measurement. The response correction is by far the largest one, while the showering correction starts to be noticeable at large rapidity. At high rapidity, the actual angular distance for each $\Delta\eta$ bin is small, while the radius of the showering is slightly increasing due to the

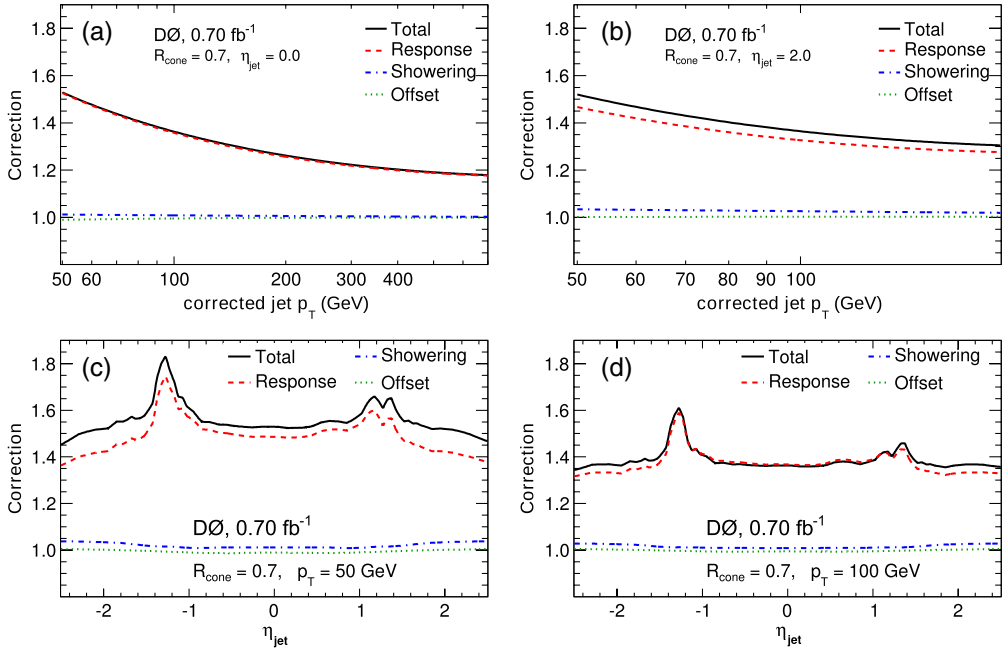

FIG. 20 (color online). (color online) Jet energy scale corrections as a function of jet p_T for (a) central and (b) forward rapidity, and as a function of jet rapidity for (c) low and (d) high jet p_T.

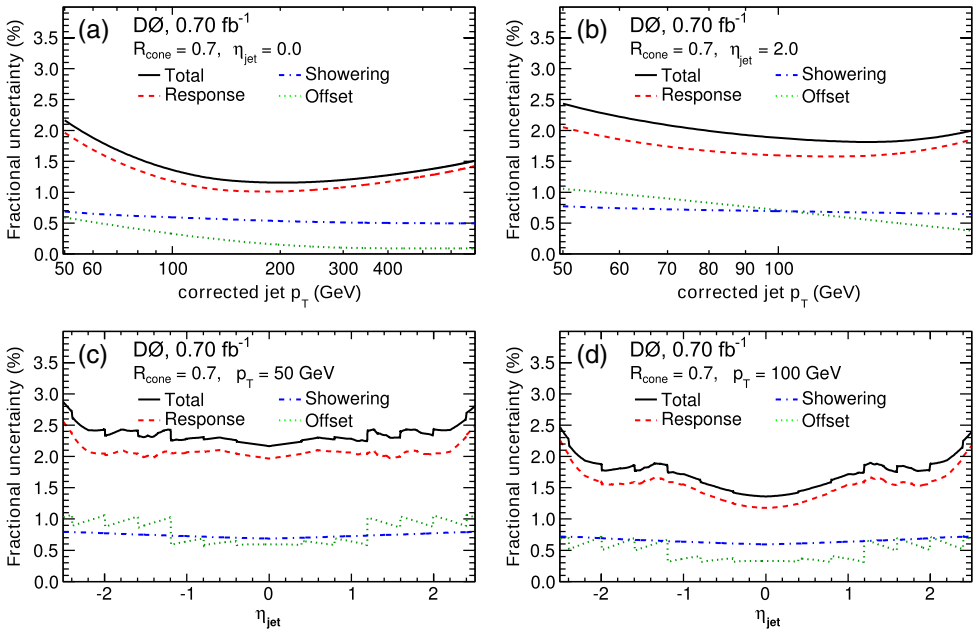

FIG. 21 (color online). (color online) Jet energy scale uncertainties as a function of jet p_T for (a) central and (b) forward rapidity, and as a function of jet pseudorapidity for (c) low and (d) high jet p_T.

increasing energy of the jet at fixed p_T as one goes forward. The total correction is computed using Eq. (3). The combined effects of the uncertainties associated with each component of the correction are summarized in Fig. 21 as a function of jet p_T for central and forward rapidity, and as a function of jet rapidity for low and high jet p_T—high jet energy corresponds to low p_T at high rapidity.

The corrections do not show a significant dependence as a function of jet rapidity except in the region of the ICR. The uncertainties vary between 1.2% and 2.5% for the kinematic range of the cross section measurement and are dominated by the uncertainties of the jet response. The uncertainties obtained in the CC and for jet $p_T \approx 100$–500 GeV are the smallest ones obtained by any experiment operating at a hadron collider. These uncertainties do not depend strongly on jet pseudorapidity and p_T.

F. Closure tests

The aim of the closure tests is to verify the accuracy of the jet energy scale correction using either MC or data and to evaluate the remaining difference as an additional systematic uncertainty related to the method. As an example, one test is to use the full method in MC and to compare the results with the particle-level jet energy. The direct closure variable is defined as

$$D = \frac{\langle E_{\text{jet}}^{\text{corr}} \rangle}{\langle E_{\text{jet}}^{\text{particle}} \rangle}, \tag{17}$$

where $E_{\text{jet}}^{\text{corr}}$ is the corrected jet energy and $E_{\text{jet}}^{\text{particle}}$ is the energy of the closest particle jet matching the reconstructed jet within $\Delta R < R_{\text{cone}}/2$. Results from the direct closure test are shown in Fig. 22 in two regions of jet

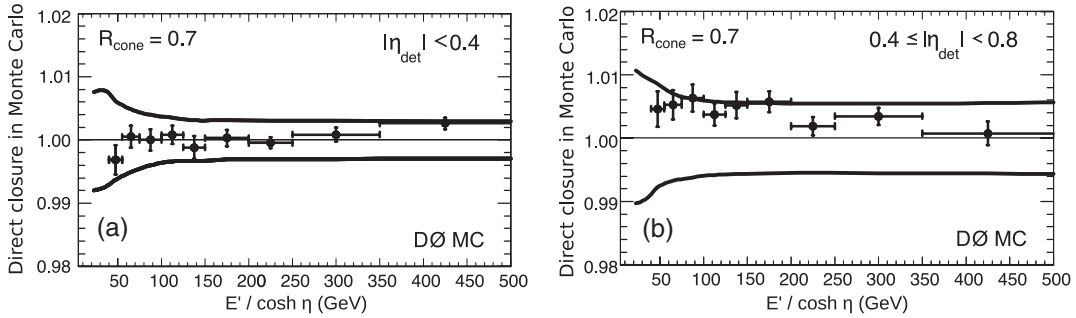

FIG. 22. Closure test of jet energy scale in MC for (a) $|\eta_{\text{det}}| < 0.4$ and (b) $0.4 < |\eta_{\text{det}}| < 0.8$. The band outlined by the solid curves corresponds to the uncertainties in the extraction of jet energy scale in MC which are mainly statistical.

rapidity. We note that we obtain consistency of the method within expected uncertainties (D is close to unity within less than 1%) and no additional systematic uncertainty is introduced. Closure tests using data are performed relative to MC by comparing ratios of fully corrected jet energies $\langle E_{\text{data}}^{\text{corrected}}\rangle/\langle E_{\text{MC}}^{\text{corrected}}\rangle$ in fixed regions of E' and η. Again we find good agreement within the expected uncertainties of the jet energy scale.

VI. TRIGGERING ON JETS

In this section, we briefly describe how we determine the absolute jet trigger efficiencies. Two different samples based on jet or muon triggers are used. The D0 trigger system is composed of three consecutive levels called L1, L2, and L3. At L1, a single jet trigger typically requires n calorimeter trigger towers above a given threshold, where a trigger tower is defined by the hardware summation of energies in 2×2 calorimeter towers. The trigger towers are read out separately from the precision calorimeter electronics via a fast digitizer and are used in both L1 and L2 triggers. All events used in this analysis are required to pass a L1 trigger designed to fire if a single jet with $p_T > 50$ GeV is in the event. For instance, the 65 GeV single jet trigger requires the presence of three calorimeter towers with a transverse momentum above 5 GeV. This requirement is often satisfied by the presence of trigger towers belonging to different jets, ensuring high trigger efficiency. In most of these events, there are two high-p_T jets in the event or more than two low-p_T jets, which ensures that the event passes the L1 threshold. A detailed analysis shows that the L1 single jet efficiency is more than 98% for the full kinematic range of our measurement, which is corrected for the residual inefficiency. At L2 we perform a clustering of the trigger tower energies and apply a threshold based on the p_T of highest energy cluster. Seven L3 triggers corresponding to uncorrected L3 jet p_T thresholds of 8, 15, 25, 45, 65, 95, and 125 GeV are used in the analysis. The highest-p_T L3 trigger was never prescaled during data collection. In Fig. 23, we show the jet cross section before any unfolding corrections as a function of jet p_T for the different jet triggers for two domains in jet rapidity $|y| < 0.4$, and $2.0 < |y| < 2.4$.

The first method used for computing the jet efficiency is to obtain the relative jet trigger efficiency with respect to the lower p_T jet trigger. For instance, the ratio of the 95 and 65 GeV triggers is shown in Fig. 24. For this purpose, we plot the ratio of the number of events that pass the 95 GeV trigger to those that pass the 65 GeV threshold as a function of jet p_T after jet energy scale and vertex efficiency corrections to cancel known luminosity dependencies as discussed in Sec. VII. The ratio is scaled by the relative integrated luminosities of these triggers to account for the different prescales. When this ratio reaches 1, the 95 GeV threshold trigger is 100% efficient with respect to the 65 GeV one. A fit to this ratio gives the different thresholds for which the triggers are fully efficient ($> 99.9\%$). The jet energy scale corrected p_T at which each trigger becomes fully efficient is given in Table I. These thresholds take into account the p_T binning used in the analysis and can be significantly higher than the minimum usable threshold. We note that this method does not allow us to obtain the absolute trigger efficiency since it gives all efficiencies with respect to the lowest 8 GeV p_T trigger as a reference.

A second method is used to measure the absolute single jet trigger efficiency. It uses independent muon and minimum bias triggers. The minimum bias trigger only requires energy deposits in the luminosity monitors. As its name indicates, it shows very little selection bias and is ideal for trigger studies. Unfortunately, the sample collected during all of Run II at the Tevatron at 0.5 Hz only yields statistics adequate to study jets below 70 GeV using this trigger, and this method does not allow exploration of the high p_T jet trigger efficiency. For this reason, inclusive muon triggers

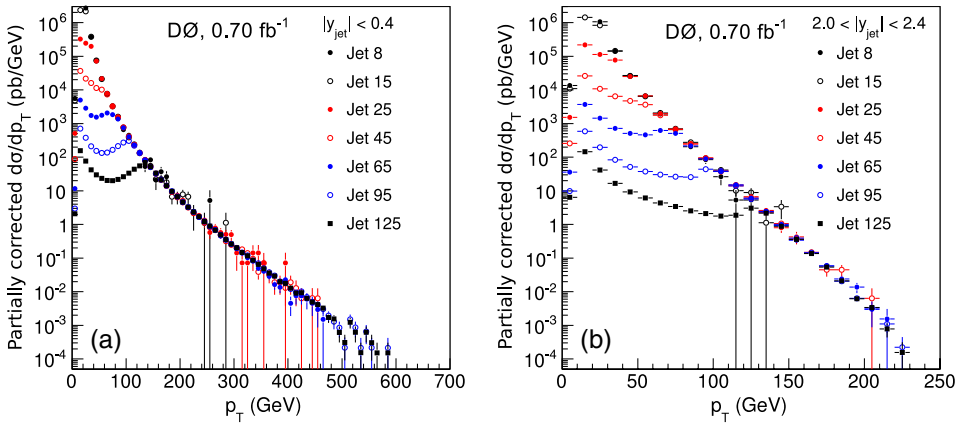

FIG. 23 (color online). (color online) Inclusive jet p_T cross section without unfolding corrections for the different single jet triggers as a function of jet p_T for (a) $|y| < 0.4$ and (b) $2.0 < |y| < 2.4$. The average prescales are 34000, 7100, 460, 41, 9.6, 1.4 and 1 for the 8, 15, 25, 45, 65, 95, and 125 GeV triggers, respectively.

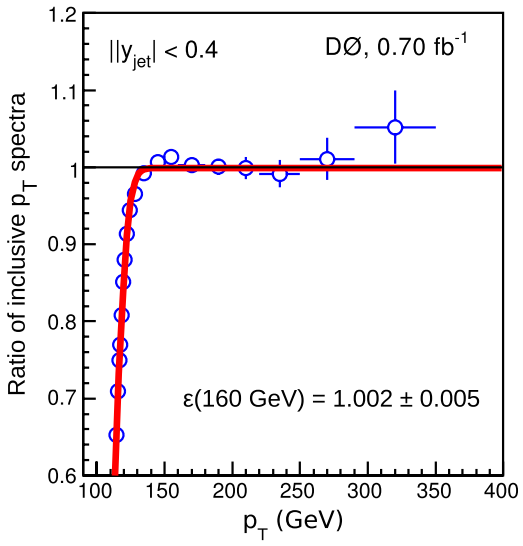

FIG. 24 (color online). (color online) Ratio of two consecutive jet triggers used to obtain the relative jet trigger efficiency for the 95 and 65 GeV single jet triggers. The fit of the turn-on curve determines the 95 GeV jet p_T 99%-threshold to be 130 GeV. A higher threshold of 160 GeV that is consistent with an efficiency $\epsilon = 1.00$ is used in the final analysis.

without any calorimeter requirements are also used. This allows us to check what fraction of the offline reconstructed jets in muon triggered events pass the calorimeter jet trigger requirement, providing a direct estimate of trigger efficiencies up to 400 GeV in the CC. The conclusion of this study is that all jet triggers are more than 98% efficient above the thresholds defined above, and the residual inefficiency is determined to a precision of better than 1%. Both methods to obtain the trigger efficiencies are useful since the muon triggers have a tendency to enrich the inclusive jet samples in b and c-jets where the b and c quarks decay leptonically, which might lead to different trigger efficiencies as a function of jet p_T.

VII. EVENT SELECTIONS AND EFFICIENCIES

In this section, we discuss the selections that are used to remove background events in the sample. The selections fall into three different categories. The event quality flags remove events suffering from diverse calorimeter noise issues. The vertex requirement selects events with a high quality vertex close to the center of the calorimeter to improve the jet p_T and y measurements and to reduce the background from cosmic ray events. The $\not\!\!E_T$ requirement is designed to remove the remaining cosmic ray background, especially at high jet p_T.

TABLE I. Jet energy scale corrected p_T in GeV at which each L3 trigger becomes fully efficient in different jet y bins.

Rapidity/L3 trigger	15	25	45	65	95	125
$\lvert y\rvert < 0.4$	50	60	100	120	160	200
$0.4 \leq \lvert y\rvert < 0.8$	50	60	100	120	160	200
$0.8 \leq \lvert y\rvert < 1.2$	50	90	110	140	190	230
$1.2 \leq \lvert y\rvert < 1.6$	50	80	90	140	190	240
$1.6 \leq \lvert y\rvert < 2.0$	50	70	90	110	160	190
$2.0 \leq \lvert y\rvert < 2.4$	50	70	90	120	160	200

A. Event quality flags

Event quality flags ensure that the subdetectors used in the analysis were working properly when the data were collected. Calorimeter event quality flags allow removal of events showing coherent pedestal shifts in the analog-to-digital converters, parts of the calorimeter not correctly read out, or high coherent noise. This is especially important for high-p_T jets which can originate artificially from noisy towers in the calorimeter. Note that the vertex and $\not\!\!E_T$ requirements also remove most of these events. The inefficiency induced by the calorimeter event quality flag rejection is estimated using an independent sample whose trigger is known to be unaffected by the calorimeter problems, the zero bias trigger. The inefficiency is calculated to be (3.2% ± 1.0%) where the 1.0% uncertainty covers the time and luminosity dependence of the inefficiency.

B. Reconstructed vertex requirement

The vertex selection is based on three different requirements: there must be at least one reconstructed vertex, the z-position along the beam line of the primary reconstructed vertex must be within 50 cm of the detector center ($|z_{\text{vertex}}| < 50$ cm), and the number of tracks fitted to the vertex has to be at least three to ensure an accurate measurement. The z-vertex position requirement ensures that the vertex is in the high-efficiency tracking region. The third requirement rejects vertices originating from fake high p_T tracks. To each reconstructed vertex is assigned a probability that it comes from a minimum bias interaction based on the $\ln(p_T)$ distributions of the tracks with $p_T > 0.5$ GeV pointing to the vertex. The vertex with the lowest minimum bias probability is selected as the primary vertex.

The efficiency of the requirement of at least three tracks pointing to the reconstructed vertex (without the requirement on the z-vertex position) is found to be (99.6% ± 0.4%), independent of jet p_T and y. This is determined by examining the distribution of track multiplicity in jet events and extrapolating below the three track requirement. The observed 0.4% inefficiency is consistent with about 0.6% of the primary vertices not being reconstructed because of tracking inefficiencies, and 0.2% being replaced by a minimum bias vertex.

The leading inefficiency comes from the requirement on the vertex position along the z-axis. The fraction of events rejected by this requirement is of the order of 7%. To determine the efficiency of this requirement we take into

account the shape of the luminous region. The longitudinal shape of the luminous region is approximated by the expression

$$\frac{d\mathcal{L}(z)}{dz} = N_p N_{\bar{p}} \frac{1}{\sqrt{2\pi}\sigma_z} \frac{e^{-(z-z_{0z})^2/2\sigma_z^2}}{4\pi\sigma_x(z)\sigma_y(z)}, \quad (18)$$

where the overlap of the proton and antiproton beam bunches having N_p and $N_{\bar{p}}$ particles is described with a Gaussian distribution of width σ_z in the z direction, with a possible offset z_{0z} relative to the nominal interaction point. $\sigma_x(z)$ and $\sigma_y(z)$ represent the transverse size of the beam spot and vary as a function of z:

$$\sigma_T^2(z) = \frac{1}{6\pi\gamma}\epsilon_T\beta_T^*\left[1 + \frac{(z - z_{0T})^2}{\beta_T^{*2}}\right]. \quad (19)$$

Here T is either x or y, z_{0T} is the minimum of the β function describing the beam dimensions near the interaction point in direction T and any offset in the x and y directions with respect to the nominal interaction point, γ is the Lorentz factor of the beam particles. The emittance ϵ_T and beta parameter β_T^* describe the beam dimensions at the interaction point. The parameterization can be integrated to yield

$$\epsilon_{|z_{\text{vertex}}|<50\text{ cm}} = \frac{\int_{-50\text{ cm}}^{50\text{ cm}} f(z_{\text{vertex}}, \text{run}, \mathcal{L})}{\int_{-140\text{ cm}}^{140\text{ cm}} f(z_{\text{vertex}}, \text{run}, \mathcal{L})}, \quad (20)$$

where the limits of integration in the denominator come from the requirements used in the luminosity determination. This parameterization is fitted to minimum bias data in the high tracking efficiency region ($|z_{\text{vertex}}| <$ 40–60 cm) in bins of instantaneous luminosity for several

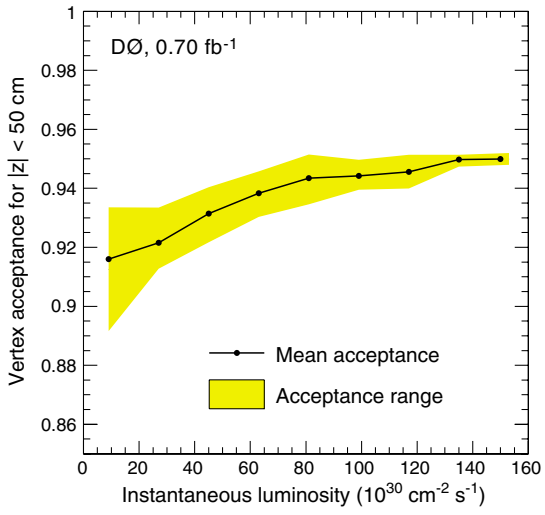

FIG. 25 (color online). (color online) Vertex acceptance for the requirement on the z-vertex position $|z_{\text{vertex}}| < 50$ cm as a function of instantaneous luminosity. The shaded band indicates the variation for different running periods.

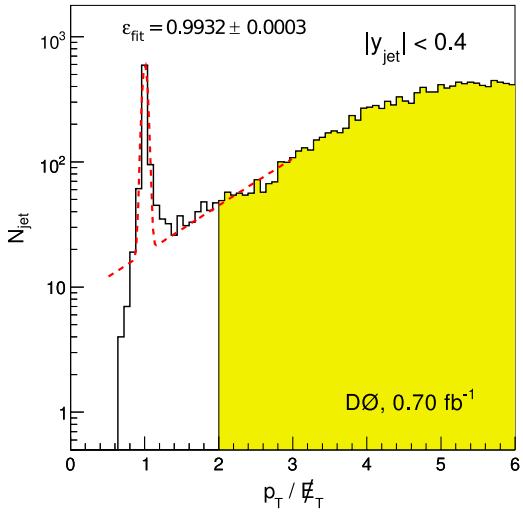

FIG. 26 (color online). (color online) Distribution of $p_{T,\text{lead}}/\not{E}_T$ for jet events with leading jet $p_T > 200$ GeV. A peak from cosmic ray background is visible around 1. The shaded region shows jets passing the $p_{T,\text{lead}}/\not{E}_T$ requirement.

run ranges (the changes in beam optics as a function of time affect the beam shape as described by the β^* parameter). The changes as a function of instantaneous luminosity are primarily due to the variations in the beam parameters during a store. The vertex efficiency varies by up to 6% as a function of instantaneous luminosity and by up to 4% as a function of the period of data taking for a fixed value of luminosity. The parameterizations have been determined as a function of time and instantaneous luminosity, and are applied as such on a per-event basis. Figure 25 shows the mean vertex efficiency as a function of instantaneous luminosity, with the range of efficiencies overlaid. The uncertainty on the vertex acceptance is estimated to be 0.5% by comparing results from fits to minimum bias data at $|z_{\text{vertex}}| < 60$ cm and $|z_{\text{vertex}}| < 40$ cm. In addition, an increased uncertainty of 0.4% added in quadrature at high $|y|$ is introduced to account for the possibility of a lower vertex reconstruction efficiency.

C. Missing transverse energy requirement

A requirement on the missing transverse energy in an event is applied to remove the remaining background from cosmic rays that induce showers in the calorimeter. The cross section for these cosmic ray interactions falls much less steeply versus p_T than the inclusive jet cross section, and is typically comparable at $p_T \approx 400$ GeV. The issue of background from cosmic rays is thus more important for high-p_T jets. Fortunately, cosmic ray showers deposit most of their energy on one side of the calorimeter, have no reconstructed vertex, and produce high uncorrected $\not{E}_T$ that peaks at $p_{T,\text{lead}}/\not{E}_T \approx 1$, where $p_{T,\text{lead}}$ is the uncorrected p_T of the leading jet of the event. These events are fully and efficiently removed by requiring $p_{T,\text{lead}}/\not{E}_T > 1.4$, when

$p_{T,\mathrm{lead}} < 100$ GeV and $p_{T,\mathrm{lead}}/\not{E}_T > 2.0$, when $p_{T,\mathrm{lead}} \geq 100$ GeV. Figure 26 shows the distribution of $p_{T,\mathrm{lead}}/\not{E}_T$ for the high-p_T jet trigger with $p_T > 200$ GeV, with the selected events at $p_{T,\mathrm{lead}}/\not{E}_T > 2.0$ shown by the shaded region. A spike coming from cosmic ray events is visible at 1. An upper limit of 0.4% is estimated on the inefficiency for jet identification due to the $\not{E}_T$ requirement and used as an uncertainty, but no correction is applied. This upper limit is based on studies of fits of distributions like the one in Fig. 26, and track-matching inefficiency for jets since cosmic ray events are usually out-of-time with the tracking readout.

VIII. JET IDENTIFICATION REQUIREMENTS AND EFFICIENCIES

The jet identification requirements are designed to remove instrumental backgrounds such as jets formed from sources of transient noise in the calorimeter and also physics backgrounds from electrons and photons. The jet requirements are based on the fractions of jet energy deposited in the electromagnetic calorimeter (EMF) and in the coarse hadronic calorimeter (CHF). EMF < 0.95 is required to remove overlaps between jets and electromagnetic objects, i.e. electrons and photons. A lower limit on EMF (either 0 or varying between 0.03 and 0.05 depending on the pseudorapidity region in the calorimeter) as well as an upper limit on CHF (varying between 0.4 and 0.6) removes jets that are formed predominantly out of noise in the hadronic calorimeter. An additional requirement, L1 confirmation, is based on the ratio of the p_T as measured by the L1 trigger system and as measured by the precision readout. It is required to be above 0.5 for jet $p_T < 80$ GeV, and there is no requirement for higher p_T jets. This removes jets formed out of noise, for example, due to coherent noise in the precision readout electronics.

The jet identification efficiencies are determined using a data-driven method. This method uses track jets which are jets built with a cone algorithm using charged particle tracks instead of calorimeter energy clusters. We select a leading p_T tagged object, which in this case is a photon or a track jet associated with a good calorimeter jet, and a probe object, which is the leading track jet that is back-to-back in ϕ with the tag object. Events with additional track jets are vetoed to ensure that the leading objects are balanced in p_T. The reconstruction efficiency is defined as the fraction of probe objects with a calorimeter jet found within the 0.7 jet cone, and the jet identification efficiency is the fraction of those calorimeter jets passing the jet identification requirements. The data-driven method has been used for three different samples: dijet, γ + jet, and Z + jet, which all lead to the same result. The central value for the jet identification efficiency shown in Fig. 27 is taken from the dijet sample. The efficiency for $p_T > 50$ GeV, where we perform the measurement of the inclusive jet p_T cross section, is 99% in all calorimeter regions except in the region $0.8 < |y| < 1.2$ where it is about 98%.

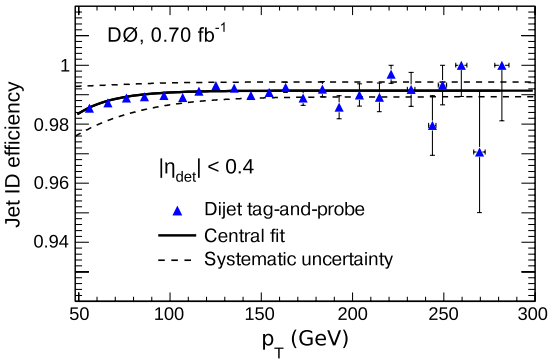

FIG. 27 (color online). (color online) Jet identification efficiencies obtained for the dijet sample. Dashed lines indicate the systematic uncertainty.

Because the data-driven method is used for calorimeter jets that are independently identified as track jets, we also directly measure the efficiencies by computing the fraction of events removed by each jet identification requirement individually after applying all other requirements in the inclusive jet sample. This method assumes that each jet identification cut removes only good jets. The efficiencies described above are found to be in good agreement with those from the tag-and-probe method.

IX. JET TRANSVERSE MOMENTUM RESOLUTION

In this section, we discuss the determination of the jet p_T resolution, which is needed for the unfolding of the inclusive jet p_T cross section. The jet p_T resolution is determined from data using the dijet asymmetry distribution, which can be obtained with minimal input from MC. This method requires corrections for the presence of additional unreconstructed jets (soft radiation), momentum imbalance at the particle level, and asymmetry bias due to non-Gaussian tails. We describe each correction needed to obtain the jet p_T resolution.

A. Dijet asymmetry

The jet p_T resolutions are determined starting from the dijet asymmetry

$$A = \frac{p_{T,1} - p_{T,2}}{p_{T,1} + p_{T,2}} \tag{21}$$

computed in a pure dijet sample with no additional jet identified, where $p_{T,1}$ and $p_{T,2}$ are the p_T of the leading and second-leading jets and the two leading jets are randomly assigned an index of 1 or 2. Both jets are required to be back-to-back with $\Delta\phi > 3.0$ to avoid any large effects from QCD radiation. The RMS of the asymmetry distribution is directly proportional to the jet p_T resolution

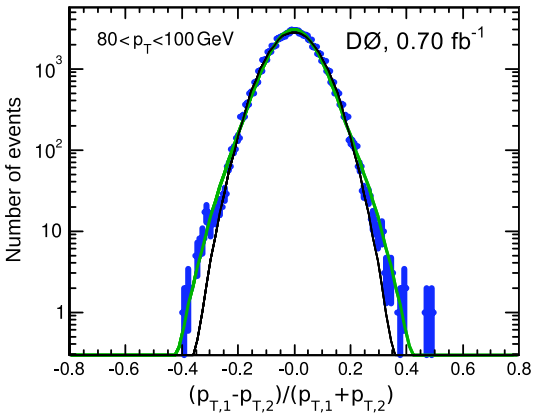

FIG. 28 (color online). (color online) Asymmetry distribution for jets in the central region with $80 < p_T < 100$ GeV. The probe jet is at $|y| < 0.4$, the reference jet at $|y_{\rm ref}| < 0.8$. The two lines display the result of a Gaussian fit and a Gaussian with smeared exponential tails (see Sec. IX C).

$$\sigma_A = \frac{1}{\sqrt{2}} \frac{\sigma_{p_T}}{p_T}, \tag{22}$$

if the jets are in the same y region to ensure that the p_T resolution of both jets is the same. To characterize the p_T dependence of the resolution for a single jet, σ_A is measured in bins of $p_T = (p_{T,1} + p_{T,2})/2$. This method can be used directly to measure the jet p_T resolution in the central region where the statistics are high. However, in the forward region, the statistics for forward-forward jet pairs are small compared to central-forward jet pairs. If one of the jets is in the central region and the other in the forward region, it is possible to infer the jet p_T resolution σ_{p_T} in the forward region once the resolution for jets in the central reference region $\sigma_{\rm ref}$ is known

$$\frac{\sigma_{p_T}}{p_T} = \sqrt{4 \cdot \sigma_A^2 - \left(\frac{\sigma_{\rm ref}}{p_T}\right)^2}. \tag{23}$$

The central reference region used in this study is $|y_{\rm ref}| < 0.8$, with the probe jet binning following the same 0.4 binning in rapidity as the rest of the analysis. The asymmetry distribution in the central region is shown in Fig. 28 for $80 < p_T < 100$ GeV as an example and other $p_T^{\rm jet}$ bins also show similarly small non-Gaussian tails.

B. Corrections to the resolution

The jet p_T resolution determined from the dijet asymmetry can be affected by physics and instrumental effects. The final parameterization of the resolution used in this analysis includes corrections to remove biases in the measurement as described below.

1. Soft-radiation corrections

The asymmetry method to compute the jet p_T resolution is biased by the presence of nonreconstructed jets in the sample. The p_T threshold to reconstruct a jet is 6 GeV, and requesting the presence of only two jets in the sample to compute the asymmetry does not ensure the absence of jets with p_T below 6 GeV. The corrections for such soft radiation are determined directly in data. We compute the asymmetry and the jet p_T resolution for different p_T thresholds for jet reconstruction, namely, 7, 8, 10, 12, 15, 20, and 40 GeV. The jet p_T resolution as a function of the jet reconstruction threshold is shown in Fig. 29(a) for one bin in jet p_T and $|y|$. A linear fit allows for extrapolating the jet p_T resolution to a threshold p_T of 0. The soft-radiation factor,

$$K_{\rm soft} = \frac{\sigma_{p_T}(p_{T,\rm soft}^{\rm cut} \to 0)/p_T}{\sigma_{p_T}(p_{T,\rm soft}^{\rm cut} = 6\ {\rm GeV})/p_T}, \tag{24}$$

is studied as a function of the average jet p_T in each $|y|$ bin as illustrated in Fig. 29(b). To better describe the low p_T region and limit the statistical fluctuations, the dependency of $K_{\rm soft}$ versus p_T is fitted with

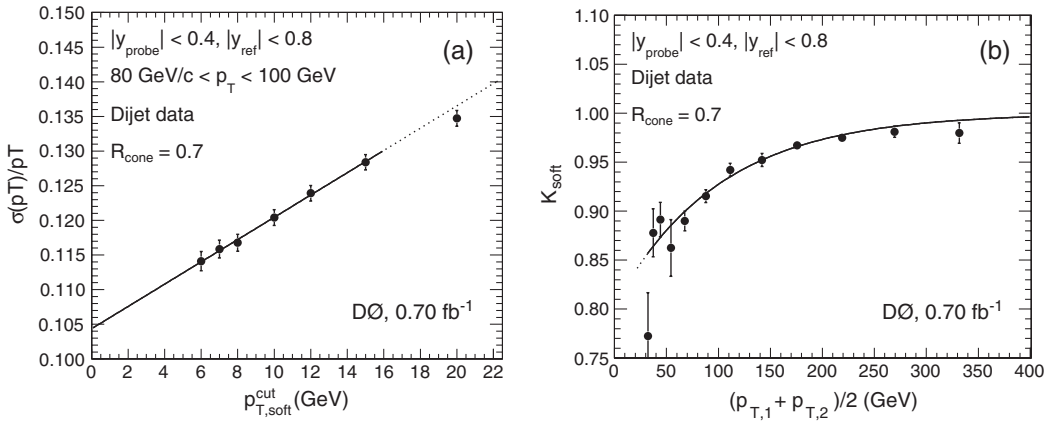

FIG. 29. (a) Jet p_T resolution extrapolated to a jet p_T reconstruction threshold of 0 GeV (in the $80 < p_T < 100$ GeV and $|y| < 0.4$ bin). (b) Soft-radiation correction factor as a function of the average jet p_T for the $0.4 < |y| < 0.8$ bin. The solid lines are the fit result and the dashed lines are the result of the extrapolations.

$$K_{\text{soft}}(p_T) = 1 - \exp(-p_0 - p_1 p_T), \quad (25)$$

where p_0 and p_1 are two parameters of the fit.

2. Particle imbalance and combined corrections

The remaining correction needed to obtain the final jet p_T resolution is the particle imbalance correction. Even in the ideal situation of only two particle jets and no soft radiation, the two jets are not necessarily perfectly balanced. In particular, fragmentation effects cause some energy and p_T to be found outside the jet cone. This effect is purely related to QCD and is determined using a MC simulation. The particle-level imbalance is corrected for soft radiation using the same method as introduced for data

$$K_{\text{soft}}^{\text{MC}} = \frac{\sigma_{p_T}^{\text{ptcl}}(p_{T,\text{ptcl}}^{\text{threshold}} \to 0)/p_T}{\sigma_{p_T}^{\text{ptcl}}(p_{T,\text{ptcl}}^{\text{threshold}} = 6\ \text{GeV})/p_T}, \quad (26)$$

$$\sigma_{\text{MC}} = K_{\text{soft}}^{\text{MC}} \cdot \sigma_{p_T}^{\text{ptcl}}, \quad (27)$$

where $\sigma_{p_T}^{\text{ptcl}}$ is the resolution evaluated at the particle level in the MC and $p_{T,\text{ptcl}}^{\text{threshold}}$ is the p_T threshold of jet reconstruction at the particle level.

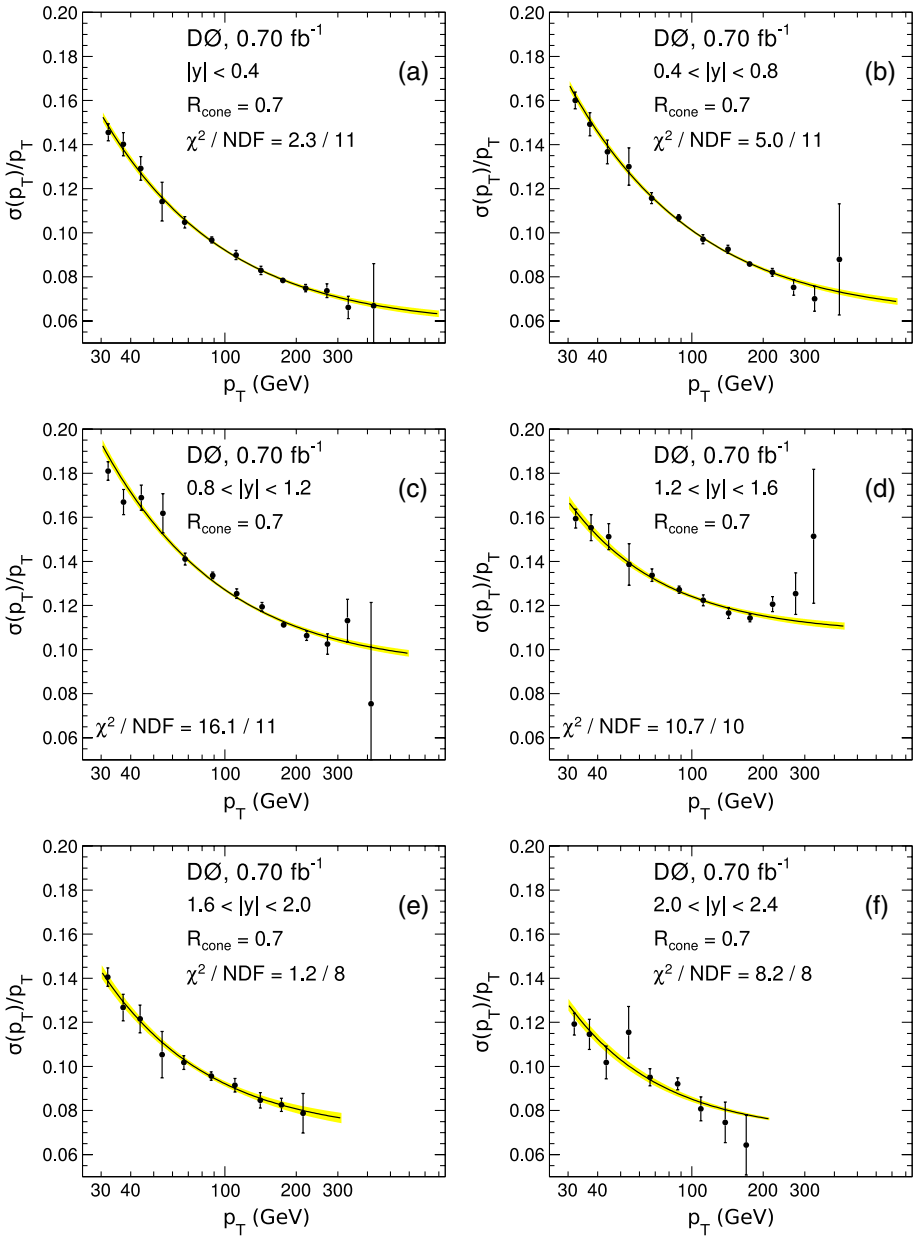

FIG. 30 (color online). (color online) Jet p_T resolution determined in data for the six rapidity regions. The solid curves are the results of the fit. The fit uncertainty is given by the shaded band.

TABLE II. Parameters of the fits to the jet p_T resolution versus p_T for data. The noise term is fixed to the MC value with an uncertainty of 1 GeV since it is not constrained by the data.

	N (oise)	S (tochastic)	C (onstant)
$\lvert y\rvert < 0.4$	2.07	0.703	0.0577
$0.4 < \lvert y\rvert < 0.8$	2.07	0.783	0.0615
$0.8 < \lvert y\rvert < 1.2$	2.07	0.888	0.0915
$1.2 < \lvert y\rvert < 1.6$	2.07	0.626	0.1053
$1.6 < \lvert y\rvert < 2.0$	2.07	0.585	0.0706
$2.0 < \lvert y\rvert < 2.4$	2.07	0.469	0.0713

The corrected particle-level imbalance σ_{MC} is subtracted in quadrature from the soft-radiation corrected resolution computed in data (see previous section),

$$\sigma_{\mathrm{corr}} = \sqrt{(K_{\mathrm{soft}}\sigma_{p_T})^2 - \sigma^2_{\mathrm{MC}}}. \tag{28}$$

The relative correction due to particle-level imbalance is about (7%–9%) in the CC, (2%–6%) in the ICR and the EC, for $p_T > 50$ GeV. The systematic uncertainties on particle imbalance corrections are mainly due to the differences between the Gaussian one standard deviation and the RMS of the particle-level imbalance distribution due to non-Gaussian tails. The RMS is used for the central correction. The main non-Gaussian tails in particle-level imbalance corrections are caused by muons and neutrinos, which are not included in the definition of D0 particle jets.

C. Final jet p_T resolutions

Using the asymmetry method and the various corrections discussed above, we obtain the jet p_T resolutions shown in Fig. 30. The measured resolutions are fitted with the parameterization

$$\frac{\sigma_{p_T}}{p_T} = \sqrt{\frac{N^2}{p_T^2} + \frac{S^2}{p_T} + C^2}, \tag{29}$$

where N is the noise term, S the stochastic term, and C the constant term. The values of the parameters are given in Table II. These resolutions are used to obtain the inclusive jet p_T cross section as described in the next section.

We note that the resolution is not Gaussian at high p_T even in the central region because of calorimeter punch-through: jets at very high p_T are not always fully contained in the calorimeter and can deposit energy into the muon system. In Fig. 31(a), we show the distribution of $(p_{T,\mathrm{jet}}/p_{T,\mathrm{ptcl}} - 1)$—the ratio of the reconstructed to the particle-level jet p_T—obtained from MC simulation of the detector in the central region of the calorimeter at high p_T. The ICR also exhibits non-Gaussian tails as shown in Fig. 31(b), which are explained by the changing structure of the calorimeter in this region. The non-Gaussian tails are modeled using a smeared exponential

$$f(p_T, \mu, \sigma, P, \lambda) = (1 - P) \cdot \frac{1}{\sqrt{2\pi}\sigma} e^{(p_T-\mu)^2/(2\sigma^2)} + \frac{P\lambda}{2} \cdot \exp\left[\lambda\left(p_T - \mu + \frac{\lambda\sigma^2}{2}\right)\right] \times \mathrm{erfc}\left(\frac{p_T - \mu + \lambda\sigma^2}{\sqrt{2}\sigma}\right), \tag{30}$$

with μ, σ, P, and λ as free parameters. The parameter μ accounts for shifts in the mean jet p_T due to punch-through, P is the fraction of jets with punch-through, and λ represents the exponential distribution of energy loss due to punch-through. The fitted shape from MC is scaled by varying the parameter σ such that folding the distributions for the leading jets with the exponential p_T spectrum from data results in precisely the same RMS of the jet p_T resolution as observed in data when the resolution functions are symmetrized. This method can account for any shaping of the non-Gaussian tails that takes place due to bin-to-bin migrations in data. The full MC shape with tuned σ is later used in the unfolding of the data.

The uncertainties on jet p_T resolution are given in Fig. 32 for two bins in rapidity as an example. The uncertainties come primarily from the statistical uncertainties in the fits. An additional component is added to cover

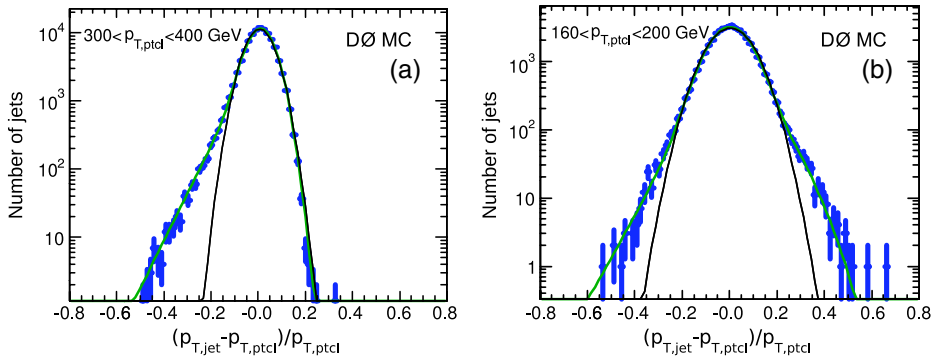

FIG. 31 (color online). (color online) (a) example of punch-through for $|y| < 0.4$ at high jet p_T for $300 < p_T < 400$ GeV and $|y| < 0.4$. (b) example of tails of the jet p_T resolution in the ICR for $160 < p_T < 200$ GeV and $0.8 < |y| < 1.2$. The two curves are the result of the Gaussian fit and of a Gaussian plus exponential tails.

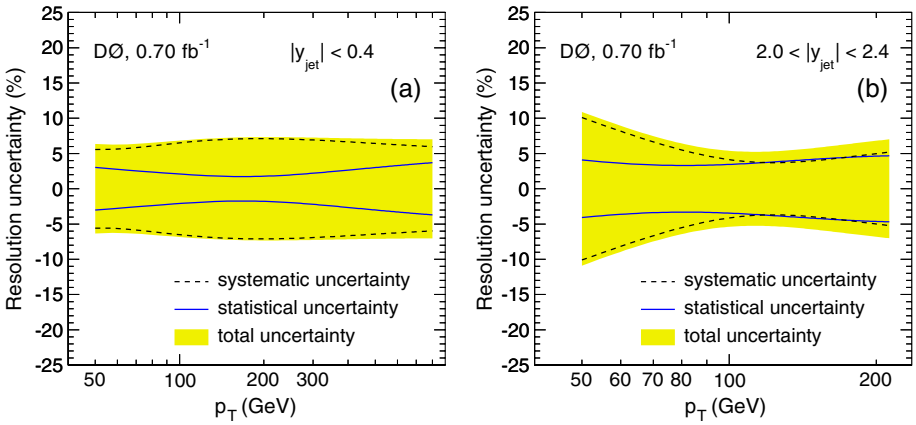

FIG. 32 (color online). (color online) Relative statistical and systematic uncertainties on jet p_T resolution for (a) $|y| < 0.4$ and (b) $2.0 < |y_{\text{jet}}| < 2.4$.

nonstatistical variations between the fit model and the data. The total uncertainty coming from the jet p_T resolution is (5%–10%) over the full kinematic range covered by the inclusive jet cross section measurement ($p_T > 50$ GeV). The leading systematic uncertainty in the central region is (4%–5%) due to the uncertainties on the particle-level imbalance corrections. In the ICR, an important systematic is due to the uncertainty on the tails in the resolution for this region. This systematic is estimated by varying the size of the tails by a factor of two to cover differences in the effects of using the RMS resolution and one with explicitly modeled tails and is evaluated by propagating the resulting variation in shape through the unfolding procedure for data. Another important source of uncertainty is taken from the following MC closure test: the full resolution measurement using the asymmetry is redone using a full simulation of the D0 detector, and the difference between the true MC resolution $\sigma(p_T^{\text{detector}} - p_T^{\text{particle}})$ and the result of the method is taken as a systematic uncertainty. This amounts to up to about 10% uncertainty in the resolution at $p_T = 50$ GeV in the forward region.

X. JET RAPIDITY RESOLUTION

Compared to the jet p_T resolution, the rapidity resolution is a small effect which is determined using a MC simulation of the detector. The bin width in y is much larger than the y resolution and bin-to-bin migrations only occur at the bin edges. To unfold the effect of the rapidity resolution, a smooth parameterization of the resolution as a function of y is used. The result of the parameterization of the y resolution in different p_T bins is shown in Fig. 33.

XI. UNFOLDING

In this section, we describe the method used to unfold the data as a function of jet p_T and y. As we already mentioned, the main smearing effect is due to the jet p_T resolution while the y smearing is only a second-order effect. The steeply falling jet p_T cross section convoluted with the jet p_T resolution leads to an increase of the observed cross section as a function of the measured jet p_T. To unfold the data, we use the so-called ansatz method. We start with a functional form for the cross section that has only a few parameters, smear it with the jet p_T and y resolutions, and fit the parameters so that it describes the raw cross section measurement before unfolding.

The ansatz used in each rapidity bin contains a p_T dependence term and an additional rapidity dependence

$$f(p_T, \eta) = N_0 \left(\frac{p_T}{100\ \text{GeV}}\right)^{-\alpha} \left[1 - \frac{2p_T \cosh(|y_{\text{min}}|)}{\sqrt{s}}\right]^{\beta} \cdot \exp(-\gamma p_T). \quad (31)$$

Here $\sqrt{s} = 1960$ GeV is the center-of-mass energy and $|y_{\text{min}}|$ is the low edge of the bin in absolute rapidity. The ansatz is based on phenomenological fits and motivated by the parton model [32]. The exponential term represents

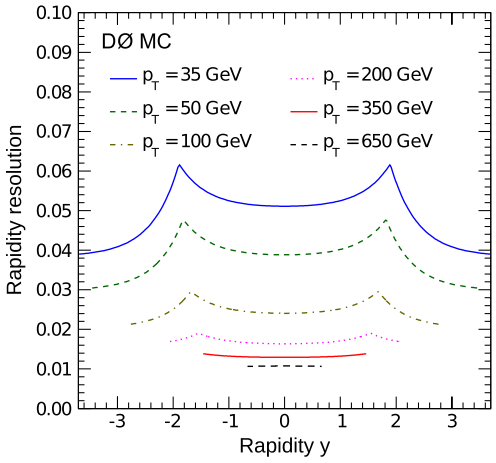

FIG. 33 (color online). (color online) Rapidity resolution (RMS) as a function of y in different jet p_T regions.

hydrodynamic production by freezing out particles from the quark and gluon sea. The value of γ is expected to be of the order of 0.3–0.6 GeV^{-1}, typical of the proton size. The first power term characterized by α represents the scaling violations associated with hard production. Typical values of α are 4–6 for single particle production. The second power term characterized by β represents the kinematic suppression effect at the edges of the phase space of particle production.

The ratios between the data and the smeared ansatz are shown in Fig. 34, where the ansatz correctly describes the data in all y bins. The unfolding corrections for the p_T resolution effects are shown by the dashed lines in Fig. 35. The unfolding corrections are (10%–40%) in the CC, (20%–80%) in the ICR where the jet p_T resolution is worse, and (15%–80%) in the EC where the jet cross section falls steeply. The highest p_T bin (where the unfolding corrections are the largest) where the cross section measured is chosen so that the cross section measurement is still meaningful; the number of events should still be sufficient to give a lower limit on the measured cross section at the 95% C.L. ($N_{\mathrm{theory}}/\sqrt{N_{\mathrm{smearedtheory}}} \geq 1.645$).

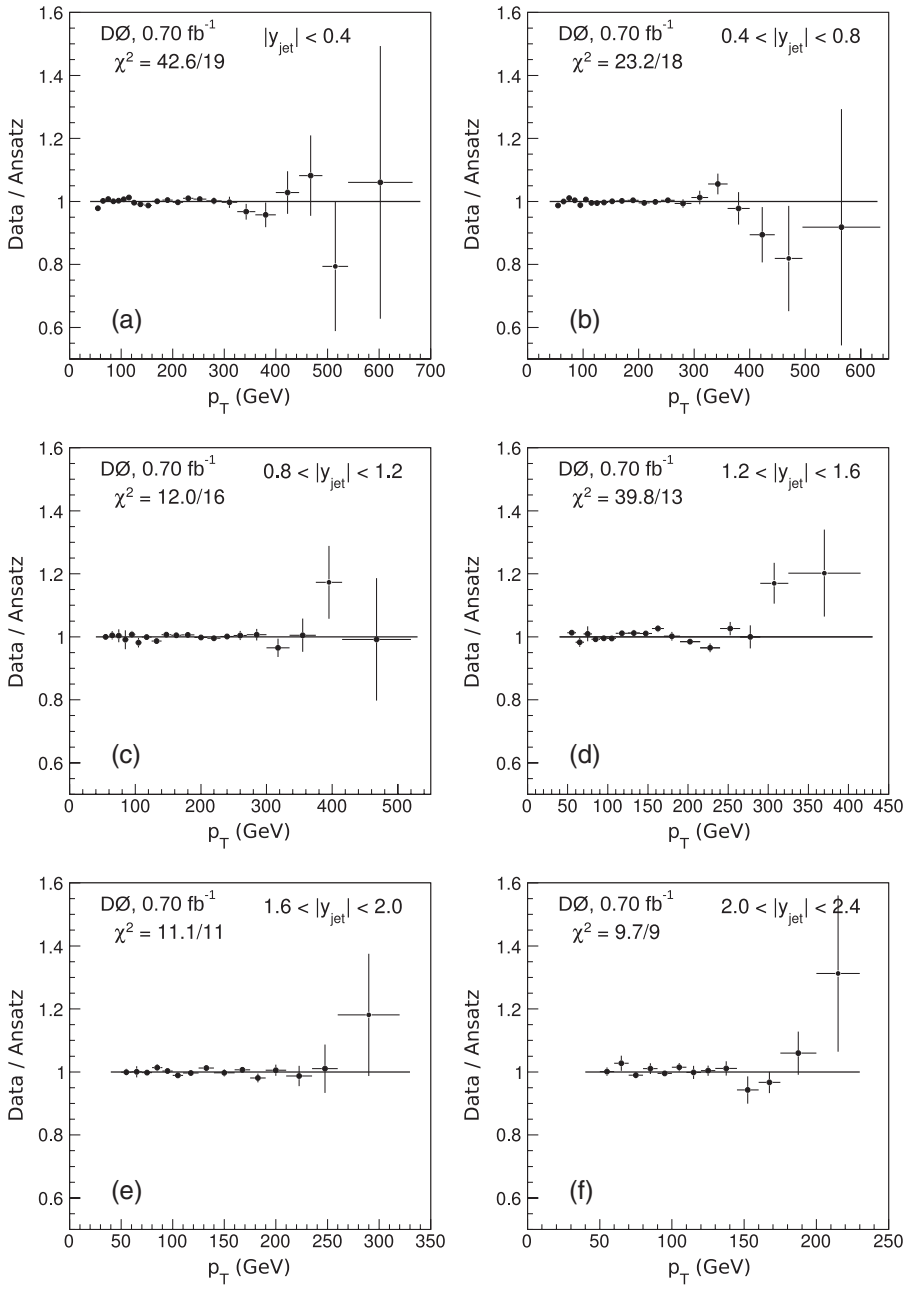

FIG. 34. Data divided by the ansatz fit with models for p_T and y smearing in the six rapidity regions.

Although in some bins most of the events migrate from lower p_T, the migrations are well understood and result in a relatively small uncertainty compared to the uncertainty from the jet energy scale. The ansatz unfolding is found to be in good agreement with the results using the PYTHIA MC where the cross section is rescaled to data and the jets at particle level are smeared according to the p_T resolutions obtained in Sec. XI.

The same ansatz unfolding method can be used to unfold the cross section for effects of the resolution for resolving rapidity, assuming the p_T and y resolutions are uncorrelated. Since the y resolution is much better than the p_T resolution, the effects of the y resolution are a small perturbation on top of the p_T smearing. The fits to the unfolded p_T spectra (unfolded for p_T resolution effects only) in neighboring rapidity bins are interpolated with respect to rapidity to produce a smooth, continuous two-dimensional spectrum in p_T and y. A final unfolding is performed to correct for events that migrate into neighboring rapidity regions due to effects of the y resolution. The results of the y unfolding as a function of jet p_T in the different y bins are given in Fig. 35, together with the

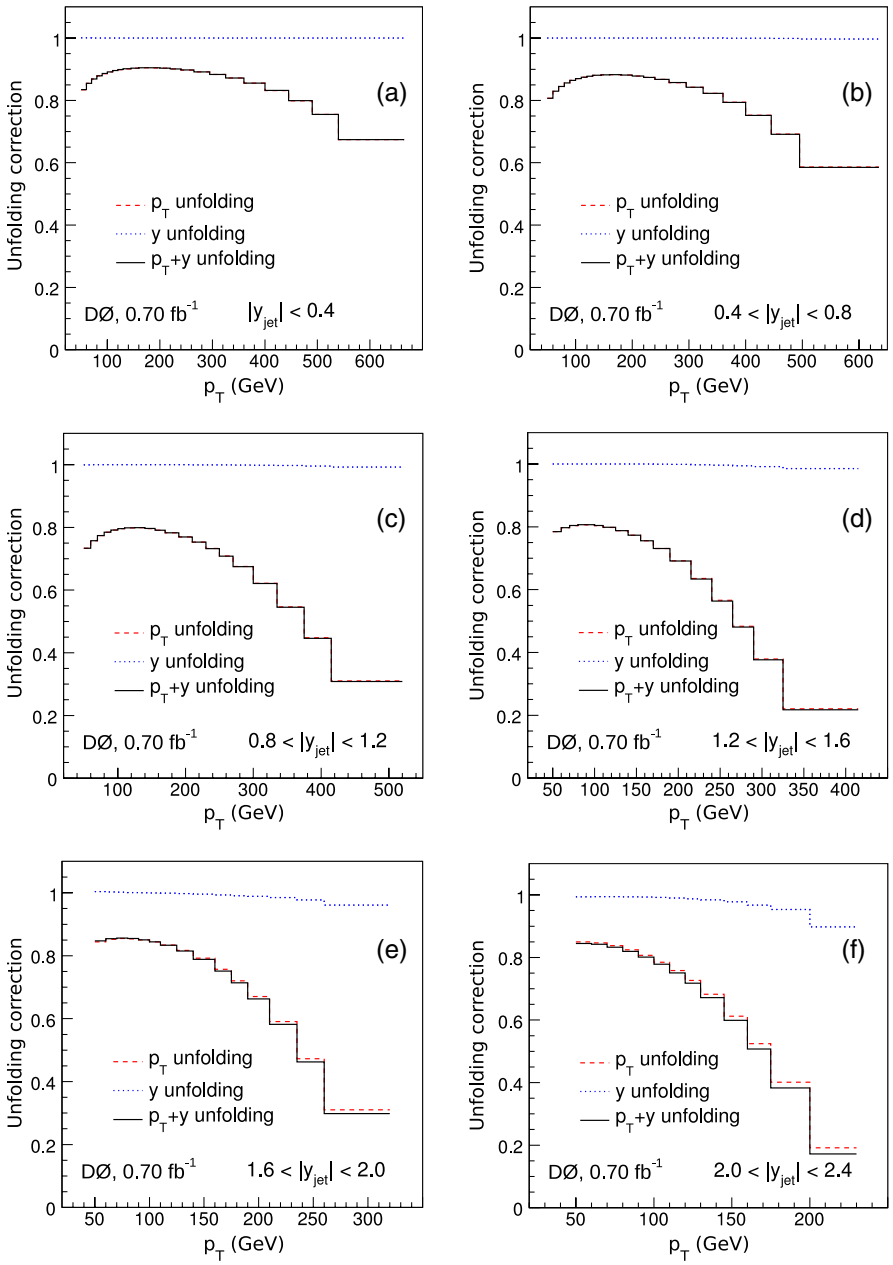

FIG. 35 (color online). (color online) Unfolding corrections in the six rapidity regions as a function of jet p_T. The corrections are given for p_T, y unfolding separately and combined.

results of the global unfolding corrections in jet p_T and y. As expected, the effects of y unfolding are very small with respect to the effects of the p_T unfolding.

XII. NCLUSIVE JET p_T CROSS SECTION MEASUREMENT

In this section, we describe the final result on the inclusive jet p_T cross section measurement applying the corrections defined in the previous sections: jet energy scale, efficiencies, and unfolding, used in order to compute the true number of events corresponding to each p_T and y bin. The cross section results are given in Fig. 36 in the six y bins as a function of jet p_T. The data points are plotted according to the prescription described in Ref. [33] and the tabulated data are available from Ref. [34].

The method used to extract the cross section is repeated and cross checked using a MC simulation of the detector. Events are generated using PYTHIA and weighted to match the NLO prediction calculated using the CTEQ6.5M PDFs and including nonperturbative corrections. The MC events are treated in the same way as data, all corrections are rederived using MC events, and the derived cross section is compared to the input cross section to perform a closure test of the measurement. The results given in Fig. 37 show that the method used to extract the cross section works well within the statistical uncertainties of the fits to the jet response, jet p_T resolution and p_T spectrum. These MC uncertainties are significantly smaller than the systematic uncertainties present in data.

In Fig. 36 the measurement is compared to the prediction of NLO QCD using the CTEQ6.5M PDF parameterization computed using the NLOJET++ program and FASTNLO. The central CTEQ6.5M prediction uses the factorization and renormalization scales $\mu_F = \mu_R = p_T$. The alternative scale choices $\mu_F = \mu_R = 0.5p_T$ and $\mu_F = \mu_R = 2p_T$ are used to estimate the theoretical uncertainty on the higher order corrections.

The NLO PQCD prediction is corrected for nonperturbative effects to connect the parton-level jets predicted by theory to the measured particle-level jets. The leading nonperturbative corrections are hadronization and underlying event which partially cancel. Another small correction is the exclusion of muons and neutrinos from the definition of the particle jets. The muon/neutrino energy loss is not corrected by the JES procedure using the MPF method in γ + jet events. The MC corrections have been obtained using PYTHIA v6.412 with parameters for tune QW [35] obtained by tuning PYTHIA to reproduce CDF Run II data. The strong coupling constant is fixed to $\alpha_s(M_Z) = 0.118$ at the Z boson mass and uses the 2-loop formula for the Q^2 evolution of α_s. The PYTHIA cross section is reweighted in $\hat{s}$ so that the PYTHIA parton shower prediction agrees with NLO pQCD. The correction factors for hadronization and the underlying event are shown in Fig. 38. As shown in Fig. 36, the measurement is well described by NLO QCD over eight orders of magnitude in the six y bins.

To check more precisely how well the measurement is described by the NLO QCD theory, we display the ratio of data over theory in Fig. 39, where the theory is calculated using the CTEQ6.5M PDF parameterization. The PDF uncertainties represented as dashed lines are calculated using the set of 20 eigenvectors provided by the CTEQ Collaboration for the CTEQ6.5M PDF fits. Data and theory agree within experimental and theoretical uncertainties, but data seems to favor the lower end of the CTEQ6.5M PDF 90% confidence level uncertainty band. Data are also

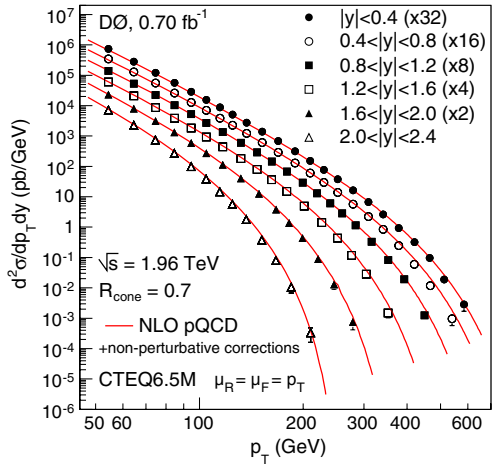

FIG. 36 (color online). (color online) Inclusive jet cross section measurements as a function of jet p_T in six $|y|$ bins. The data points are multiplied by 2, 4, 8, 16, and 32 for the bins $1.6 < |y| < 2.0$, $1.2 < |y| < 1.6$, $0.8 < |y| < 1.2$, $0.4 < |y| < 0.8$, and $|y| < 0.4$, respectively.

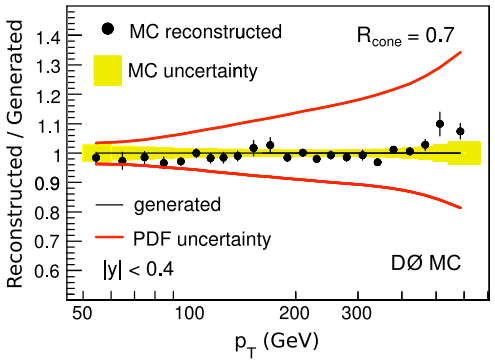

FIG. 37 (color online). (color online) MC closure test of the method used to extract the inclusive jet p_T cross section for the jet $|y| < 0.4$ bin. The full analysis was repeated treating MC events as data and comparing the result to the input cross section. Good agreement is found within the statistical uncertainties of fits to jet energy scale and resolution, and unfolding present in MC (shaded band), which are much smaller than the systematic uncertainties in data.

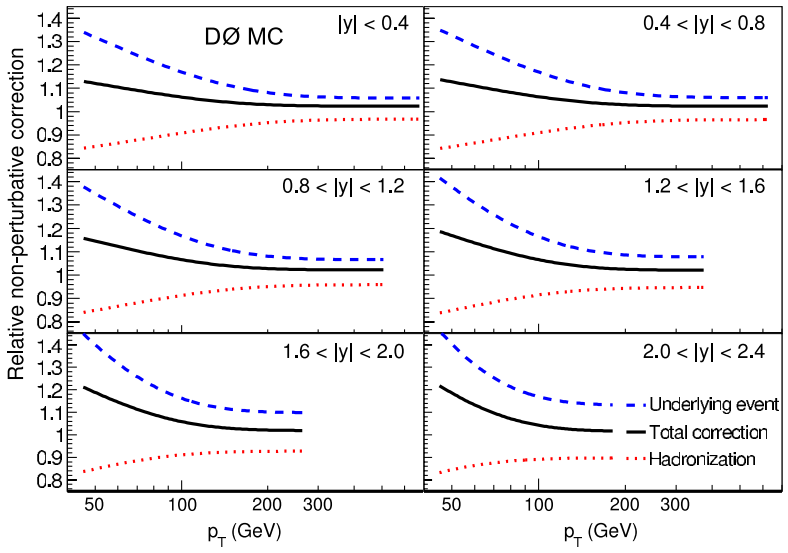

FIG. 38 (color online). (color online) Hadronization (dashed line) and underlying event (dotted line) corrections for inclusive jet cross section and the product of both corrections (solid line). The uncertainty on the theory is estimated as 50% of the individual corrections added in quadrature.

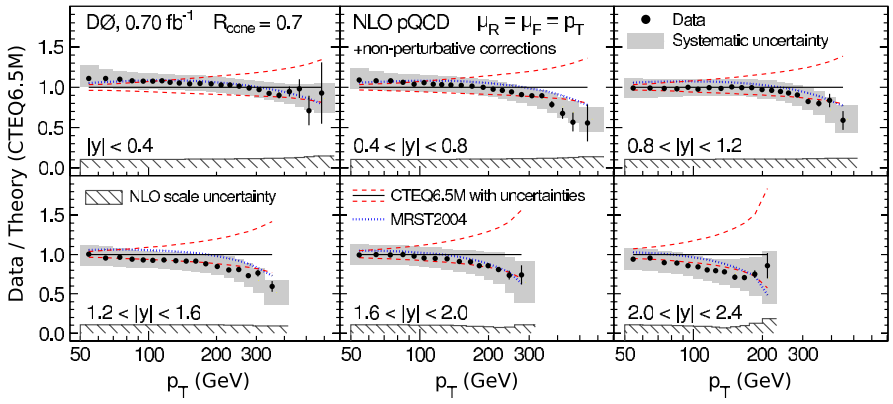

FIG. 39 (color online). (color online) Measured data divided by theory for the inclusive jet cross section as a function of jet p_T in the six $|y|$ bins. The data systematic uncertainties are displayed by the shaded band. NLO pQCD calculations, with renormalization and factorization scales set to jet p_T using the CTEQ6.5M PDFs and including nonperturbative corrections, are compared to the data. The CTEQ6.5 PDF uncertainties are shown as dashed lines and the predictions with MRST2004 PDFs as dotted lines. The theoretical uncertainty, determined by changing the renormalization and factorization scales between $p_T/2$ and $2p_T$, is shown at the bottom of each figure.

compared to the NLO QCD calculations using the MRST2004 PDF parameterization and our agreement in shape is good. The experimental uncertainties are smaller than the present PDF uncertainties, so these data further constrain the PDFs.

Some recent parameterizations have already used our measured jet cross sections described here to further constrain the PDFs (MSTW2008, CT10, NNPDFv2.1). As an example, we display in Fig. 40 the ratio data over theory, where the NLO theory is calculated using the MSTW08 NLO PDF [36] which displays good agreement between our measurement and this parameterization, with a tendency to be slightly different at high jet p_T where the uncertainties are larger. For reference, we also display in Fig. 41 the ratio of data over theory where the theory uses the recent HERAPDFv1.0 PDF [37], which uses only HERA data to constrain PDFs. We notice some discrepancies between our measurement and the HERAPDFv1.0 PDF at medium jet p_T especially in the central region, and at high p_T in the forward region. We also compare our data with the ABKM09NLO [38] parameterization in Fig. 42 and we notice some disagreement between our data and the predictions, in particular, on the normalization. This shows the capability of our data to constrain further the PDFs. Furthermore, we compare our measurements to the recent CT10 [39] parameterization in Fig. 43.

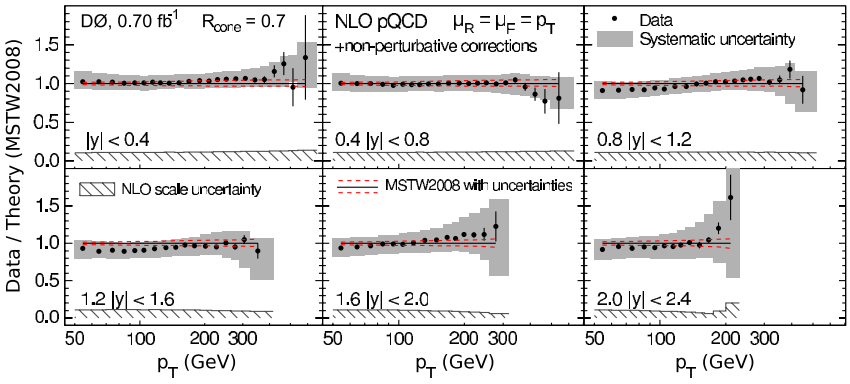

FIG. 40 (color online). (color online) Measured data divided by theory for the inclusive jet cross section as a function of jet p_T in the six $|y|$ bins using the MSTW2008 parameterization. The data systematic uncertainties are displayed by the shaded band. The theoretical uncertainty, determined by changing the renormalization and factorization scales between $p_T/2$ and $2p_T$, is shown at the bottom of each figure.

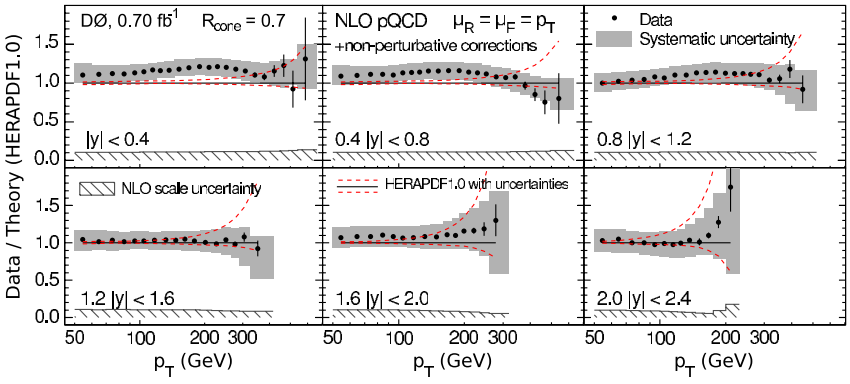

FIG. 41 (color online). (color online) Measured data divided by theory for the inclusive jet cross section as a function of jet p_T in the six $|y|$ bins using the HERAPDF1.0 parameterization. The data systematic uncertainties are displayed by the shaded band. The theoretical uncertainty, determined by changing the renormalization and factorization scales between $p_T/2$ and $2p_T$, is shown at the bottom of each figure.

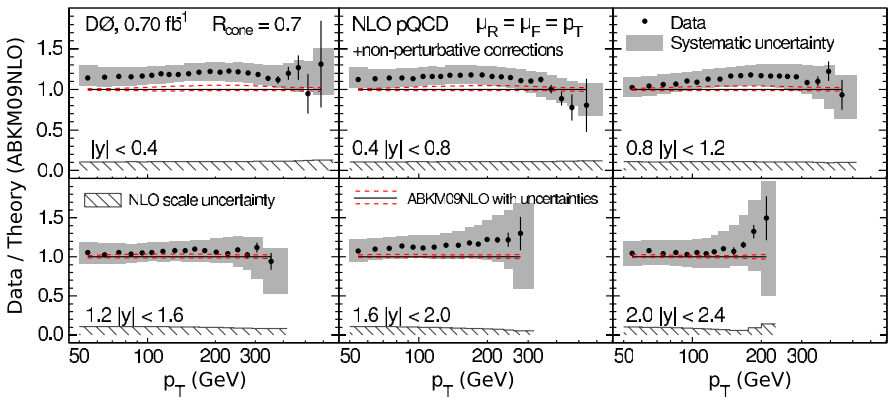

FIG. 42 (color online). (color online) Measured data divided by theory for the inclusive jet cross section as a function of jet p_T in the six $|y|$ bins using the ABKM09 parameterization. The data systematic uncertainties are displayed by the shaded band. The theoretical uncertainty, determined by changing the renormalization and factorization scales between $p_T/2$ and $2p_T$, is shown at the bottom of each figure.

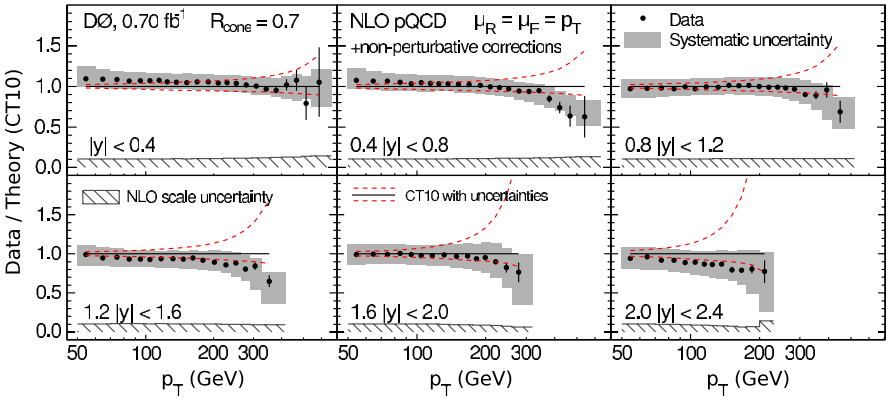

FIG. 43 (color online). (color online) Measured data divided by theory for the inclusive jet cross section as a function of jet p_T in the six $|y|$ bins using the CT10 parameterization. The data systematic uncertainties are displayed by the shaded band. The theoretical uncertainty, determined by changing the renormalization and factorization scales between $p_T/2$ and $2p_T$, is shown at the bottom of each figure.

There is a good agreement with data with the tendency of the CT10 parameterization to be higher at large p_T in all $|y|$ bins. Finally, we compare our measurement with the predictions from the NNPDFv2.1 [40] parameterization in Fig. 44 and again good agreement is found with our data.

The details of the uncertainties on the inclusive jet p_T cross section are given in Fig. 45. The dominant uncertainty is due to the systematic uncertainties on the jet energy scale, but the unfolding and the uncertainties related to the resolution in jet p_T are also important, especially at high p_T and high $|y|$. The 6.1% luminosity uncertainty is the second largest uncertainty at low p_T and the third largest at high p_T, and leads to significant uncertainty in the overall normalization of the cross section. For a jet $p_T \approx 150$ GeV, it is similar to the jet energy scale uncertainty. The uncertainties related to efficiencies are small everywhere.

XIII. UNCERTAINTY CORRELATIONS

Correlations between systematic uncertainties are studied in detail to increase the value of these data in future fits to model parton distributions and their impact on LHC physics predictions, in particular. In total, there are 91 independent sources of systematic uncertainty, and in this section we describe the method we use to group those with similar impact on the shape of the cross section to find the principal components of the uncertainty without significantly impacting the overall quality of the data. Many of the systematic sources we describe above are small in magnitude and highly correlated in shape with other sources.

The traditional interpretation of uncertainties to be independent requires that at each point the sum of all sources in quadrature must equal the total systematic uncertainty. In practice, adding in quadrature sources with similar shapes whose orthogonal components (defined later) are

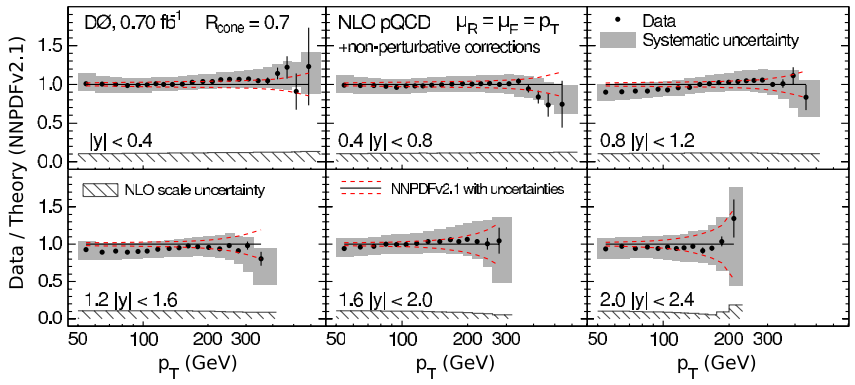

FIG. 44 (color online). (color online) Measured data divided by theory for the inclusive jet cross section as a function of jet p_T in the six $|y|$ bins using the NNPDFv2.1 parameterization. The data systematic uncertainties are displayed by the shaded band. The theoretical uncertainty, determined by changing the renormalization and factorization scales between $p_T/2$ and $2p_T$, is shown at the bottom of each figure.

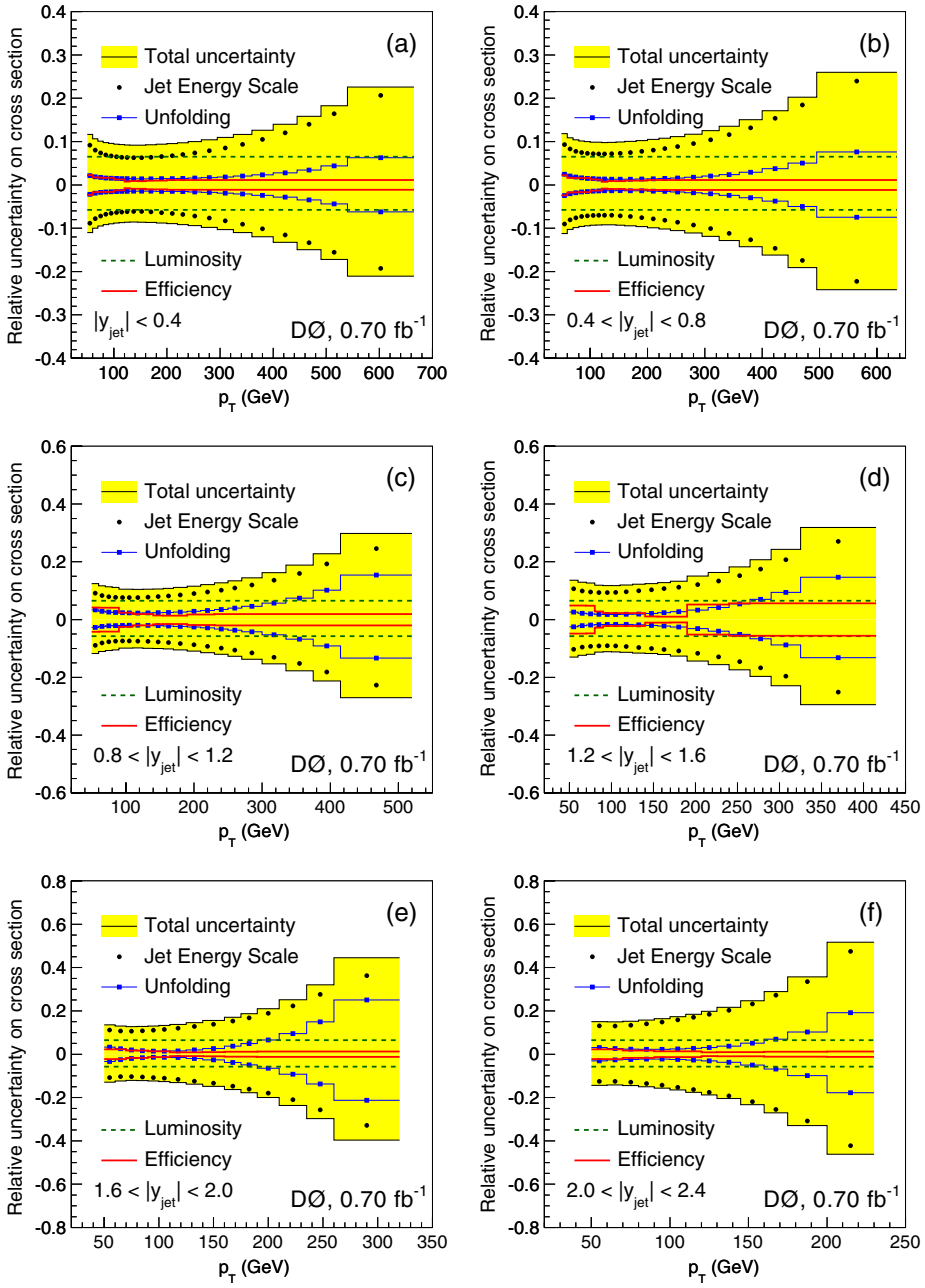

FIG. 45 (color online). (color online) Different components of the systematic uncertainty as a function of jet p_T in the six y bins.

small will lose very little information compared to the full information given in the 91 different systematic uncertainties.

We combine uncertainties that are correlated and of similar shape to reduce the number of components in the covariance matrix. We develop a robust systematic approach for regrouping the sources based on the notions of source size, shape similarity, and orthogonality. The natural measure for the size of a source is the impact it has on the overall χ^2 in the fit with the ansatz function when shifted by one standard deviation around the minimum. To assess the similarity in shape between different systematic uncertainties, we define the inner product for sources h and g as

$$\langle h \cdot g \rangle = \sum_{i \in \text{bins}} \frac{h_i \cdot g_i}{\sigma^2_{\text{stat},i}}, \tag{32}$$

where h_i and g_i are the values of two systematic uncertainties and the sum is over the p_T and $|y|$ bins. The size, or magnitude, of a source h can be written using this notation as

$$||h|| = \sqrt{\langle h \cdot h \rangle}. \tag{33}$$

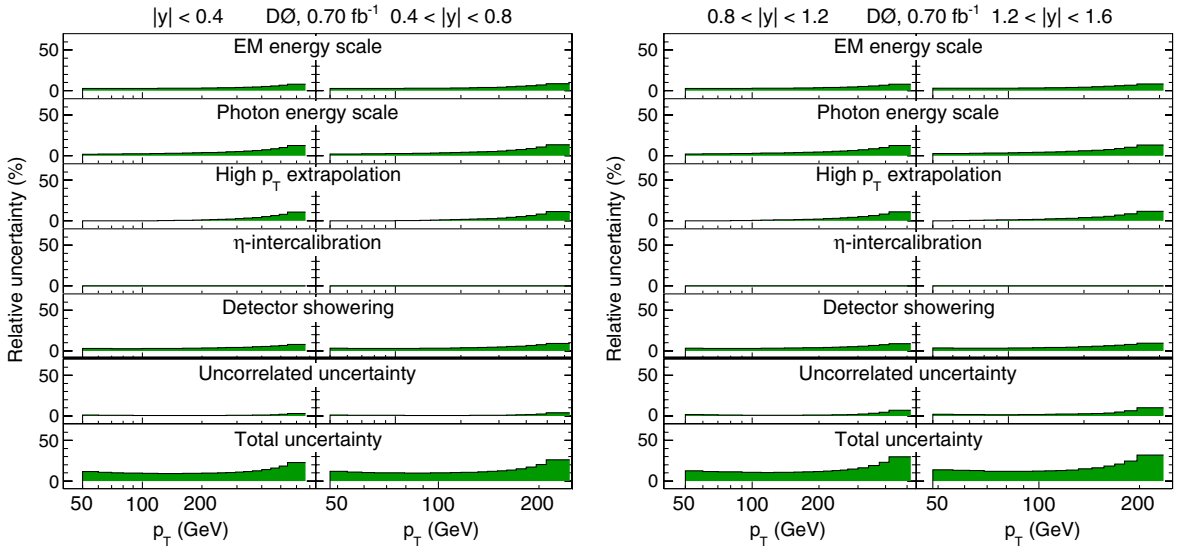

FIG. 46 (color online). (color online) Correlated uncertainties for all central regions and the ICR as a function of jet p_T for four $|y|$ bins, $|y| < 0.4$, $0.4 < |y| < 0.8$, $0.8 < |y| < 1.2$, and $1.2 < |y| < 1.6$. The five largest systematic uncertainties are shown together with uncorrelated and total uncertainties, computed as the sum in quadrature of all sources.

The shape similarity of two sources h and g can be quantified by calculating their correlation, which is written in the notation of Eq. (32) as

$$\rho = \frac{\langle h \cdot g \rangle}{||h|| \cdot ||g||}, \tag{34}$$

which varies between -1.0 and 1.0. When $\rho = 1.0$, the sources are fully correlated, -1.0 fully anticorrelated and 0.0 completely uncorrelated. The source g can be broken into a component that is fully correlated with source h and another component that is fully uncorrelated by considering a linear transformation

$$g' = g - \alpha h. \tag{35}$$

When the orthogonality of h and g' is defined in terms of the inner product,

$$h \perp g' \equiv \langle h \cdot g' \rangle = 0, \tag{36}$$

Eqs. (35) and (36) together yield

$$\alpha = \frac{\langle h \cdot g \rangle}{\langle h \cdot h \rangle}, \tag{37}$$

defining g' as the orthogonal component that is fully uncorrelated with source h. The value g' has the property $\langle g' \cdot g' \rangle \leq \langle g \cdot g \rangle$, $\langle g' \cdot g' \rangle = \langle g \cdot g \rangle$ is equivalent to h being orthogonal to g, and $\langle g' \cdot g' \rangle = 0$ to h being parallel to g. Small values of $||g'||$ indicate that the sources can be combined with little impact on the freedom of the fit to the ansatz.

The sources due to statistical uncertainties in fits are first assigned as uncorrelated. The remaining sources are sorted by size and are then iteratively recombined with other sources most similar in shape and having the smallest orthogonal components. The sources are combined when their correlation is greater than about 85% and the orthogonal components have a magnitude smaller than 10% of the largest individual systematic $\epsilon_{\max}$. At the end of the iterative procedure, the remaining set of sources no longer has any pairings with an orthogonal component less than $0.1\epsilon_{\max}$. The smallest remaining sources with magnitude less than $0.1\epsilon_{\max}$ are added in quadrature to the uncorrelated uncertainty. The final reduced set of uncertainties has 23 correlated sources (principal components) and one fully uncorrelated uncertainty, which is a significant reduction compared to the original 91 sources. The reduced set of 23 correlated sources and the total uncorrelated uncertainty are provided in Ref. [34].

The five leading sources from the reduced set of combined systematic uncertainties, the total uncorrelated uncertainty, and the total uncertainty are shown in Figs. 46 and 47 in the six $|y|$ bins. These sources summarize the leading systematic uncertainties for the measurement, where the names correspond to the dominant contributions to the uncertainty within each group. The EM scale uncertainty comes from the calibration of the EM calorimeter using $Z \rightarrow e^+e^-$ events. The photon energy scale includes the uncertainty in the MC description of the difference in the electron and photon responses and the uncertainty in the amount of passive material in front of the calorimeter, which affects the response difference as a function of photon p_T. The uncertainty in the high p_T extrapolation is due to differences in fragmentation models of PYTHIA and HERWIG, which lead to an additional uncertainty in the high p_T extrapolation of the central response. The rapidity-intercalibration uncertainty summarizes the uncertainty in the relative response calibration between calorimeter

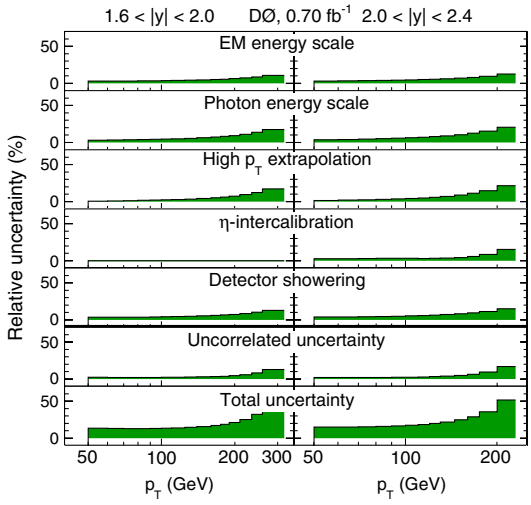

FIG. 47 (color online). (color online) Correlated uncertainties for $1.6 < |y| < 2.0$ and $2.0 < |y| < 2.4$ as a function of jet p_T. The five largest systematic uncertainties are shown together with uncorrelated and total uncertainties, computed as the sum in quadrature of all sources.

regions. The detector showering uncertainty includes the uncertainties on showering, but also additional significant contributions from other uncertainties such as sample purity and the difference between alternate tunes of PYTHIA (tunes A and QW).

XIV. CONCLUSION

In this paper, we described the measurement of the inclusive jet cross section by the D0 experiment. The measured inclusive jet cross section corrected for experimental effects to the particle level in $p\bar{p}$ collisions at $\sqrt{s} = 1.96$ TeV with $\mathcal{L} = 0.70$ fb^{-1} is presented for six $|y|$ bins as a function of jet p_T. The precision reached in this measurement is unprecedented for results from a hadron collider, particularly for processes dependent on gluons at high-x. The measurement is found to be in good agreement with NLO QCD calculations with CTEQ6.5M and MRST2004 PDFs. These results will also be useful for any experiment at a hadron collider such as the LHC where the same techniques can be used to extract the jet energy scale with high precision and to measure the inclusive jet cross section. In addition, a full analysis of correlations between sources of systematic uncertainty was performed, demonstrating a useful method to reduce the complexities of describing numerous sources of uncertainties in the cross section, and increasing the potential impact of these data in global PDF fits.

ACKNOWLEDGMENTS

We thank the staffs at Fermilab and collaborating institutions, and acknowledge support from the DOE and NSF (USA); CEA and CNRS/IN2P3 (France); FASI, Rosatom, and RFBR (Russia); CNPq, FAPERJ, FAPESP, and FUNDUNESP (Brazil); DAE and DST (India); Colciencias (Colombia); CONACyT (Mexico); KRF and KOSEF (Korea); CONICET and UBACyT (Argentina); FOM (The Netherlands); STFC and the Royal Society (United Kingdom); MSMT and GACR (Czech Republic); CRC Program and NSERC (Canada); BMBF and DFG (Germany); SFI (Ireland); The Swedish Research Council (Sweden); and CAS and CNSF (China).

[1] V. M. Abazov *et al.* (D0 Collaboration) Phys. Rev. D **80**, 111107 (2009).
[2] A. Belyaev *et al.*, J. High Energy Phys. 01 (2006) 069.
[3] Z. Nagy, Phys. Rev. D **68**, 094002 (2003) and references therein.
[4] E. Eichten *et al.*, Rev. Mod. Phys. **56**, 579 (1984); **58**, 1065 (1986).
[5] P. Chiappetta and M. Perrottet, Phys. Lett. B **253**, 489 (1991).
[6] N. Arkani-Hamed, S. Dimopoulos, and G. R. Dvali, Phys. Lett. B **429**, 263 (1998); Phys. Rev. D **59**, 086004 (1999); K. R. Dienes, E. Dudas, and T. Gherghetta, Nucl. Phys. B **537**, 47 (1999).
[7] D. Atwood, S. Bar-Shalom, and A. Soni, Phys. Rev. D **62**, 056008 (2000).
[8] V. M. Abazov *et al.* (D0 Collaboration), Phys. Rev. Lett. **101**, 062001 (2008).
[9] M. Voutilainen, Fermilab thesis Report No. FERMILAB-THESIS-2008-19, 2008.
[10] T. Andeen *et al.*, Fermilab Report No. FERMILAB-TM-2365, 2007.
[11] T. Aaltonen *et al.* (CDF Collaboration), Phys. Rev. D **78**, 052006 (2008).
[12] A. Abulencia *et al.* (CDF Collaboration), Phys. Rev. D **75**, 092006 (2007); Phys. Rev. D **74**, 071103 (2006).
[13] B. Abbott *et al.* (D0 Collaboration), Phys. Rev. Lett. **82**, 2451 (1999); **86**, 1707 (2001).
[14] F. Abe *et al.* (CDF Collaboration), Phys. Rev. Lett. **77**, 438 (1996).
[15] V. M. Abazov *et al.* (D0 Collaboration), Nucl. Instrum. Methods Phys. Res., Sect. A **565**, 463 (2006).
[16] S. Abachi *et al.* (D0 Collaboration), Nucl. Instrum. Methods Phys. Res., Sect. A **338**, 185 (1994).
[17] S. Klimenko, J. Konigsberg, and T. M. Liss, Fermilab Report No. FN-0741, 2003.
[18] G. C. Blazey *et al.*, in *Proceedings of the Workshop: "QCD and Weak Boson Physics in Run II"*, edited by

U. Baur, R. K. Ellis, and D. Zeppenfeld (Batavia, Illinois, 2000), p. 47.
[19] T. Kluge, K. Rabbertz, and M. Wobisch, arXiv:hep-ph/0609285.
[20] W. K. Tung *et al.*, J. High Energy Phys. 02 (2007) 053; J. Pumplin *et al.*, J. High Energy Phys. 07 (2002) 012; D. Stump *et al.*, J. High Energy Phys. 10 (2003) 046.
[21] A. D. Martin *et al.*, Phys. Lett. B **604**, 61 (2004).
[22] A. D. Martin *et al.*, Eur. Phys. J. C **63**, 189 (2009).
[23] Buttar *et al.*, arXiv:hep-ph/0803.0678.
[24] B. Abbott *et al.* (D0 Collaboration), Nucl. Instrum. Methods Phys. Res., Sect. A **424**, 352 (1999).
[25] V. M. Abazov *et al.*, Phys. Rev. Lett. **103**, 141801 (2009).
[26] V. M. Abazov *et al.* (D0 Collaboration), Phys. Lett. B **666**, 435 (2008).
[27] T. Sjöstrand *et al.*, Comput. Phys. Commun. **135**, 238 (2001).
[28] V. M. Abazov *et al.* (D0 Collaboration), Phys. Lett. B **639**, 151 (2006).
[29] G. Marchesini *et al.*, Comput. Phys. Commun. **67**, 465 (1992).
[30] We note that nearly all the quark-initiated jets come from light quarks.
[31] For all comparisons of the in-situ calibration methods to expectations from MC truth, particle-level jets are matched to detector level jets using the requirement $\Delta R < R_{\mathrm{cone}}/2$.
[32] S. M. Berman, J. D. Bjorken, and J. B. Kogut, Phys. Rev. D **4**, 3388 (1971); R. P. Feynman, R. D. Field, and G. C. Fox, Phys. Rev. D **18**, 3320 (1978).
[33] G. D. Lafferty and T. R. Wyatt, Nucl. Instrum. Methods Phys. Res., Sect. A **355**, 541 (1995).
[34] Measurements and correlations are available at http://hepdata.cedar.ac.uk/View/7662670.
[35] R. Field, M. G. Albrow *et al.* (TeV4LHC QCD Working Group), arXiv:hep-ph/0610012.
[36] A. D. Martin *et al.*, Eur. Phys. J. C **63**, 189 (2009).
[37] F. D. Aaron *et al.*, J. High Energy Phys. 01 (2010) 109.
[38] S. Alekhin *et al.*, Phys. Rev. D**81**, 014032 (2010).
[39] H.-L. Lai *et al.*, Phys. Rev. D **82**, 074024 (2010).
[40] R. D. Ball *et al.*, Nucl. Phys. **B838**, 136 (2010).

Cluster Hadronization in HERWIG 5.9

Alexander Kupčo

Institute of Physics, Na Slovance 2, 182 21 Prague 8, Czech Republic

Abstract: The HERWIG 5.9 cluster hadronization model is briefly discussed here. It is shown that the model has peculiar behaviour when new heavy baryon resonances are included in the HERWIG 5.9 particle table. New fragmentation model is proposed to cure this problem and simple tuning of HERWIG 5.9 with this new model has been made using event shapes variables and identified particle momentum spectra in e^+e^- interactions at LEPI. Finally, the predictions of the two hadronization models are compared.

1 Introduction

Fragmentation of quarks and gluons into hadrons is a typical non-perturbative phenomenon and phenomenological methods must be used to model it. The three basic models are available at present: independent fragmentation (ISAJET, [1]), string fragmentation (JETSET, [2]), and cluster hadronization (HERWIG, [3]).

The independent fragmentation model does not take into account the colour connections and it is also less successful than other two models. The concept of colour connection is essential for the string and cluster hadronization models. JETSET gives better agreement with the experimental data then HERWIG but also contains a large number of parameters which can be tuned. Nevertheless, HERWIG, with its few-parametric cluster hadronization model, represents main alternative to the string models.

In this paper it is shown that the behaviour of HERWIG 5.9 in relation to the light quark sector (u, d, s) does not correspond to the naive view of cluster hadronization in that the introduction of the new baryon cluster decay channels does not lead to an increase in the predicted proton yield. In fact, the proton multiplicity decreases in comparison to predictions made with the default particle list.

This article reviews the HERWIG 5.9 hadronization model and pins down the origin of the peculiar behaviour. A new hadronization model is proposed to cure the problem. To make reliable comparison between the two models, it was necessary to tune the new one. Finally, the differences between the models are discussed. Wherever possible the names of variables are taken from HERWIG 5.9 notation. They are indicated by `typewriter` font.

This work is important for analyses at the HERA experiments in that a reliable theoretical description of the baryon sector needs to be provided. Although there have so far been very few

experimental results on baryon yield from H1 and ZEUS, interesting observations are already being made on strangeness suppression [4, 5] and baryon number propagation [6] and, with the high statistics now available to the experiments, this will soon become an experimentally productive area.

2 Hadronization in HERWIG 5.9

Colourless clusters are formed from colour connected quarks, [7]. They consist of quark-antiquark (meson-like clusters), quark-diquark (baryon-like), or antiquark-antidiquark (anti-baryon-like) pairs . Only the meson-like clusters can occur in e^+e^- interactions. The basic idea of the model is that the clusters decay according to the phase space available to the decay products.

2.1 HERWIG 5.9 parameters and variables

The most important HERWIG 5.9 parameters and variables relevant to cluster model (subroutine `HWCHAD`) are described in this subsection. The values shown here are the default HERWIG 5.9 settings.

The a priori weights for quarks d, u, s, c, b, t, and diquarks (in that order) are assumed to be equal

$$\texttt{PWT(1)} = \cdots = \texttt{PWT(7)} = 1\,. \tag{1}$$

Weights for diquarks of different flavour compositions are also calculated from these and the result is similarly stored in the array `PWT`.

Parameters `CLMAX=3.35` and `CLPOW=2` determine the maximum allowed mass of the cluster

$$M_{max}^{\texttt{CLPOW}} = \texttt{CLMAX}^{\texttt{CLPOW}} + (\texttt{RMASS(ID1)} + \texttt{RMASS(ID2)})^{\texttt{CLPOW}}\ , \tag{2}$$

where `RMASS(ID1)` and `RMASS(ID2)` are masses of the quarks from which the cluster is formed. If the cluster is too heavy it is first cut in two by creation of quark antiquark pair (subroutine `HWCCUT`).

All particles are grouped according to their flavour content and their internal codes `IDHW` are stored in the one-dimensional array `NCLDK`. The first (and also the lightest) hadron of a given flavour (`ID1,ID2`) has position `LOCN(ID1,ID2)` in the array `NCLDK`. The other particles with the same flavour are stored from this position and their number is `RESN(ID1,ID2)`. The masses of the lightest hadrons are put in `RMIN(ID1,ID2)`. Another one-dimensional array `CLDKWT` stores spin weights and mixing weights. For every flavour these weights are normalised by the maximum weight.

Individual weights are stored for all particles in the table `SWTEF`. This weights are set to one in the default HERWIG 5.9 version. There are also parameters that set individual weights for group of particles in HERWIG 5.9, for example `DECWT` is the weight for baryons in decuplet.

2.2 Implementation of cluster hadronization model (HWCHAD)

If the mass EM0 of cluster with flavour content (ID1,ID3) is equal to the mass of the lightest hadron with the same flavour then the cluster is identified with this hadron. In the other cases the cluster decays into two hadrons.

To begin with, the channel with the lightest decay products is chosen. If the sum of their masses (EM1, EM2) is bigger than the cluster mass EM0 then cluster decays by π^0 emission. In the other cases the phase space PCMAX of this decay is used as a maximum phase space weight

$$\texttt{PCMAX} = \sqrt{\texttt{EM0}^2 - (\texttt{EM1} + \texttt{EM2})^2} \cdot \sqrt{\texttt{EM0}^2 - (\texttt{EM1} - \texttt{EM2})^2}. \tag{3}$$

The hadronization of the cluster proceeds in the following three steps.

1. The (di)quark anti(di)quark pair of the flavour ID2 is created from vacuum according to the probability
$$P_{flavour}(\texttt{ID2}) = \texttt{PWT(ID2)} \,/\, \sum_{\texttt{I}} \texttt{PWT(I)}, \tag{4}$$
where the sum is over all allowed flavours.

2. One hadron with flavour (ID1,ID2) is randomly chosen from the iso-flavour table NCLDK and this particle is accepted according to its weight CLDKWT. If the particle is not accepted then another hadron with the same flavour content (ID1,ID2) is taken from the table and so on. The corresponding probability that particle IR1 = NCLDK(I1) is chosen is then
$$P_{spin}(\texttt{IR1}|\texttt{ID1},\texttt{ID2}) = \frac{\texttt{CLDKWT(I1)}}{\sum_{\texttt{LOCN(ID1,ID2)}}^{\texttt{LOCN+RESN-1}} \texttt{CLDKWT(I)}} \ . \tag{5}$$
The same procedure is applied to the hadrons with flavour (ID2,ID3).

3. Once the decay channel has been chosen it is accepted according to its phase space PCM (given by formula (3)) with probability
$$P_{phase} = \sqrt{\texttt{SWTEF(IR1)}} \cdot \sqrt{\texttt{SWTEF(IR2)}} \cdot \texttt{PCM} \,/\, \texttt{PCMAX} \ . \tag{6}$$
If the decay mode is not accepted the algorithm starts again from the first point (i.e. from creation of quark antiquark pair).

This algorithm gives the following expression for the probability for decay of the given cluster (ID1,ID3) into the hadrons with codes IR1=NCLDK(I1) and IR2=NCLDK(I2)

$$P(\texttt{IR1},\texttt{IR2},\texttt{ID2}|\texttt{ID1},\texttt{ID3}) = P_{flavour} \cdot P_{spin}(\texttt{IR1}) \cdot P_{spin}(\texttt{IR2}) \cdot P_{phase} \ . \tag{7}$$

It is now clear, why the inclusion of some new massive resonances with a given flavour leads to the suppression of all decay channels with the hadrons of the same flavour. Omitting hadron spins and mixing weights, probability (5) depends only on the number of iso-flavour particles

$$P_{spin}(\texttt{IR1}|\texttt{ID1},\texttt{ID2}) = \frac{1}{\texttt{RESN(ID1,ID2)}} \ . \tag{8}$$

Finally, the overall probability of a cluster to decay into channels with created flavour ID2 is

$$\begin{aligned} P(\texttt{ID2}|\texttt{ID1},\texttt{ID3}) &= \sum_{\texttt{IR1},\texttt{IR2}} P(\texttt{IR1},\texttt{IR2},\texttt{ID2}|\texttt{ID1},\texttt{ID3}) \\ &\propto \texttt{PWT(ID2)} \cdot \frac{\sum_{\texttt{IR1},\texttt{IR2}} P_{phase}}{\texttt{RESN(ID1,ID2)} \cdot \texttt{RESN(ID2,ID3)}} \ , \end{aligned} \tag{9}$$

which is nothing else than the **mean** value of phase spaces of the corresponding decay channels. The phase space of resonances is small due to their high masses. Hence, this new resonances lower value of the overall probability (9).

The motivation for the HERWIG authors was to eliminate factor 1/2 in $u\bar{u}$ and $d\bar{d}$ mixing for neutral non-strange mesons, [12]. Indeed, this algorithm gives the same number of π^0 and π^+ in the case where there are only u and d quarks, with no baryons, and with π^0, $\pi^\pm$, and isotopic (η-like) singlet.

This behaviour of HERWIG 5.9 is demonstrated in Tab. 3. Both versions (5.8 and 5.9) have the same default settings but HERWIG 5.9 particle table contains more meson resonances. Consequently, baryon production was enhanced and meson production decreased.

3 New cluster hadronization model

In the rest frame of a particle of mass M, the width of a two-body decay is given, generally, by expression

$$\mathrm{d}\Gamma = \frac{1}{32\pi^2} \left|\mathcal{M}\right|^2 \frac{|\boldsymbol{p_1}|}{M^2} \mathrm{d}\Omega \, , \tag{10}$$

where final particles are labeled 1 and 2, $\mathcal{M}$ is the corresponding matrix element, and

$$|\boldsymbol{p_1}| = |\boldsymbol{p_2}| = \frac{\left[\left(M^2 - (m_1+m_2)^2\right)\left(M^2 - (m_1-m_2)^2\right)\right]^{1/2}}{2M} = \frac{\texttt{PCM}\,(M, m_1, m_2)}{2M} \tag{11}$$

are the momenta of final state particles.

We do not know a great deal about the matrix element. We can sum over final states (spin factors), we can take into account mixing of flavours (mixing weights) and we can apply Zweig's rule which states the two-body decays of cluster (ID1,ID3) to pair of hadrons with flavour (ID1,ID3) and (ID2,ID2) are strongly suppressed. Assuming that the matrix elements are the same for all decay channels of a cluster and that they depend only on the flavour ID2 of a created (di)quark anti(di)quark pair, the weight W(IR1,IR2,ID2|ID1,ID3) of particular decay of cluster (ID1,ID3) into hadrons IR1 and IR2 with flavour content (ID1,ID2) and (ID2,ID3) is

$$\begin{aligned} W(\texttt{IR1},\texttt{IR2},\texttt{ID2}|\texttt{ID1},\texttt{ID3}) = \texttt{PWT(ID2)} \cdot (2J_1+1) \cdot (2J_2+1) \cdot \texttt{WT(IR1)} \cdot \texttt{WT(IR2)} \cdot \\ \cdot \texttt{SWTEF(IR1)} \cdot \texttt{SWTEF(IR2)} \cdot \texttt{PCM(EM0,EM1,EM2)} \ , \end{aligned} \tag{12}$$

where J_1, J_2 are particle spins and WT is flavour mixing weight.

The overall probability for decay channels with created flavour ID2 is then (again omitting spins, mixing weights, and individual weights SWTEF)

$$P(\texttt{ID2}|\texttt{ID1},\texttt{ID3}) \propto \texttt{PWT(ID2)} \cdot \sum_{\texttt{IR1},\texttt{IR2}} \texttt{PCM} \ . \tag{13}$$

Contrary to Eq.(9) this probability is proportional to the **sum** of the phase spaces of particular channels. Therefore, the inclusion of new baryon resonances will enhance the baryon multiplicities.

The new hadronization model is based on formula (12). Several subroutines have been changed to implement this model into HERWIG 5.9 (`HWCHAD, HWURES`). Moreover, HERWIG 5.9 particle table had to be extended. As was mentioned earlier, there are plenty of meson resonances in the table but only the basic baryon octet and decuplet. New baryon resonances dramatically increase the probability for a cluster decay through the baryon channel and they play an important role in the new model. Hence, I decided to include all light quark meson and baryon resonances that have their own PDG number in [9]. The branching ratios of particular decay modes were taken also from this paper. The properties of these new resonances were put in new subroutine `MHWRES`.

3.1 Tuning HERWIG 5.9 with new hadronization model

To make final comparison between the both hadronization models, one has to use the tuned settings of HERWIG 5.9 parameters. The L3 fit has been used for the original model (see Tab. 1).

	H5.9	H5.9n	H5.9n
parameter	**L3 fit**	**CAND1**	**CAND2**
`QCDLAM`	0.177	0.179	0.1602
`RMASS(13)`	0.75	0.706	0.764
`CLMAX`	3.006	5.27	3.90
`CLPOW`	2.033	—	1.53
`CLSMR`	0.35	—	0.341
`DECWT`	0.5	—	0.753
`PWT(3)`	0.88	—	1.071
`PWT(7)`	0.80	0.812	2.408

Table 1: Settings of HERWIG 5.9 for both hadronization models.

Complete tuning of HERWIG 5.9 with new hadronization model has not been attempted. I used the same method as in [11] but with fewer statistics so the presented results can still be improved. DELPHI measurements of event shape variables [11] and LEPI data of p–spectra of identified particles have been used for tuning the parameters. There are two settings for HERWIG 5.9 with new hadronization (H5.9n) in the Tab. 1. In the case of **CAND1** setting, only four parameters have been tuned. **CAND2** represents the best fit where the same parameters was tuned as in the case of L3 fit. Tab. 2 gives a summary of the fit results.

4 Comparison of the two cluster hadronization models

Although the probability of cluster decay through the particular channel is proportional to the phase space in both cases, the strange normalisation factors of the standard version (see Eq. (5)) give different behaviour of the models.

	Event shapes	Ident. particles	All channels
L3 fit	$\chi^2 = 2874/305 = 9.4$	$\chi^2 = 1002/157 = 6.4$	$\chi^2 = 3876/462 = 8.4$
CAND1	$\chi^2 = 3121/260 = 12.0$	$\chi^2 = 921/130 = 7.1$	$\chi^2 = 4042/390 = 10.5$
CAND2	$\chi^2 = 2319/305 = 7.6$	$\chi^2 = 824/157 = 5.2$	$\chi^2 = 3143/462 = 6.8$

Table 2: Summary of fit results.

CAND1 setting of HERWIG 5.9 is the worst one (see Tab. 2). This could be due to a small number of fitted parameters. Nevertheless, one can find quite a good agreement with the identified particle multiplicities data in the basic meson and baryon octet, Tab. 3.

On the other hand, **CAND2** gives a better description of the data than the HERWIG 5.9 default model with the **L3** setting. The set of fitted parameters was the same, so it is more appropriate to compare these two settings. Since the **L3** fit was made on slightly different data some inconsistency still survives.

Concerning identified particle multiplicities, **CAND1** predictions are in an excellent agreement with the data in the whole meson sector except η' and Φ. Good agreement is also found in the basic baryon octet (except Ξ^-) but large discrepancies occur in the basic baryon decuplet ($\Sigma(1385)$ and $\Xi(1530)^0$).

The situation is roughly the same in the case of **CAND2** set. The agreement with the data is slightly worst (especially for K^0 and $K^\pm$) and the problems with baryon resonances were not cured although parameter `DECWT` was also tuned in this fit.

The default HERWIG 5.9 hadronization model (**L3** fit) has similar problems in describing the data here. Moreover, it underestimates the production of protons and Λ particles.

Both hadronization models give (within the experimental uncertainties) the correct particle multiplicities for the lightest non-strange mesons and baryons (π, η, ρ, ω, p, Δ) although the new model predictions are slightly closer to the data. The discrepancies occur for the singlet mesons η' and $\Phi(1020)$ and for heavy strange baryons.

5 Conclusions

It has been observed that with the introduction of new nucleon resonances, HERWIG 5.9 predicts a reduced proton yield, contrary to the naive view of cluster hadronization. In the HERWIG 5.9 hadronization scheme, a decay of a colourless cluster takes place in such a way as to eliminate the factor 1/2 in $u\bar{u}$ and $d\bar{d}$ mixing. The algorithm, however, gives the probability of a cluster decay through channels with a created particular flavour that is proportional to the mean value of corresponding phase spaces.

A new hadronization model which treats all decay channels in the same way has been proposed. It was found that this provides an improved description of inclusive particle data taken by the LEP experiments. In particular, the baryon sector is better described that with the default version of HERWIG 5.9. This is a particularly important if the HERWIG model is to be used predictively in HERA environment, in which topics such as baryon number propagation and strange diquark suppression are starting to be studied.

Particle	**PDG'98**	H5.8	H5.8	H5.9	H5.9	H5.9n	H5.9n
		Delphi	**DEF**	**DEF**	**L3**	**CAND**	**CAND**
		FIT			**FIT**	**ONE**	**TWO**
charged	21.05 ± 0.20[8]	20.81	21.17	20.62	21.13	21.03	21.52
π^0	9.42 ± 0.56	9.79	9.76	10.14	10.88	9.51	9.74
$\pi^{\pm}$	17.1 ± 0.4	17.64	17.52	16.7	17.62	17.26	17.53
K^0	2.013 ± 0.033	2.03	2.29	1.937	1.949	1.981	2.253
$K^{\pm}$	2.39 ± 0.12	2.11	2.40	2.10	2.20	2.32	2.54
η	0.97 ± 0.10	1.01	1.01	0.92	1.01	0.79	0.89
η'	0.222 ± 0.040	0.14	0.144	0.140	0.157	0.109	0.125
$\rho(770)^0$	1.28 ± 0.14	1.43	1.32	1.16	1.29	1.12	1.12
$K^*(892)^0$	0.747 ± 0.028	0.75	0.796	0.521	0.565	0.640	0.734
$\Phi(1020)$	0.109 ± 0.007	0.099	0.120	0.181	0.178	0.208	0.182
$\omega(782)$	1.10 ± 0.13	0.92	1.10	1.05	1.23	1.00	1.02
p	0.964 ± 0.102	0.77	0.948	1.41	0.77	0.959	0.944
Λ	0.372 ± 0.009	0.367	0.431	0.598	0.256	0.363	0.389
Σ^-	0.071 ± 0.018	0.058	0.066	0.10	0.069	0.082	0.092
Ξ^-	0.0258 ± 0.0010	0.048	0.052	0.070	0.0242	0.0195	0.0208
Δ^{++}	0.085 ± 0.014	0.158	0.198	0.276	0.109	0.113	0.100
$\Sigma(1385)^{\pm}$	0.0462 ± 0.0028	0.118	0.15	0.20	0.069	0.0713	0.0617
$\Xi(1530)^0$	0.0055 ± 0.0005	0.026	0.024	0.037	0.0053	0.0120	0.0091
Ω^-	0.0016 ± 0.0003	0.0074	0.0078	0.0094	0.0009	0.0019	0.0011
$\Lambda(1520)$	0.0213 ± 0.0028[8]	—	—	—	—	0.0426	0.0339

Table 3: Particle multiplicities per event in e^+e^- interactions at $\sqrt{s} = 91.2\,\mathrm{GeV}$ in the data [10] compared with HERWIG 5.8 (H5.8), HERWIG 5.9 prediction for default cluster hadronization model (H5.9), and for new hadronization model (H5.9n).

References

[1] F. E. Paige et al., *Isajet manual, http://ox3.phy.bnl.gov/~serban/isajet/doc/isajet.ps*

[2] T. Sjöstrand, *Comp. Phys. Commun.* **82**, 74 (1994)

[3] G. Marchesini, B. R. Webber, G. Abbiendi, I. G. Knowles, M. H. Seymour, and L. Stanco, *Comp. Phys. Commun.* **67**, 465 (1992)

[4] ZEUS Collaboration, *Z. Phys.* C **68**, 29 (1995)

[5] H1 Collaboration, *Nucl. Phys.* B **480**, 3 (1996)

[6] H1 Collaboration, *Paper 556 submitted to ICHEP98, Vancouver, Canada*

[7] G. Marchesini, B. R. Webber, *Nucl. Phys.* B **310**, 461 (1988)

[8] OPAL Collaboration, *CERN-PRE/96-99* , (1996)

[9] L. Montanet et al., *Phys. Rev.* D **50**, (1994)

[10] C. Caso et al, *The European Physical Journal* C **3**, 1 (1998)

[11] DELPHI Collaboration, *Z. Phys.* C **73**, 11 (1996)

[12] B. R. Webber, *Private communication*